Theses and Dissertations   Graduate School

2015

Femtosecond Laser Beam Propagation through Corneal Tissue: Evaluation of Therapeutic Laser-Stimulated Second and Third-Harmonic Generation

William R. Calhoun III
Virginia Commonwealth University

Femtosecond Laser Beam Propagation through Corneal Tissue: Evaluation of Therapeutic Laser-Stimulated Second and Third-Harmonic Generation

A dissertation submitted in partial fulfillment of the requirements for the degree of Doctor of Philosophy at Virginia Commonwealth University.

by
William R. Calhoun III,
B.A. Miami University 2007

Directors: Ilko K. Ilev Ph.D., Senior Staff Scientist and Lab Leader, Division of Biomedical Physics, U.S. Food and Drug Administration; Gerald Miller Ph.D., Professor and Chair, Biomedical Engineering, Virginia Commonwealth University

Virginia Commonwealth University
Richmond, VA
May 2015

For my wife and son

Acknowledgment

I would like to thank several people. My journey overcoming the many hurdles and long days that define graduate school would not have been possible without their assistance and encouragement.

I of course must begin with my friend and advisor Dr. Ilko Ilev. Beginning during a summer undergraduate internship in 2006, Ilko believed in me and has cheered louder than anyone on my behalf. His ability to breakdown the most complicated topics into their fundamental principles has given me the confidence to tackle difficult questions and pursue any scientific endeavor.

I am very grateful for the support I have received from ORISE and the Division of Biomedical Physics at the FDA over the past 5 years. In addition, my studies wouldn't have been possible without the support of Dr. Gerald Miller, Dr. Paul Wetzel, Dr. Daniel Conway and the Department of Biomedical Engineering at VCU. Their willingness to support my research at the FDA despite the added complexity is much appreciated.

I thank Dr. Esen Akpek for our discussions. Her clinical point of view and input has been invaluable in my thought process and in the application of this work to tangible, real-world problems.

I owe a very special thank you to my undergraduate advisor, Dr. Samir Bali, for opening my eyes to the world of optics and for his contagious and sincere enthusiasm for science that led me down this career path.

I am forever in debt to my parents who have encouraged me to follow my passions and have provided unwavering support over the years which has allowed me to focus all of my effort on my education. Most importantly though, they have taught me through example the importance of integrity, hard-work, and gratitude. These morals are undoubtedly behind any of my successes.

I thank my friends and family for their loving support and their belief in me over the years. I am fascinated by their unique ability to listen to me talk exhaustingly about my research without showing the slightest sign of disinterest or boredom.

To my wife Gabriela: Since the day we met, you have humbled me with your courage, trust in people and ability to balance professionalism with humanity. My perpetual positive attitude, energy and happiness are generated by your care for and confidence in me. Eu te amo.

Table of Contents

Abstract

FEMTOSECOND LASER BEAM PROPAGATION THROUGH CORNEAL TISSUE: EVALUATION OF THERAPEUTIC LASER STIMULATED SECOND- AND THIRD-HARMONIC GENERATION

William R. Calhoun III, Ph.D. Candidate

A dissertation submitted in partial fulfillment of the requirements for the degree of Doctor of Philosophy at Virginia Commonwealth University.

Virginia Commonwealth University 2015

Directors: Ilko K. Ilev Ph.D., Senior Staff Scientist and Lab Leader, Division of Biomedical Physics, U.S. Food and Drug Administration; Gerald Miller Ph.D., Professor and Chair, Biomedical Engineering, Virginia Commonwealth University

One of the most recent advancements in laser technology is the development of ultrashort pulsed femtosecond lasers (FSLs). FSLs are improving many fields due to their unique extreme precision, low energy and ablation characteristics. In the area of laser medicine, ophthalmic surgeries have seen very promising developments. Some of the most commonly performed surgical operations in the world, including laser-assisted *in-situ* keratomileusis (LASIK), lens replacement (cataract surgery), and keratoplasty (cornea transplant), now employ FSLs for their unique abilities that lead to improved clinical outcome and patient satisfaction.

The application of FSLs in medical therapeutics is a recent development, and although they offer many benefits, FSLs also stimulate nonlinear optical effects (NOEs), many of which were insignificant with previously developed lasers. NOEs can change the laser characteristics during propagation through a medium, which can subsequently introduce unique safety concerns for the surrounding tissues. Traditional approaches for characterizing optical effects, laser performance, safety and efficacy do not properly account for NOEs, and there remains a lack of data that describe NOEs in clinically relevant procedures and tissues. As FSL technology continues to expand towards new applications, FSL induced NOEs need to be better understood in order to ensure safety as FSL medical devices and applications continue to evolve at a rapid pace.

In order to improve the understanding of FSL-tissue interactions related to NOEs stimulated during laser beam propagation though corneal tissue, research investigations were conducted to evaluate corneal optical properties and determine how corneal tissue properties including corneal layer, collagen orientation and collagen crosslinking, and laser parameters including pulse energy, repetition rate and numerical aperture affect second and third-harmonic generation (HG) intensity, duration and efficiency. The results of these studies revealed that all laser parameters and tissue properties had a substantial influence on HG. The dynamic relationship between optical breakdown and HG was responsible for many observed changes in HG metrics. The results also demonstrated that the new generation of therapeutic FSLs has the potential to generate hazardous effects if not carefully controlled. Finally, recommendations are made to optimize current and guide future FSL applications.

List of Figures and Tables

Chapter 1 – Introduction

One of the most important innovations of the 20th century was the invention of the laser in the 1960s [1]. In principle, a laser is a device that emits highly correlated light through an optical amplification process. The magnitude of this invention was validated by the awarding of the Nobel Prize in 1964 for the research leading to the development of the laser. Since then, the laser has revolutionized the world and now affects almost everyone on a daily basis. Lasers have allowed vast improvements across many areas including communication, medicine, laboratory research, consumer electronics, manufacturing, entertainment, law enforcement, and military [2].

The femtosecond laser (FSL), developed in the 1980's [3, 4], has created numerous opportunities and further improvements in many fields. FSLs emit a train of extremely short pulses of near-infrared (near-IR) light, each on the order of 10^{-15} seconds, femtoseconds, hence the laser's name. The novelty of FSLs lies in their ability to produce extremely high intensities using very low energy due to the brevity of the pulse. When applied, less energy translates to less collateral effects and damage to the medium surrounding the laser target [5]. This allows nanometer-scale manipulations to be made in a variety of materials. Further, the FSL has the ability to target isolated subsurface locations without affecting the medium above or below the laser focus. In addition to material manipulations, FSLs have led to several revolutionary imaging techniques. For these reasons there continues to be significant efforts to develop FSLs for numerous uses in a broad range of fields. Medical applications continue to be one of the most prominent targets of development. Areas benefiting from this technology include drug

development [6], imaging [7], neurosurgery [8], dentistry [9], and targeted cancer therapy [10], with the most notable area to date being ophthalmology [11-15].

Due to low scattering and absorption of FSL-emitted, IR light by ocular tissues and the ability of the laser to precisely ablate tissue at subsurface locations without damaging tissue outside the laser focus, ophthalmic applications were an attractive target for developing the first FSL-based clinical therapies [16]. The most successful of which is the use of FSLs in corneal refractive surgery known as laser-assisted *in-situ* keratomileusis (LASIK) [17, 18]. Many other ophthalmic surgical procedures benefitting from the capabilities of using an FSL have been developed and continue to emerge including keratoplasty (cornea transplantation), lens replacement (cataract surgery) and other corrective refractive surgeries [13, 15].

The fundamental therapeutic effect, efficiently generated by the FSLs, that forms the basis of most ophthalmic applications is laser induced breakdown (LIB). LIB occurs only when a large amount of laser energy is concentrated in a very small volume in a very short period of time. By focusing IR light generated by an FSL within the thickness of ocular tissues, LIB causes a small volume of tissue to be vaporized. Further, by scanning the laser focus through the tissue in 3 dimensions, various tissue cutting morphologies can be produced that are more precise and versatile than the manual surgical techniques that they replace [19-22].

The unprecedented optical field intensities generated by focused FSL light pulses allow them to generate a variety of nonlinear optical effects (NOEs). NOEs are a product of a high intensity optical field interacting with the medium through which it is propagating. LIB is one example of a NOE. Another NOE, harmonic generation (HG) converts FSL energy to other optical frequencies and can occur in the human cornea [23, 24].

1.1 Motivation

The application of FSLs in medical therapeutics is a recent development, and although they offer many benefits, FSLs also introduce novel safety concerns and inefficiencies related to laser stimulated NOEs, many of which were insignificant with previous lasers. LASIK and keratoplasty procedures account for approximately 850,000 procedures per year in the United Sates [25], the majority of which employ FSLs [26]. Further, FSLs have dramatically improved cataract surgery [21, 22], the most common surgical procedure in the United States [27] and the world [28] with 19.7 million procedures performed worldwide in 2012 [29]. Although not yet the standard of care, FSLs improve conventional keratoplasty (cornea transplant surgery) and allow more complex and beneficial versions of this surgery as well. Keratoplasty accounts for approximately 47,000 procedures annually in the United States [30]. LIB generated by the therapeutic FSL is an essential part of the surgical process. However, many other NOEs are not desirable in this context, yet occur in parallel with LIB. In the case of ophthalmic FSLs, HG can generate green and ultraviolet (UV) light, both optical spectral frequencies being capable of damaging surrounding tissues. Normally, the cornea absorbs the majority of UV light entering the eye. In the case of HG, UV light is being produced within the cornea, bypassing the protective feature of the cornea leaving more UV to continue into the eye.

HG has been extensively studied in nonlinear crystals and other synthetic materials [31, 32] for material characterization and laser design purposes as well as for imaging various tissues [33]. These applications require low intensity lasers and consequently produce weak HG, detected using powerful signal amplification. Therapeutic FSLs emit intensities that are orders of magnitude higher than those previously mentioned, and are likely capable of generating much

more intense visible and UV harmonics. Since the use of FSLs in medical therapeutics is a recent development, there is a poor understanding of NOEs generated in living tissues.

Independent of the specific FSL ophthalmic procedure, FSL energy must passes through the cornea, which further highlights the importance of better understanding HG in the corneal tissue. It is important to determine if HG poses a significant risk to the safety of the patient and if HG can be minimized. This is especially important since different types of FSL using different laser parameters for a variety of procedures exist.

The results of the proposed systematic investigation of the relationship between specific laser parameters and tissue properties and NOEs will not only improve the knowledge of these fundamental laser-tissue interactions, but will also guide the laser and medical industry in development of safer and more effective devices for all areas of laser medicine. With a large movement to personalize medicine, findings from this study may also allow for a more tailored laser therapy based on the specific nature of each patient's tissues. Standard test methods and limitations will be established that can be used for future evaluation of clinical therapeutic devices. As more clinical procedures continue to adopt FSLs, and previously impossible solutions are made possible with the unique capabilities of FSLs, the information gained through this study will also serve to protect the public by shedding light on these previously uninvestigated medical device phenomena.

1.2 Objectives

Using previous biomedical optics and laser-tissue interaction experience, this project intends to characterize the influence of specific tissue properties and laser parameters on HG stimulated in corneal tissue. This will be accomplished by developing of an experimental system capable of

repeatable application of FSL radiation to living corneal tissues and measurement of the resulting HG while varying specific critical laser and tissue parameters. The specific tissue parameters that will be investigated are broad band spectral transmission, tissue layer (depth), collagen orientation and degree of collagen crosslinking. The specific laser parameters that will be investigated are pulse energy, pulse repetition rate, and focusing angle. The resulting effects of varying these tissue properties and laser parameters will be evaluated by measuring HG intensity, duration and efficiency. Using these measurements, potential ocular safety concerns will be determined by performing an ocular tissue hazard analysis. Further, recommendations will be made to guide the current and future FSL based ophthalmic surgical procedures.

1.3 Chapter Overview

This dissertation is organized into six Chapters. The first Chapter is an introduction to this dissertation and includes a brief introduction to FSLs and ophthalmology. The motivation for the proposed work, the objectives of the project and the expected outcomes are discussed as well.

The second Chapter provides a more detailed description of FSLs, why they are an attractive clinical tool, and how they have been applied to ophthalmic surgical procedures including the current status of use. This includes a review of the relevant anatomy and physiology of the eye.

In Chapter three, FSL-tissue interactions are discussed, beginning with a description of the optical properties of relevant ocular tissues. This includes experimental results from human and bovine corneal transmission and birefringence measurement experiments that characterize the tissue using FSLs. The discussion then progresses into NOEs including LIB, second- (SHG) and third-harmonic generation (THG), the nonlinear refractive index, self-focusing and

filamentation. Finally, the concern for ocular safety with respect to FSL use is examined in more detail.

Chapter four focuses on the influence that tissue properties have on HG. Experiments examining how corneal layer, collagen orientation and collagen crosslinking affect SHG and THG intensity are discussed. These results are then translated to clinical practice where benefits of understanding the HG-tissue property relationships are discussed as well as their connection to procedure safety.

Chapter five then examines how varying specific laser parameters affect SHG and THG intensity, duration and efficiency. Laser pulse repetition rate, pulse energy, and focusing angle are tested. The impacts the experimental results have on clinical practices are discussed.

In the final Chapter six, the major findings of this dissertation are summarized and discussed. The experimental findings are compared with current relevant safety standards to assess safety. The two major classes of FSLs are compared with respect to safety. And finally, recommendations are made for ensuring safe use of FSLs into the future.

Chapter 2 - Femtosecond Lasers and Clinical Applications

2.1 Femtosecond lasers

A laser is a device that generates and emits intense, coherent light, through an optical amplification process known as stimulated emission. Optical amplification begins with a pump source, typically a flash lamp or light emitting diode (see Figure 1), which excites electrons within the gain medium to higher energy levels, known as population inversion. The excited electrons will return to their ground state by emitting a photon of light in a random direction,

Principal Solid-State Laser Design
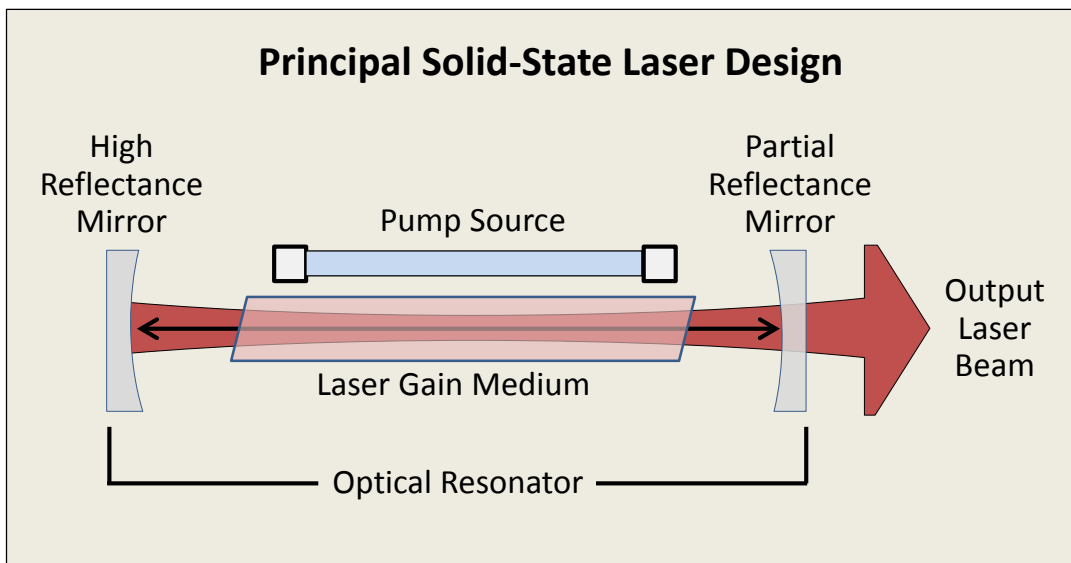
Figure 1. Principle solid-state laser diagram.

known as spontaneous emission. Some of these photons will be emitted in a direction that allows them to oscillate between two mirrors that flank the resonator. Subsequently, the oscillating photon, when incident upon an excited electron, will induce the release of a photon in the same direction and with the same phase. This is known as stimulated emission, and is the fundamental

property of all lasers. Finally, light is emitted from the cavity as some of the oscillating photons transmit through the partially reflecting mirror.

FSLs emit ultrashort pulses (USP) of coherent light rather than a continuous-wave of light. They accomplish this through a process called mode-locking. To understand this principle, a more detailed description of light oscillation within the resonator is required. Although lasers are
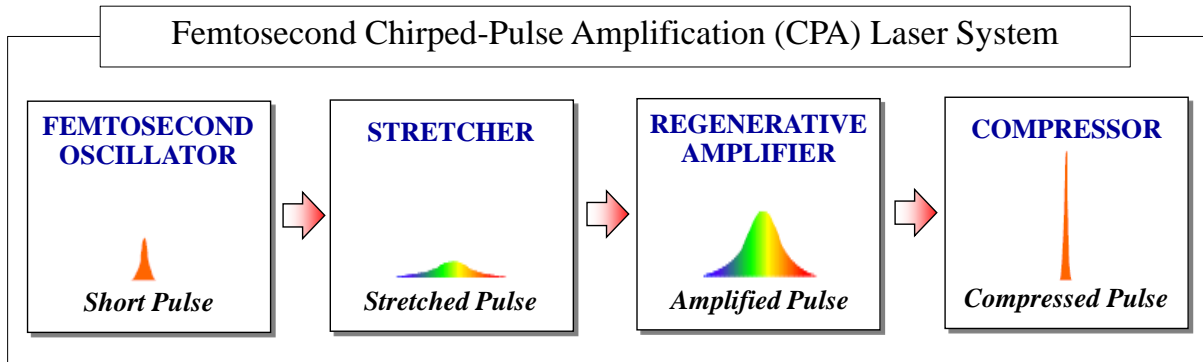
Figure 2. Femtosecond chirped pulse amplification (CPA) sequence diagram.

described as emitting monochromatic light, there is a range of frequencies that are produced within the cavity, known as the gain bandwidth. This is largely determined by the gain medium, with some lasers producing narrow bandwidths (less than 1 nanometer) and others producing broad bandwidths (several hundred nanometers); the FSL being of the latter. Since light is an electromagnetic wave, as it reflects between the cavity mirrors it can constructively and destructively interfere with itself. The result of this process leaves only discrete frequencies that will self-regenerate, forming standing waves known as longitudinal modes. Normally the longitudinal modes have no fixed phase relationship and these modes interfere to generate random pulses of light. However, by inserting a saturable absorber into the laser cavity, strong peaks in interference will be allowed to oscillate while weaker ones will be suppressed creating a mode-locked state. In the case of FSLs, the result of mode locking is a stable train of pulses, each
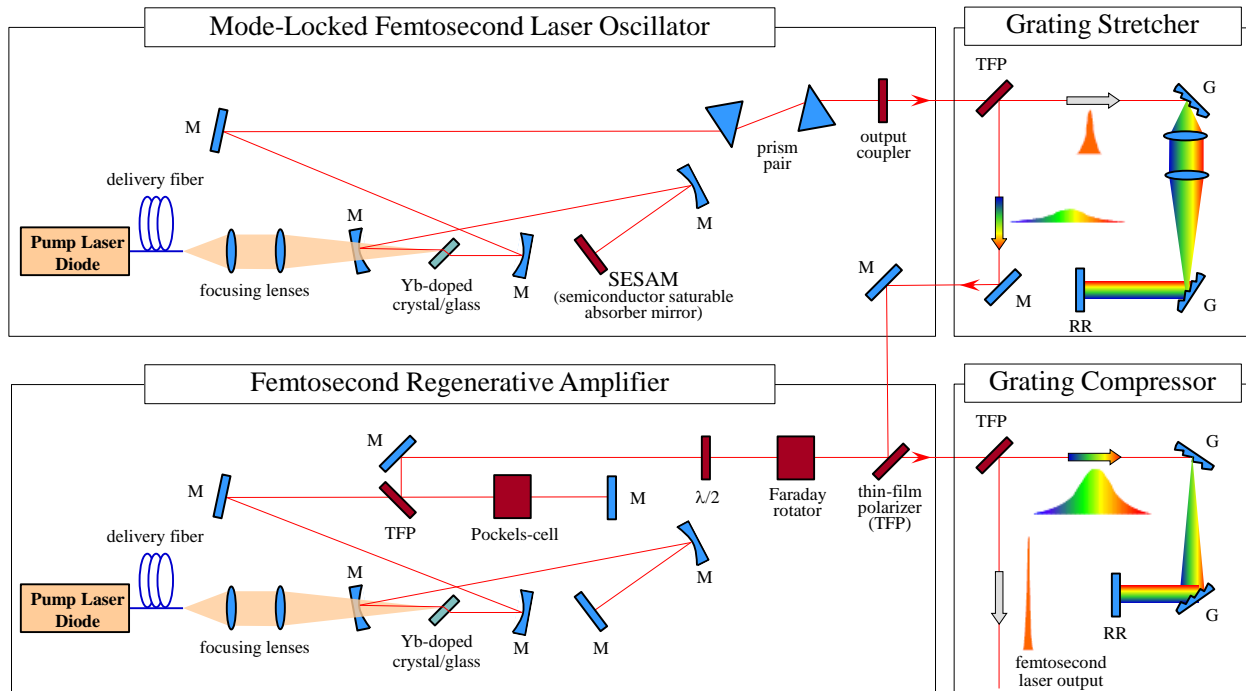
Figure 3. Conventional solid-state femtosecond laser diagram.

on the order of femtoseconds in length. Gain mediums commonly found in FSLs are able to produce large gain bandwidths, which are required to generate many longitudinal modes and subsequently femtosecond length pulses, typically produce light with infrared wavelengths.

FSLs can be complex with respect to the optical components involved, but their function can be simplified to four major steps in a process called chirped pulse amplification (CPA) (see Figure 2). This process begins with the generation of short, weak pulses in the oscillator (mode-locked FSL oscillator). These pulses are then stretched, typically using a grating pair (grating stretcher), which reduces their intensity. The purpose of stretching is so that upon pulse amplification, in the third step, damage to the optical components and nonlinear optical effects are avoided and minimized respectively. The third step, amplification, takes place in a second
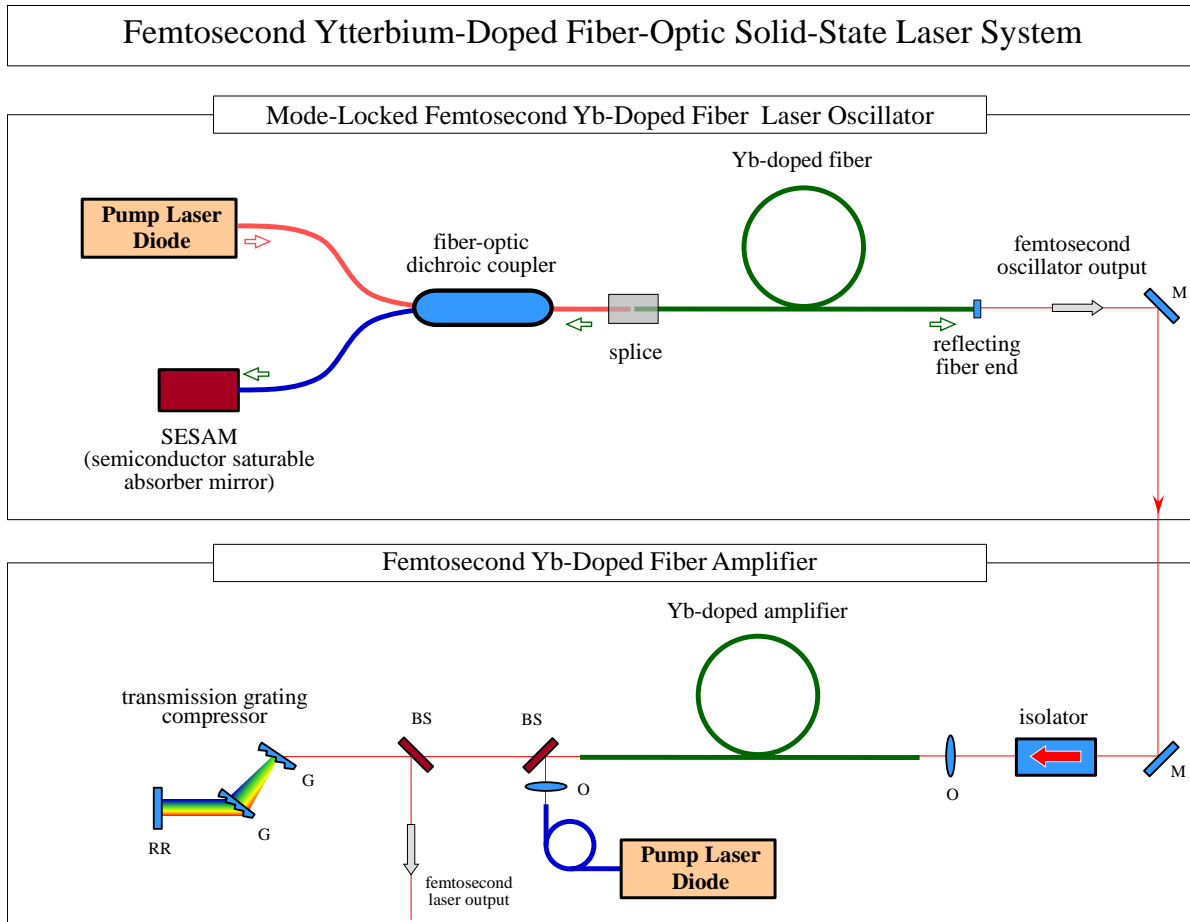
Figure 4. Fiber-based femtosecond laser diagram.

optical resonator (femtosecond regenerative amplifier) where many passes through a second gain medium, which is also pumped, significantly increases the intensity of the pulse. Finally, before exiting the laser housing, a pair of gratings (grating compressor) is used to recompress the pulse, generating a very short, intense pulse. A diagram of the principal optical components of a conventional FSL can be seen in Figure 3. As fiber optic technology continues to develop and offer many advantages over bulk optics, fiber based lasers have emerged as robust, stable and simplified alternatives to conventional laser systems. One of the latest developments in FSLs has been the emergence of fiber-based FSLs. Figure 4 shows a diagram of a typical fiber based FSL. Although fiber based FSLs have many of the same advantageous characteristics of conventional

FSLs, they also introduce additional benefits in terms of achieving high repetition rates, high stability, low noise, compactness and cost. These two trends in FSL technology will be discussed further in terms of a biomedical perspective in a later Section.

2.2 Clinical ophthalmic use of femtosecond lasers

2.2.1 Anatomy and physiology of the eye

The mammalian eye is the organ that allows the sensation of vision. It collects light from the external environment and focuses it onto specialized cells that convert the light to an electro-chemical signal that can be carried to and interpreted by the brain as an image. The process begins as light enters the eye through the cornea, the anterior most tissue of the eye (see Figure 5). The cornea partially focuses the light onto the crystalline lens, which further focuses the light to a microscopic image on the retina where specialized photoreceptor cells absorb the light and
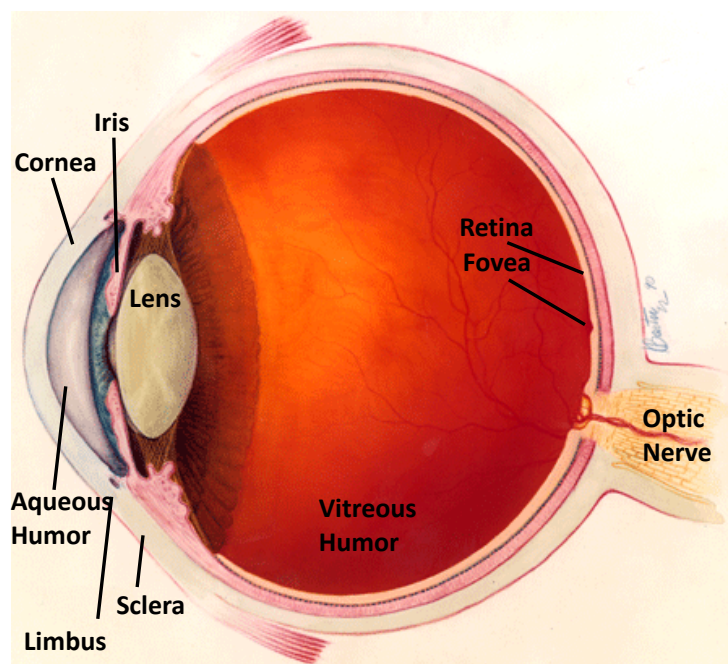
Figure 5. Diagram of ocular tissues and structures.

convert it to an electro-chemical signal that travels to the brain through the optic nerve. The cornea provides about two thirds of the focusing power of the eye by refracting light as it passes through its fixed curved shape. The crystalline lens provides about one third of the focusing capabilities and can change shape to focus on objects near and far from the observer. The aqueous humor fills the space between the cornea and the crystalline lens and supplies nutrients to the avascular cornea and lens. The vitreous humor fills the eye posterior to the lens.

The cornea has three major functions: it protects the inner eye by acting as a barrier to contaminants such as dust, bacteria and UV light; it provides a transparent window for light to pass into the eye; and it focuses light onto the lens. The cornea is composed of five avascular layers (see Figure 6):

(1) At the anterior surface there is an epithelial cell layer that rapidly regenerates to repair damage. It has approximately six cell layers. Tears hydrate the epithelium and maintain a very smooth interface with the air, critical for optimal refraction of light.

(2) Posterior to the epithelium is the Bowman's layer, a dense, acellular membrane composed of tightly woven type I collagen and heparin sulfate proteoglycans. The Bowman's layer is about 10 μm thick and protects the corneal stromal layer.

(3) Posterior to the Bowman's layer is the corneal stroma. The stroma accounts for the majority of the thickness of the cornea. It is approximately 500 μm thick at the center and thickens to 700 μm at the limbus. It is composed of about 300 stacked and interwoven layers [34] at the central cornea and increases to about 500 at the limbus [35], the junction between the cornea and the sclera. The layers, known as lamellae, are composed of predominantly type I collagen fibrils. The collagen fibrils are oriented parallel to one another within each lamella and approximately perpendicular to adjacent lamellae.
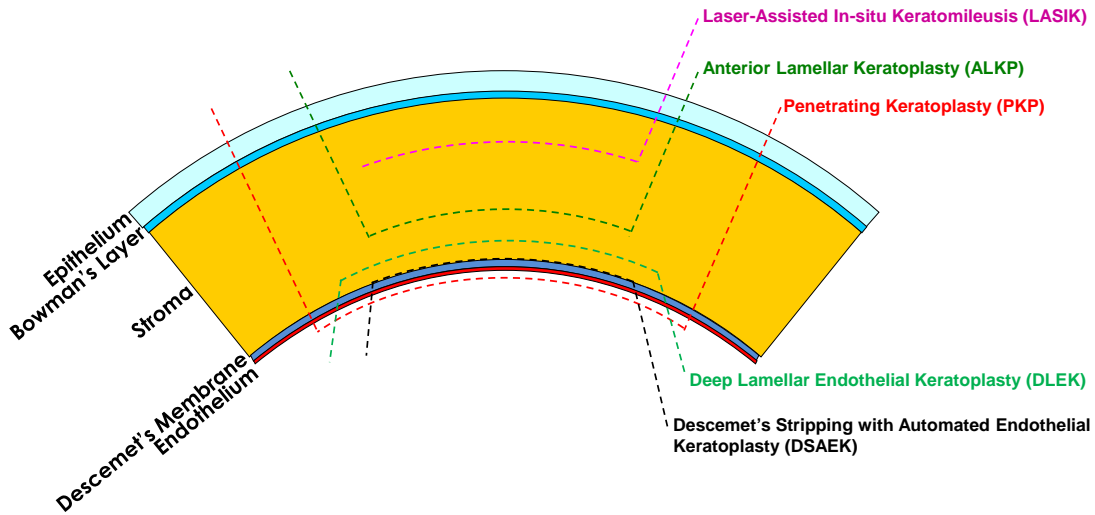
Figure 6. Corneal layer diagram and associated surgical cut morphologies.

Keratocytes are distributed throughout the stroma which repair and maintain the collagen tructure. The stroma provides much of the mechanical integrity of the cornea.

(4) Posterior to the stroma is the Descemet's membrane. It is thin, acellular, composed of type IV collagen and serves as a basement membrane to the endothelial layer.

(5) The most posterior layer of the cornea is a monolayer of endothelial cells that regulates stromal hydration by actively pumping fluid out of the cornea into the aqueous humor. Unlike the epithelial layer, the endothelial layer will not regenerate if damaged and below a critical cell density, the endothelium will lose its ability to regulate stromal hydration. This will cause the cornea to swell and lose its transparency which will decrease visual acuity.

It is common for many investigations having implications related to human corneas to use bovine corneas as analogs for practical and economic considerations. The layered structure of bovine corneas is identical to humans with the exception of the size scale. Bovine corneas are approximately twice as thick as human corneas, and have a proportionally thicker stromal layer

[36]. However both share very similar composition including similar stromal collagen organization and fibril size [37]. In the following investigations, both bovine and human corneas are used.

2.2.2 Common ophthalmic disorders and associate surgical therapies

The most common vision related disorder in the United States is refractive error, the inability of the eye to properly focus light onto the fovea. This can be due to improper corneal curvature, improper length of the eyeball, or an irregularity in the cornea or crystalline lens. These circumstances lead to the common visual impairments myopia, hypermetropia and astigmatism. Although refractive error can usually be corrected using eye glasses or contact lenses, many people choose a surgical method, LASIK, to eliminate the need to use glasses or contacts. This makes LASIK one of the most common surgical procedures in the United States with more than 800,000 procedures performed each year.

The objective of LASIK surgery is to reshape the cornea so that light is properly focused on the retina. The two step procedure begins with the creation of a circular flap by making a planar cut in the stroma, approximately parallel to the corneal surface. A hinge is left in the tissue and the flap is folded back (see Figure 6). In the second step, the cornea is reshaped by ablating the exposed stromal surface using an ultraviolet (UV) excimer laser before returning the corneal flap to its original position. Traditionally, the first step is performed with a microkeratome. More recently, FSLs have replaced the microkeratome in the majority of cases due to their precise and accurate flap creation, improved preservation of the epithelial layer, reduced induced astigmatism [20], reduced induced intraocular pressure, enhanced wound healing response [38], ability to create a wider range of flap dimensions and more advanced cutting morphologies, and reduced flap related complications [18, 19].

14

One of the latest and promising techniques for correcting refractive error, called small-incision lenticule extraction (SMILE), use the FSL to cut out an intrastromal lenticule which can then be removed through a small incision in the cornea. This technique improves upon LASIK by eliminating the need for a second laser and producing only a small incision instead of a flap in the cornea.

Another common ophthalmic surgical procedure that has benefited from FSLs is keratoplasty. In this procedure, the full (penetrating) or partial thickness (lamellar) of the cornea is surgically removed and then replaced with that of a donor cornea. Indications for this procedure are broad and include corneal damage, infection, and diseases and their sequelae that impede vision by reducing the optical performance of the cornea. Often, this may be the result of a dysfunctional endothelium. There are several types of lamellar keratoplasty for treating different indications (see Figure 6), all of which are more challenging for a surgeon to perform than penetrating keratoplasty due to size scale and delicacy of the procedure. All keratoplasty types have benefited from the superior positioning, precision and the ability of the laser to produce intricate cut morphologies that allow improved graft integration and retention [39, 40]. Further, procedures with FSLs result in less damage to the critical endothelial layer than traditional manual techniques [41]. These advantages result in quicker healing times and reduced astigmatism [14, 15].

For many of the same reasons, the unique advantages of using FSLs has improved cataract surgery, the most commonly performed surgical procedure in the United States [27] and the world [28] with 19.7 million procedures performed worldwide in 2012 [29]. A cataract is the term for the crystalline lens after it has become cloudy and dramatically reduces visual acuity. To improve vision, the cataract is surgically removed and a synthetic lens implant, called an

15

intraocular lens (IOL), is positioned in its place. The laser is used to replace three of the steps in cataract surgery. First, it can create the corneal incisions necessary to access the lens. One of the most critical steps in cataract surgery is the capsulorhexis, the creation of a centered, circular cut in the lens capsule that provides access to the cataract. The capsulorhexis is considered to be one of the most difficult surgical techniques to master. The centration and circularity of this circular cut has a direct effect on the performance of the implanted IOL. This is especially true in the case of high performance aspheric, multifocal and accommodating IOLs where small alignment errors translate to significant visual effects that can be incapacitating [42, 43]. In addition, an improperly sized capsulorhexis can lead to posterior capsule opacification, the most common complication of cataract surgery, and miscalculation of the necessary IOL power, both of which require follow up treatments to correct [43]. FSLs create a capsulorhexis that is more circular, centered and sized than manual techniques resulting in better IOL performance [42-44].

The third step in cataract surgery is the breakdown and removal of the cataract. This is typically performed through a process known as phacoemulsification where by a specialized tool inserted into the lens capsule produces ultrasonic vibrations that break up the dense cataract and simultaneously aspirate the created particles. One of the possible side effects of this procedure is damage to the endothelial layer leading to a decreased endothelial cell count [45, 46]. Using FSLs to fragment the lens has been shown to reduce or eliminate the need for phacoemulsification with the benefit of reduced endothelial cell loss [47-49]. Although FSL use in cataract surgery currently accounts for only a small proportion of these procedures, it is expected that FSL use will soon become routine [50].

In addition to these three major procedures, LASIK, Keratoplasty and Cataract surgery, there are several other applications that employ the use of FSLs. FSLs are being used to correct

16

astigmatism, both naturally occurring and induced by previous surgical procedures, by making small strategically located and sized incisions in the cornea known as astigmatic keratotomy and limbal relaxing incisions. Compared to manual techniques, the FSL is more precise, stable and can more accurately achieve the correct length, depth and optical zone of the incisions [18]. FSLs can be used to cut tunnels in the cornea for implanting intrastromal ring segments for treating Keratoconus, a disease that causes the cornea to grow into a conical shape. Gliding planes can be cut into the lens to restore flexibility in patients suffering from presbyopia, the hardening of the lens. Reduced lens flexibility reduces the ability of the eye to focus on close objects. Whereas most applications of FSL technology improve existing techniques, this procedure didn't exist before FSL technology.

2.2.3 Femtosecond laser classes

The term FSL includes a broad range of laser types with the only inclusion criteria being that pulse duration must be in the femtosecond time domain. This includes FSLs having pulse durations of only a few femtoseconds used in femto-chemistry [51] applications as well as sub-picosecond pulse durations used for x-ray sources [52]. Other laser parameters such as repetition rate and pulse energy can vary even more widely. Picojoule pulse energies (10^{-12} J) are used in cellular surgery applications [53] while millijoule pulse energies (10^{-3} J) are used in microfabrication applications [54]. Even within a single application, ophthalmic surgery, there is a range of laser parameters. Current FSL-based medical devices for ophthalmic surgery are solid-state infrared lasers that can be grouped into two classes illustrated in Figure 7. Conventionally used clinical FSLs are characterized by high pulse energies and low pulse repetition frequencies in the microjoule (10^{-6} J) and kilohertz (kHz) range, respectively. More recently, a new class of FSLs exhibiting low pulse energies and high pulse repetition frequencies in the nanojoule (10^{-9} J)

17
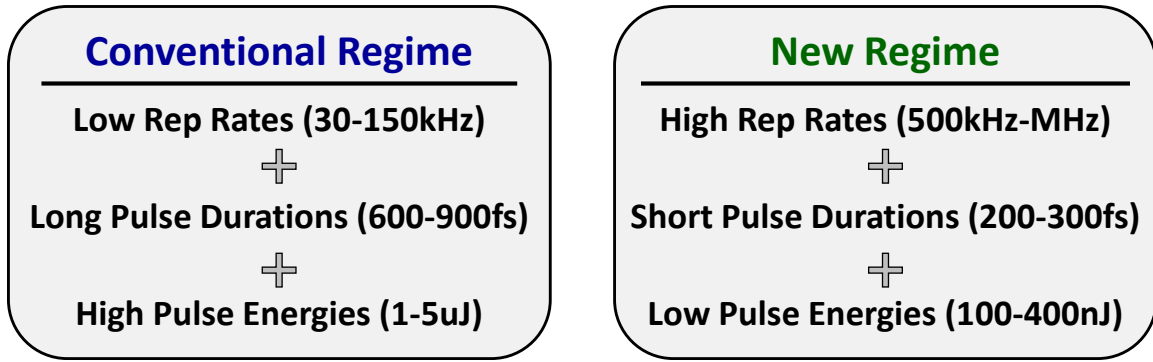
Figure 7. Laser parameters associated with two therapeutic femtosecond laser classes.

and megahertz (MHz) range, respectively, has emerged [19, 55, 56]. As a consequence of their respective parameters, the two FSL classes require different laser scanning parameters such as laser spot spacing required to generate the continuous tissue cutting effect in ocular tissues. Low energy FSLs destroy smaller volumes of tissue and therefore, laser spots need to be located closer together in comparison with higher energy FSLs (Figure 8). Higher pulse repetitions frequencies are therefore favorable with low energy FSL systems in order to have similar procedure durations as high energy systems. Additionally, closer spacing of smaller spots results in smoother tissue cutting [57], but more total energy delivered to the tissue [56].

Currently, there are seven FSL devices FDA approved for creating corneal flaps during LASIK. The Intralase system (Abbot Medical Optics) has been used in the vast majority of FSL based LASIK procedures. Since its introduction in 2002, the Intralase system has evolved from having pulse repetition frequency and pulse energy of 15 kHz and 10 µJ, respectively, to its current parameters of 150 kHz and 1 µJ. Some of the FSL devices approved for LASIK flap creation are also approved for keratoplasty, astigmatism correction, stromal tunneling and other corneal incisions. There are also four FSL devices approved for use in cataract surgery. All of these devices vary to some extent regarding laser parameters.

Conventional Regime　　　　**New Regime**
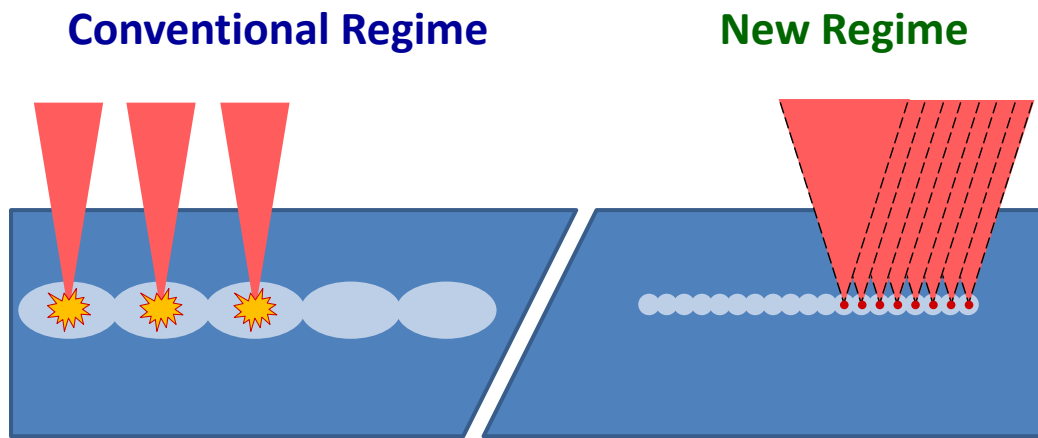
Figure 8. Photodisruption models associated with two therapeutic femtosecond laser classes.

Chapter 3 - Femtosecond Laser–Tissue Interactions

3.1 Ocular tissue optical properties

In order to understand how optical radiation propagates through a material, the optical properties of the targeted material must be considered. The amount and quality of light reaching specific locations will largely be determined by the initial properties of the light source as well as the optical absorption, scattering and refractive index of the material through which the light propagates. There are several possible phenomena that can occur as light propagates through the ocular tissues: (1) light can be transmitted to the retina directly; (2) it can be totally or partially absorbed by the tissue components; (3) it can be scattered in a random direction; or (4) it can be reflected in the direction from which it came. All four of these events occur in the eye.

Absorption and scattering of photons will collectively decrease the amount of forward propagating light reaching the retina. The attenuation coefficient (α), measured in units (cm^{-1}), accounts for both absorption and scattering and varies with the wavelength of light. It is necessary that the ocular tissues have low attenuation coefficients in the visible spectrum so that enough light reaches the retina to be sensed. Simultaneously, high attenuation coefficients in the UV spectral range are important to protect the sensitive retina and lens from phototoxic damage. The other important optical property to consider is the refractive index (n), which describes the speed of light in a given material, at a specific wavelength, with respect to its speed in a vacuum. The trajectory of light traveling from one material into another will change according to the ratio of refractive indices of the two materials, a process known as refraction. The eye focusses light

onto the retina through refraction. In addition, changes in refractive index lead to reflection from surfaces and scattering from particles which are encountered during propagation. In order to predict how light will behave in the eye, each tissue in the optical path from the anterior surface of the cornea to the retina must be considered.

3.1.1 Cornea

The cornea is the first ocular tissue light encounters during visual sensation. This first interface between air and tissue is very important since this is the largest change in refractive index that light will encounter on its path to the retina. Air and cornea have refractive indexes of approximately 1 and 1.376, respectively [58]. This large change in refractive index, combined with the curved shape of the cornea, provide about two thirds of the focusing power of the eye. Light scatter from the surface is reduced to negligible values by a thin tear film that maintains an extremely smooth optical interface. However, there is a significant Fresnel reflection from the surface of the cornea due to the large difference in refractive index. It is known as the first Purkinje image [59]. There are three more reflections produced at the cornea-aqueous humor, aqueous-crystalline lens and crystalline lens-vitreous interfaces, the second, third and fourth Purkinje images, respectively. However, these are relatively small reflections in comparison with the first image.

Optical transmission through the cornea is high and relatively flat through the visible spectrum due to a low uniform attenuation coefficient. Human vision perceives light from about 390 nm to 780 nm [58]. Over this range corneal transmission increases from about 80% to 95% [60-62]. Theoretically, the stromal collagen should scatter approximately 90% of incident light; however, there is only a minimal amount of scattering in the visible range. This effect is attributed primarily to the quasi-ordered structure of the stroma collagen [63]. Destructive

interference reduces the scattered light to almost zero in all directions except for the direction of propagation of the incident wave [63]. The majority of the minor scattering that does occur is due to the presence of keratocytes within the stromal layer. Cell nuclei present a change in refractive index with respect to the surrounding cell cytoplasm. Within the cytoplasm, there is a high concentration of crystalins, proteins that serve to match the refractive index of the stromal ground substance to the keratocyte cytoplasm and therefore reduce scattering to interactions with the higher index cell nuclei [64].

The cornea serves to protect underlying structure from UV light by absorbing in part the UV light entering the eye. UV light can be divided into three sub-groups as recommended by Commission de l'Eclairage (CIE), The International Commission on Illumination [65]: UVA (315-400 nm); UVB (280-315 nm); and UVC (100-280 nm) (Table 1). The cornea absorbs more than 99% of light below 295nm and partially attenuates UVB and UVA [66]. The main chromophores in the cornea are DNA and protein.

Table 1. Spectral range definitions according to Commission de l'Eclairage (CIE), the International Commission on Illumination.

Radiation Term	Wavelength Range
Ultraviolet C	100 nm to 280 nm
Ultraviolet B	280 nm to 315 nm
Ultraviolet A	315 nm to 400 nm
Visible	400 nm to 760 nm
Infrared A (near)	760 nm to 1400 nm

In addition to the high transmission and low scattering provided by the organization of the stromal collagen, the cornea is also substantially birefringent. The cornea is optically anisotropic having 3 principal refractive indexes. The fast axis (lowest refractive index) is the *z*

22

axis or optical axis (see Figure 9) which is perpendicular to the corneal surface. The *x* and *y* axes are tangential to the corneal surface and approximately perpendicular to each other.
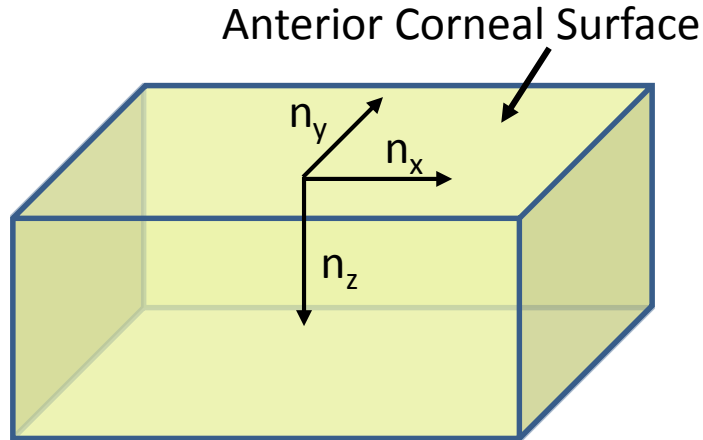
Figure 9. Principal refractive index axes of the cornea.

3.1.2 Aqueous humor

Similar to water, the aqueous humor (98% water) has high transmission of visible, IR light up to about 1100 nm, and to a slightly lesser extent, UVA. Transmission of UVB decreases with wavelength from about 70% to 10%. Any UVC transmitted through the cornea will be absorbed by the aqueous [61].

3.1.3 Crystalline lens

The remainder of the UV spectrum not absorbed by the cornea or aqueous humor (mostly UVA) is absorbed by the lens. The chromophore 3-hydroxykyurenines safely dissipates UVA energy to protect the lens and retina from photo-damaging effects until the middle ages. At this point, the enzyme kynurenine aminotransferase is produced at higher rates, which converts the protective 3-hydroxykyurenines to xanthurenic acid. This chromophore produces reactive oxygen species (ROSs) upon absorption of UV light which damage lens proteins, eventually leading to cataract formation. Tryptophan, an endogenous chromophore is photooxidized to *N*-formyl kynurenine

23

which can also generate ROSs upon further UV absorption [67]. The lens has high transmission in the VIS and IR spectral range from approximately 420 nm to 1100nm [61].

3.1.4 Vitreous humor

This gelatinous substance is 98-99% water with collagen and hyaluronic acid the other major components. The transmission properties are very similar to the aqueous in the UV and visible regions, but decreases rapidly above 950 nm.

3.2 Human and bovine corneal transmission measurements

It is very important to understand the spectral transmission properties of the cornea, not only because laser radiation passes through the cornea in all FSL-based, ophthalmic surgical procedures, but as later investigations show, FSLs are capable of changing the spectral properties of the therapeutic laser due to laser-tissue interactions in the cornea. Corneal transmission will determine the power spectral density of light reaching the lens and deeper tissues.

Many previous attempts to measure corneal transmission properties use less than ideal sample preparations that diverge from the natural shape of the cornea, inducing surface irregularities and possibly altering the physical properties of the collagen. Usually this includes placing the corning between two glass slides to maintain a uniform surface, perpendicular to the incident light [61, 68]. Some studies have measured the cornea transmission by placing a sensor within the intact eye [69, 70]. This technique doesn't isolate corneal transmission properties from other ocular tissues. To address these limitations and provide transmission properties for the same corneal samples that will be used in subsequent studies, cornea transmission of bovine and human corneal tissue was measured using an adapted commercial spectrophotometer.
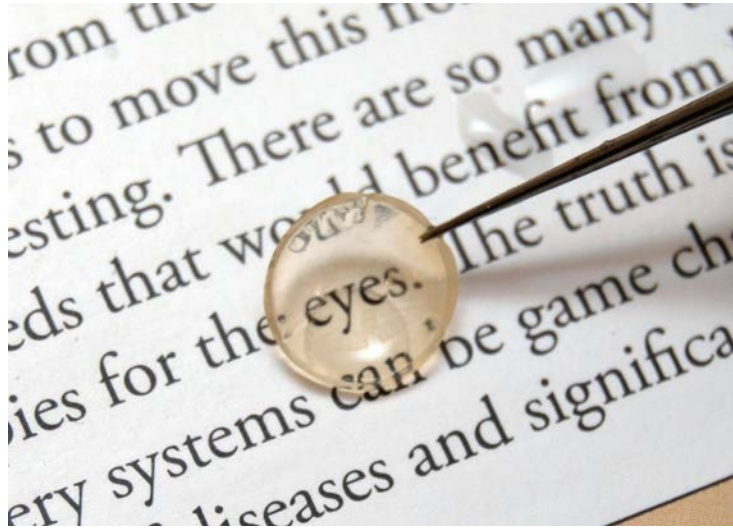
Figure 10. Appearance of gamma-irradiated corneal graft tissue. Reprinted with permission from W. R. Calhoun, E. K. Akpek, R. Weiblinger, and I. K. Ilev, "Evaluation of broadband spectral transmission characteristics of fresh and gamma-irradiated corneal tissues," Cornea, vol. 34, pp. 228-34, Feb 2015. Copyright 2015, Wolters Kluwer Health Lippincott Williams & Wilkins©.

The transmission measurements also serve to compare the optical performance of a recently developed corneal tissue graft for use in keratoplasty to replace traditional graft tissue. This graft is a product of a novel processing method for sterilizing corneal tissue that utilizes gamma irradiation to induce cell apoptosis and disrupt plasma membranes to terminally sterilize the graft without interfering with clarity (Figure 10). The shelf life of these irradiated donor lenticules is two years at room temperature which translates into minimum handling requirements after packaging. Although there are more than 8 million blind individuals due to corneal maladies worldwide [71], only about 100,000 keratoplasty procedures were performed worldwide [72]. A substantial number of these individuals are otherwise healthy in their productive stages and can have their vision restored through donor corneal transplantation. The typical source for these procedures is a cadaveric cornea that is stored in a specific environment using a physiologic supportive solution to maintain the clarity and cell function of the tissue. The harvesting, assessing of suitability for transplantation, storing and distribution of donor tissues

are generally managed by eye banks. Unfortunately, in many areas of the world there is limited eye banking and available fresh corneas due to a multitude of difficulties including shortage of donations, exclusion of corneas not meeting transplantation specifications, short shelf-life of suitable fresh corneas, and high-cost of eye banking [73], which severely limits the number of transplantations worldwide [72]. This graft tissue has the potential to improve the lack of available high-quality donor tissues outside of the United States, particularly in the developing world where corneal blindness is most prevalent.

In this study [74], broadband UV, visible and near-IR (200-850 nm) spectral transmission through full-thickness human and bovine corneas and full- and partial-thickness gamma-irradiated, sterile corneas was measured.

3.2.1 Materials and methods

Cornea Samples

Five cornea types divided into two groups were used. One group consisted of freshly acquired, unstored bovine and human corneas. The second group consisted of human graft tissues, fresh corneal grafts and irradiated full- and partial-thickness corneal grafts. Bovine whole globes were obtained from a local slaughterhouse and fresh and gamma-irradiated (VisionGraft) human cornea and corneal graft tissue samples were provided by Tissue Banks International (Baltimore, Maryland). The gamma-irradiated sterile tissue is comprised of a clear, decellularized stromal collagen matrix and a devitalized endothelium with Descemet's membrane. The tissue is stored at room temperature in sterile glass bottles in a proprietary albumin solution. The fresh human corneal grafts were transplantation quality and had been stored in Optisol corneal storage medium (Bausch and Lomb Inc. Rochester, NY) at 6 C° for no longer than 6 days prior to experiments. The epithelium was removed from all human cornea graft tissues. The freshly

excised, unstored bovine and human corneas had all layers intact and were transported in containers with balanced salt solution (BSS, Alcon, Ft Worth, TX).

All fresh corneas were trephined carefully using 8 mm disposable punch trephines. Irradiated corneas were pre-cut in the same diameter and had been irradiated between 15 and 24 weeks prior to use. Spectral transmission measurements were performed on 15 corneal buttons: 3 irradiated full-thickness human cornea grafts; 3 irradiated 100-μm-thick human cornea grafts; 3 fresh full thickness human cornea grafts; 3 fresh full-thickness bovine corneas; and 3 fresh full-thickness human corneas. Human cornea grafts were evaluated in a masked fashion and all experiments were performed using the same technique, regardless of the type of the tissue.

Spectral Transmission Measurement

Prior to the spectral transmission measurements, each corneal graft button was removed from its storage solution using a sterile 0.12 forceps gently grasping the periphery of the tissue, dipped in BSS for 5 seconds to wash the storage solution, and then placed on a customized aperture on the integrating sphere for measurement. Fresh tissues were directly placed on the aperture. A thin plate with a 5mm aperture was created for centering the cornea and sampling the center 5 mm. Care was taken to ensure that corneal samples maintained their natural curvature throughout the measurement. When the measurement was complete, the cornea was removed from the aperture, rewashed and returned to the aperture for the next measurement. Each graft tissue was measured 3 times and all others once. Before each cornea was placed onto the aperture, a 100% transmission measurement was made. Each process took less than 60 seconds and did not allow the corneal tissue to dry. Using similar procedures, transmission measurements for each storage solution and deionized water were also recorded using a 1-mm optical path quartz cell and the same aperture. To compare with a standard accepted transmission curve, transmission through a

typical single-piece acrylic intraocular lens implant with 6-mm optic (SA60AT, Alcon, Ft Worth, TX) was measured using similar procedures.

The spectral transmission of broadband light in the UV, visible and near-IR, through the corneal tissues was measured using a commercial spectrophotometer (Perkin-Elmer Lamda 950). Transmission data was collected for light with wavelength from 199 nm to 850 nm with a 3-nm step size for graft tissues and 320 nm to 850 nm with a 2-nm step size for all others. Figure 11 shows a diagram of the corneal spectral transmission measurement system. Broadband collimated light passes through the cornea and is collected and distributed by the integrating sphere. A photodiode detector measures the intensity of the light and returns the transmission at each wavelength normalized to a 100% scan taken with no cornea present on the thin aperture plate. A baffle prevents direct illumination from the aperture/cornea. Spectral transmission measurements in cornea [61, 68] as well as other materials [75, 76] using similar approaches are well accepted.
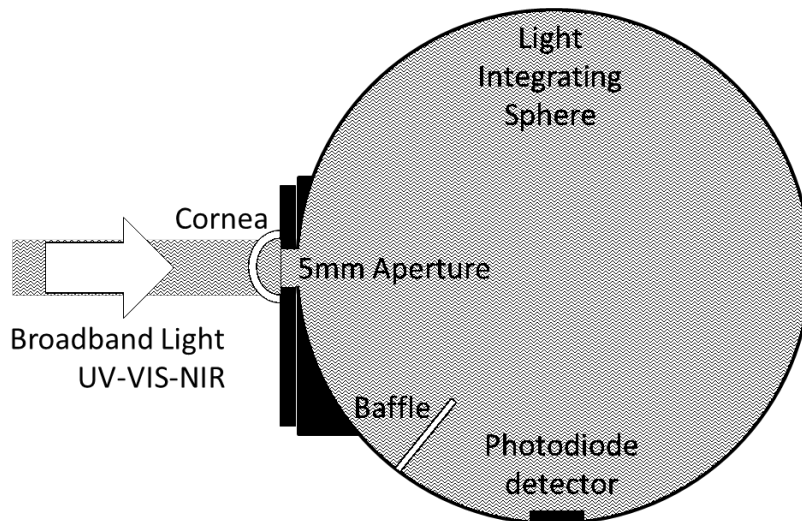
Figure 11. Corneal spectral transmission measurement apparatus. Reprinted with permission from W. R. Calhoun, E. K. Akpek, R. Weiblinger, and I. K. Ilev, "Evaluation of broadband spectral transmission characteristics of fresh and gamma-irradiated corneal tissues," Cornea, vol. 34, pp. 228-34, Feb 2015. Copyright 2015, Wolters Kluwer Health Lippincott Williams & Wilkins©.

Statistical Analysis

To determine whether irradiated corneal graft transmission values are comparable to standard fresh cornea grafts, a one tailed t-test was performed, also known as a non-inferiority test[77], using $\alpha = 0.05$ and $\delta = 2.5\%$. Comparisons were made using average transmission values at 424 nm, 451 nm, 499 nm, 550 nm, 601 nm, 649 nm and 700 nm to cover the relevant photoreceptor sensitive spectrum. In addition, 95% confidence intervals were generated for estimating the true mean transmission values of irradiated cornea at wavelengths covering the UV and visible spectral regions.

3.2.2 Results

Figures 12(a), 12(b), and 12(c) summarize the spectral transmission curves for all measurements performed for human graft tissues. Repeat transmission measurements for each graft cornea agreed well with only minor variation for all corneas. However, transmission values differed significantly for one of the irradiated 100-µm-thick human corneas. The broadband decrease in transmission in irradiated cornea 2 was most likely caused due to the inability of this tissue to maintain its natural curvature when mounted on the integrating sphere aperture causing increased back reflection. Transmission values from this cornea were excluded from analyses.

Cornea transmission curves were averaged to produce a single representative curve for each cornea type (Figure 13 (a)). Average transmission for corneal solutions and related media were measured and plotted in Figure 13(b). All human cornea types had high transmission (> 90%) in the near-IR and most of the visible wavelengths, decreasing transmission in the UVA spectral region and very low transmission below 290 nm (< 2%). The irradiated 100-µm-thick cornea had the highest transmission through the visible region. Both full-thickness and 100-µm-thick irradiated cornea tissues had smooth decays in transmission from visible to UV
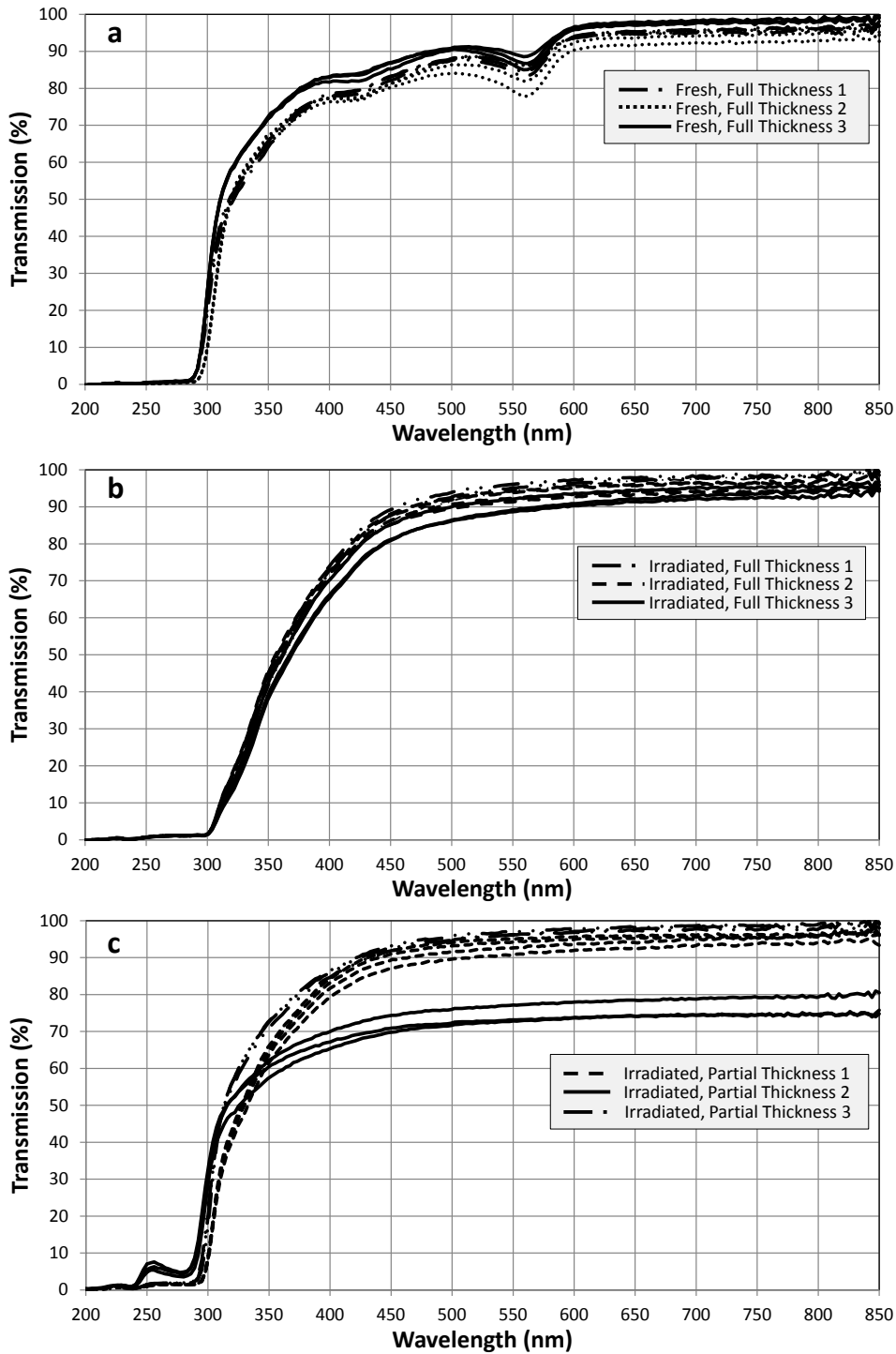
Figure 12. Spectral transmission measurements of: (a) fresh full thickness donor corneal tissue; (b) gamma-irradiated, full thickness donor corneal tissue, and (c) gamma-irradiated, partial thickness donor corneal tissue. Reprinted with permission from W. R. Calhoun, E. K. Akpek, R. Weiblinger, and I. K. Ilev, "Evaluation of broadband spectral transmission characteristics of fresh and gamma-irradiated corneal tissues," Cornea, vol. 34, pp. 228-34, Feb 2015. Copyright 2015, Wolters Kluwer Health Lippincott Williams & Wilkins©.
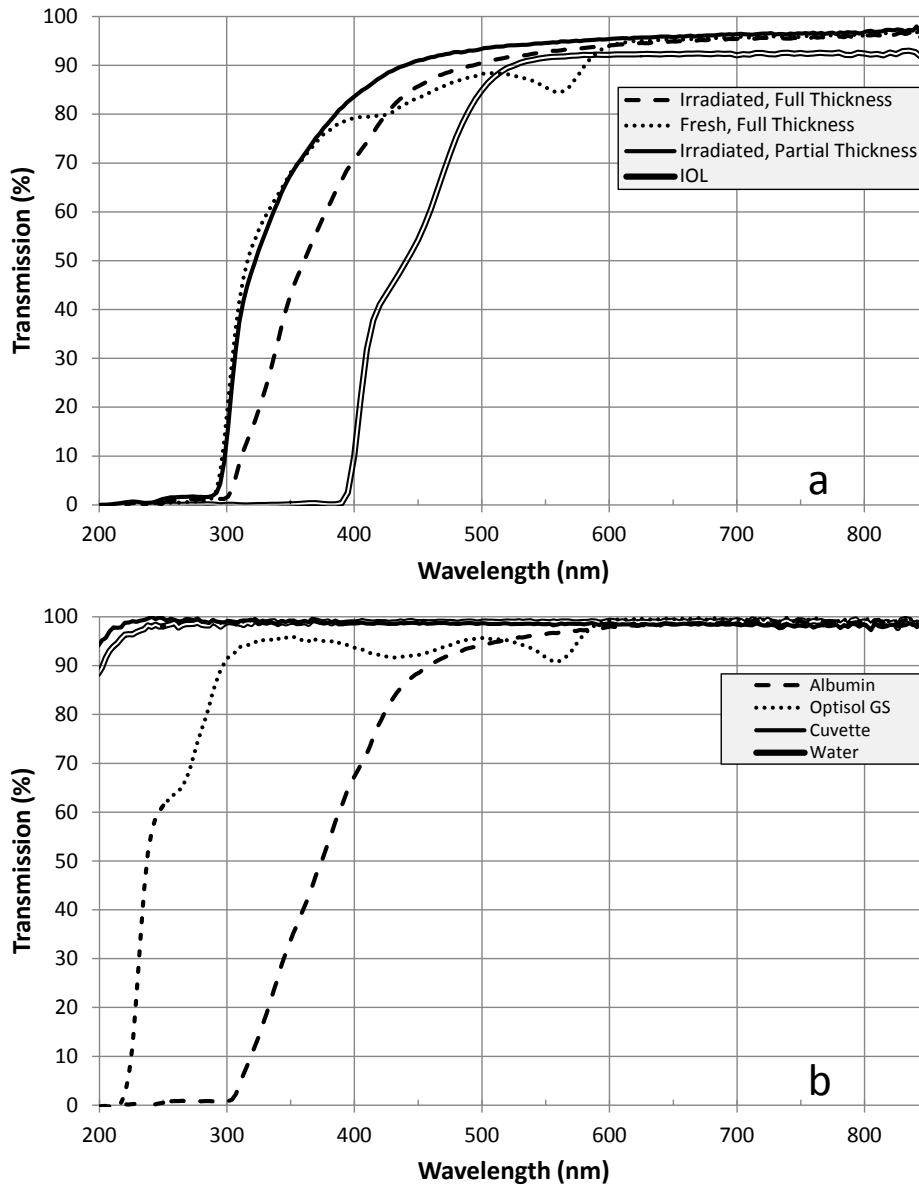
Figure 13. Average spectral transmission measurements for: (a) corneal tissue types and IOL; and (b) associated storage media. Reprinted with permission from W. R. Calhoun, E. K. Akpek, R. Weiblinger, and I. K. Ilev, "Evaluation of broadband spectral transmission characteristics of fresh and gamma-irradiated corneal tissues," Cornea, vol. 34, pp. 228-34, Feb 2015. Copyright 2015, Wolters Kluwer Health Lippincott Williams & Wilkins©.

wavelengths. The most notable differences between cornea types occurred between approximately 300 nm and 575 nm. The transmission decay in fresh corneas was characterized by two absorption peaks at 560 nm and 435 nm.

Fresh bovine corneal transmission followed a similar trend to human cornea, but had values approximately 15-20% lower throughout the visible and near-IR spectrum (Figure 14). Human and bovine corneal transmission converged in the UVA spectral region.

Transmission spectra for the storage solutions for irradiated (Albumin) and fresh cornea grafts (Optisol) also showed differences which corresponded to the characteristics of their respective corneas (Figure 13(b)). The Optisol storage solution had decreases in transmission at 435 nm and 560 nm that correspond exactly with those observed in the fresh corneal tissues. In addition, Optisol had much higher transmission below 450 nm than the albumin storage solution, similar to fresh and irradiated cornea transmission respectively. As expected, deionized water and the quartz cell had very high transmission across the entire spectrum. In general, transmission through all cornea types was higher than intraocular lens implant transmission.

Average transmission values and p-values associated with the non-inferiority test are summarized in Table 2. Throughout the visible region, irradiated cornea transmission was as good as, or better than, fresh cornea.

3.2.3 Discussion

The results of this study demonstrate similar trends in light spectral transmission properties of all tissue types tested. All tissue samples displayed high transmission throughout the visible range and strong attenuation below 300 nm wavelengths. Bovine transmission in the near-IR and visible spectral regions was shifted lower, but this was expected since bovine corneas are approximately twice as thick as human corneas and have a more actively exfoliated epithelium [36].

Some differences in transmission between irradiated versus fresh corneas were noted between 300 nm and 575 nm. Although the corneas were washed prior to measurement, they
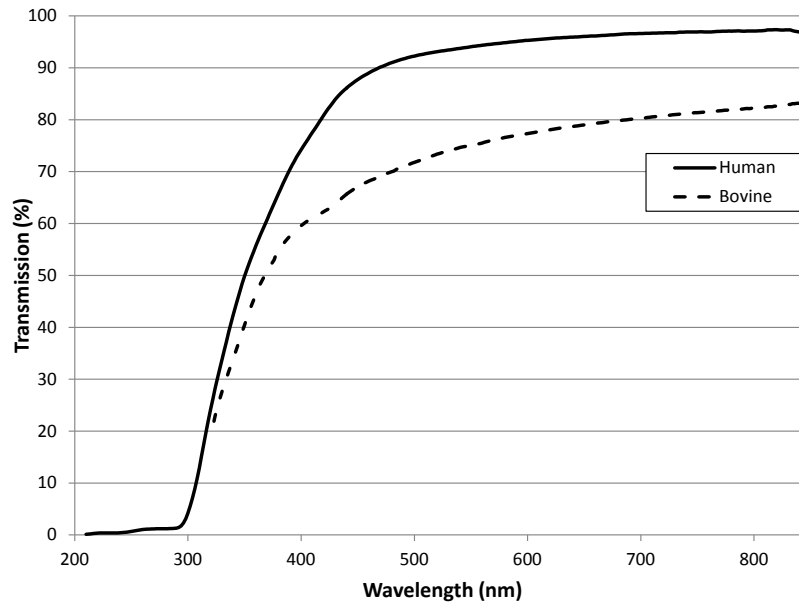
Figure 14. Average transmission measurement of freshly excised human and bovine corneal tissue. Reprinted with permission from W. R. Calhoun, E. K. Akpek, R. Weiblinger, and I. K. Ilev, "Evaluation of broadband spectral transmission characteristics of fresh and gamma-irradiated corneal tissues," Cornea, vol. 34, pp. 228-34, Feb 2015. Copyright 2015, Wolters Kluwer Health Lippincott Williams & Wilkins©.

appeared to retain some of the storage solution within the stroma. The differences in transmission between the two cornea types seemed to be due to differences in storage solution rather than differences in corneal characteristics. The two absorption peaks seen in the fresh corneas are likely due to absorption by Optisol, as identical peaks were seen in this solution's transmission spectrum. Previous studies using freshly excised tissues without storage solution did not demonstrate these decreases in transmission [60, 69]. Furthermore, albumin exhibits strong absorption below 400 nm [78] which likely explains the lower UV transmission in irradiated lenticules. There was a significant decrease in UV transmission with respect to fresh cornea at 300 nm ($p<0.0005$), 349 nm ($p< 0.0005$) and 400 nm ($p<0.005$). This would be an added benefit as this spectral region is cataractogenic [67, 79]. Nevertheless, the effects of

storage solution on light transmission are likely temporary, as the remaining intrastromal storage solution will be replaced with aqueous fluid following grafting of the tissue.

Irradiated, full-thickness cornea transmission in the visible spectral region was equal to or greater than fresh, full-thickness cornea at selected wavelengths representing the relevant photoreceptor sensitive spectrum [80] (Table 2 and Figure 15). All comparisons resulted in p-values less than 0.05. Further, 95% confidence intervals for irradiated cornea transmission in the visible spectral region were comparable to previous studies [60, 69, 81] measuring corneal transmission.

Table 2. Average corneal transmission and P-values of non-inferiority test as selected wavelengths representing the retina-sensitive, visual spectrum.

	424nm	451nm	499nm	550nm	601nm	649nm	700nm
Sterile Cornea Transmission (%)	79.73	85.83	90.42	92.71	94.12	94.89	95.42
Fresh Cornea Transmission (%)	79.85	83.43	88.09	85.51	94.12	95.27	95.77
P-value	0.041	<0.001	<0.0005	<0.0001	0.011	0.020	0.016

The major light attenuating structures of the cornea are the epithelium, Bowman's layer and stroma. Although the epithelium and Bowman's layer have absorption coefficients approximately 2 and 3 times higher than stroma, respectively, the stroma is significantly thicker and provides the majority of the attenuation in the 300-400 nm range [66]. Therefore, the high transmission seen in the 100-µm irradiated cornea is expected. Not only is it lacking an epithelial layer, but the stroma is also significantly thinner, both of which increase light transmission, especially in the UV region where absorption is the strongest [66]. Further, the UV-attenuating intrastromal storage solution effect should be minimal due to significantly less solution contained within this thinner tissue.

34
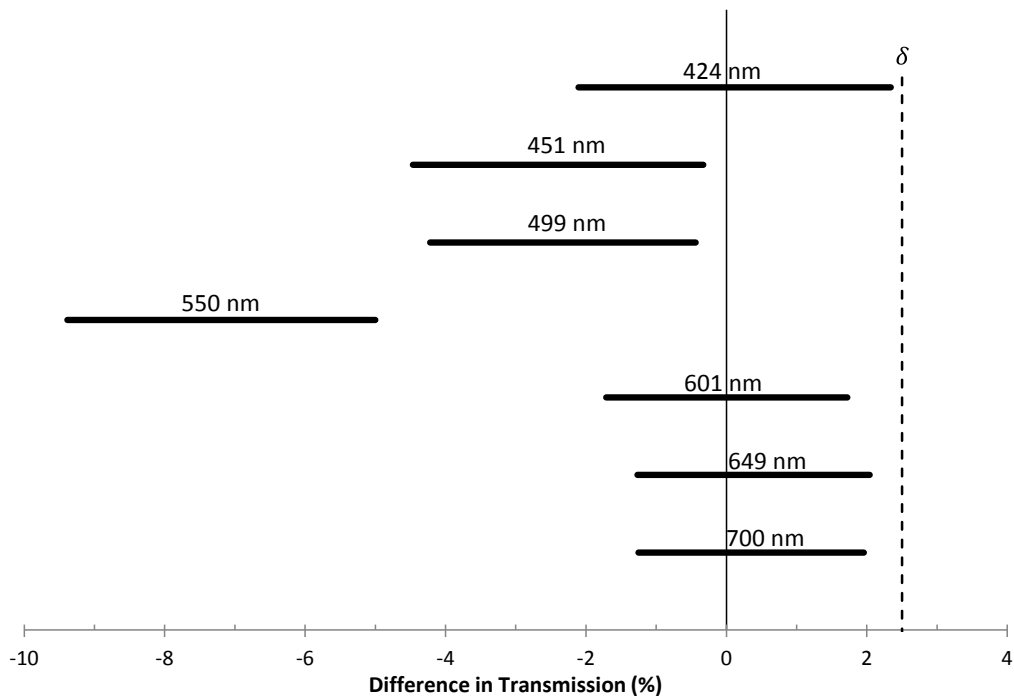
Figure 15. 95% confidence intervals for the true difference in transmission (fresh – irradiated) at selected wavelengths covering the retina-sensitive, visual spectrum with δ=2.5%. Reprinted with permission from W. R. Calhoun, E. K. Akpek, R. Weiblinger, and I. K. Ilev, "Evaluation of broadband spectral transmission characteristics of fresh and gamma-irradiated corneal tissues," Cornea, vol. 34, pp. 228-34, Feb 2015. Copyright 2015, Wolters Kluwer Health Lippincott Williams & Wilkins©.

In this study, it was found that bovine corneal transmission properties have similar behavior to those of human corneal tissue, but at slightly decreased values. It was also shown that gamma irradiated sterile corneal tissue grafts have spectral transmission characteristics as good as or better than fresh, traditionally used corneal grafts in the visible spectral range, with both tissue types having better transmission than a standard intraocular lens implant. Both tissue types have similarly strong attenuation of damaging UV wavelengths. The results suggest that in regards to the light transmission properties, irradiated corneas are suitable for corneal lamellar grafting procedures that do not require a viable endothelium.

3.3 Bovine corneal birefringence measurements

In all ophthalmic surgical procedures that utilize an FSL, the therapeutic laser beam must pass partly or entirely through the cornea. Therefore, the cornea's optical properties will affect the laser beam parameters and ultimately LIB as well as any other NOEs generated during FSL-tissue interactions. An important factor in most nonlinear processes is the polarization of the laser's electric field. HG)is a polarization dependent process [82] that can occur in the corneal stroma [83, 84]. Recent publications also indicate that laser polarization may affect FSL ablation [85, 86]. Therefore, it is important to understand how the laser polarization will change as it passes through corneal tissue.

The cornea is a birefringent material due to the highly oriented stromal collagen [87]. Born and Wolf showed that corneal birefringence has two sources: intrinsic and form birefringence [88]. Intrinsic birefringence originates from individual type 1 collagen fibrils which are uniaxially birefringent, having a higher refractive index along the length of the fibril than across [89]. Form birefringence occurs due to the parallel assembly of long and thin collagen fibrils embedded in a ground substance of different refractive index. This also generates uniaxial birefringence. Form birefringence accounts for approximately two thirds of the total corneal birefringence, the sum of both intrinsic and form [90, 91]. Although the exact organization of collagen fiber bundles is debated, most groups agree that the overall biaxial model of birefringence is a result of the layered structure of the lamellae [92]. The optical (fastest) axis is perpendicular to the corneal surface, the slowest axis is oriented in a supertemporal-inferonasal direction and parallel with the corneal surface and the second slow axis approximately perpendicular to the others [93, 94].

The purpose of this investigation is to better understand how FSL laser beam polarization changes as it passes through birefringent corneal tissue as it approaches the treatment site. This will allow for a better understanding of the laser beam parameters directly responsible for the treatment effect and other NOEs, and it will improve the ability to optimize the surgical process. In this work, a versatile methodology that includes an experimental system and analytical model developed for precise quantitative measurement and evaluation of phase retardation in corneal tissues using an FSL is demonstrated. The experimental system and methodology will allow future testing of different FSL laser parameters to determine their effect on corneal birefringence. The experimentally and theoretically validated results confirm the system's high accuracy and repeatability for quantifying cornea phase retardation effects [95].

3.3.1 Materials and methods

Cornea preparation

Freshly enucleated bovine whole globes were obtained from a local slaughterhouse and stored in minimum essential medium with HEPES (Sigma). The corneas were excised immediately prior to testing. The cornea was placed into a cradle (see Figure 16) with storage solution to maintain its natural shape and hydration. The cradle was sealed to a glass slide to maintain an optical window and to applanate a small central region of the cornea to be tested. The corneas were tested less than 6 h after enucleation.

Figure 16. Cornea cradle diagram. Reprinted with permission from W. Calhoun, R. Weiblinger, A. Beylin, and I. K. Ilev, "Assessing the phase retardation in corneal tissues using a femtosecond laser," Rev Sci Instrum, vol. 84, p. 084301, Aug 2013. Copyright 2013, AIP Publishing LLC.

Optical Setup

The principal optical setup for quantification of phase retardation in corneal tissue is illustrated in Figure 17. The corneal tissue was placed between two Glan-Laser type polarizing beam splitters (PBS) (Thorlabs) rotated so that their transmission axes are 90 degrees relative to each other. The cornea sample was positioned between the two polarizers on x-y translation and rotational stages (Thorlabs). Transmission of a femtosecond fiber laser (1064 nm, 560 fs, 18 nJ, 80 MHz, Fianium) was measured with a laser photodiode sensor (Ophir Photonics) after the second polarizer (analyzer) as the tissue was rotated. A computer was used to control and correlate the stage position and power measurements using LabVIEW programs.
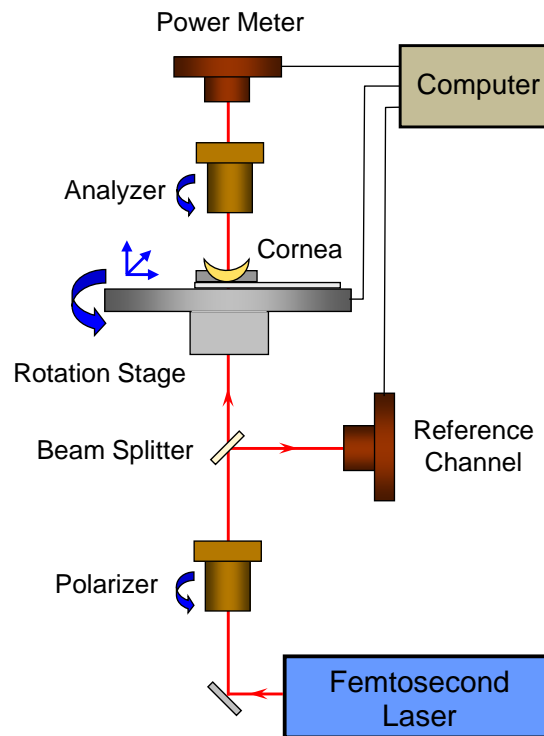
Figure 17. Principle optical experimental setup for assessing phase retardation in corneal tissue. Reprinted with permission from W. Calhoun, R. Weiblinger, A. Beylin, and I. K. Ilev, "Assessing the phase retardation in corneal tissues using a femtosecond laser," Rev Sci Instrum, vol. 84, p. 084301, Aug 2013. Copyright 2013, AIP Publishing LLC.

Experimental protocol

Immediately after the cornea was prepared, control transmission measurements were recorded for dark readings (laser blocked), leakage (transmission with no sample), and polarizer transmission. Transmission coefficients for the analyzer and glass slide were previously determined. The sample was then positioned and sample transmission was measured. Finally, transmission through the analyzer was measured for each position as the cornea was rotated 360 degrees with a 1degree step size. The cornea was then translated 1 mm and the rotation and measurements were repeated until at least 6 spots from the central cornea were sampled. The data was processed and phase rotations were determined offline after all corneas were sampled. At least 6 spots on each of 8 corneas were sampled.

Control measurements were made using only the microscope slide and storage solution to ensure no phase rotation occurred due to these elements.

The accuracy of the system was tested using standard birefringent elements, a quartz, zero-order quarter- and half-wave plates (QWP, HWP) (Edmund Optics). These elements have 90 and 180 degrees of phase rotation, respectively, at 1064 nm and the appropriate orientation.

The precision of the system was tested by performing 4 successive phase rotation measurements at the same corneal location over a 60 min period.

Data analysis

Since the position of the rotational stage has no correlation to the axes of birefringence of the cornea, the data was shifted so that the transmission peaks corresponded to multiples of 45degrees, as that is where maximum phase rotation and therefore transmission would occur. The dark readings and leakage were subtracted from the data. The slide, sample, and analyzer

losses were corrected by dividing the data set by the slide, sample, and analyzer transmission coefficients.

Using matrix multiplication and Jones calculus to model the polarization of light as it passes through each active optical element of the system, the phase rotation at each position of the cornea can be determined. Jones vectors describe the x and y component of the electric field, polarization of the light. Jones matrices are operators describing the effect of an optical element on the incident electric field. Optical birefringence can be described by the following Jones matrix for any birefringent material:

$$\begin{bmatrix} e^{i\varphi_x}\cos^2\theta + e^{i\varphi_y}\sin^2\theta & \left(e^{i\varphi_x} - e^{i\varphi_y}\right)\cos\theta\sin\theta \\ \left(e^{i\varphi_x} - e^{i\varphi_y}\right)\cos\theta\sin\theta & e^{i\varphi_x}\sin^2\theta + e^{i\varphi_y}\cos^2\theta \end{bmatrix}, \tag{1}$$

where, φ_x and φ_y are the x and y components of the phase of the electric field $E(t)$ and θ is the orientation of the fast axis with respect to x-axis[58]. Further, $(\varphi_x - \varphi_y)$ is the phase rotation induced between the electric field components, $E_x(t)$ and $E_y(t)$, by a birefringent material. Specifically, a PBS can be represented by the following reduced form of the previous matrix assuming that a PBS is a linear retarder and introduces no phase rotation:

$$\begin{bmatrix} \cos^2\theta & \cos\theta\sin\theta \\ \cos\theta\sin\theta & \sin^2\theta \end{bmatrix}, \tag{2}$$

which reduces to the following matrices when oriented with its fast axis parallel and perpendicular to the x-axis, respectively:

$$\begin{bmatrix} 1 & 0 \\ 0 & 0 \end{bmatrix}, \begin{bmatrix} 0 & 0 \\ 0 & 1 \end{bmatrix}. \tag{3}$$

Therefore, linearly polarized light exiting a polarizing beam splitter oriented parallel to the x-axis can be represented by the following Jones vector,

$$\begin{bmatrix} 1 \\ 0 \end{bmatrix}, \tag{4}$$

since the electric field is oscillating only in the x-direction. To determine the affect an optical element has on the incident light's electric field, matrix multiplication can be used. The magnitude of the vector is proportional to the intensity of the light. The Jones vector describing the incident light can be multiplied by the element's Jones matrix to determine the polarization of the transmitted light in the following way:

$$\tilde{E}_t = \mathcal{A}\tilde{E}_i ,$$
(5)

where, $\tilde{E}_i$ and $\tilde{E}_t$ are the Jones vectors for the incident and transmitted light, and $\mathcal{A}$ is the Jones matrix describing the optical element.

Since $\tilde{E}_i$ and $\tilde{E}_t$ have been determined experimentally, $\mathcal{A}$, and subsequently the phase rotation, can be solved for in a two-step process. If the Jones vector for the polarized light incident on the cornea (4) and the Jones matrix for a birefringent material (1) are substituted into Equation (5), the transmitted light can be determined:

$$\begin{bmatrix} e^{i\varphi_x}\cos^2\theta + e^{i\varphi_y}\sin^2\theta & \left(e^{i\varphi_x} - e^{i\varphi_y}\right)\cos\theta\sin\theta \\ \left(e^{i\varphi_x} - e^{i\varphi_y}\right)\cos\theta\sin\theta & e^{i\varphi_x}\sin^2\theta + e^{i\varphi_y}\cos^2\theta \end{bmatrix} \bullet \begin{bmatrix} 1 \\ 0 \end{bmatrix} = \begin{bmatrix} e^{i\varphi_x}\cos^2\theta + e^{i\varphi_y}\sin^2\theta \\ \left(e^{i\varphi_x} - e^{i\varphi_y}\right)\cos\theta\sin\theta \end{bmatrix}.$$
(6)

The resulting matrix represents the light transmitted through the cornea and incident on the analyzer. To determine the light transmitted through the analyzer and measured by the photodiode, the same process must be repeated using the Jones matrix for a polarizer rotated 90 degrees and the resulting matrix from Eq. (6) as the incident Jones vector:

$$\begin{bmatrix} 0 & 0 \\ 0 & 1 \end{bmatrix} \bullet \begin{bmatrix} e^{i\varphi_x}\cos^2\theta + e^{i\varphi_y}\sin^2\theta \\ \left(e^{i\varphi_x} - e^{i\varphi_y}\right)\cos\theta\sin\theta \end{bmatrix} = \begin{bmatrix} 0 \\ \left(e^{i\varphi_x} - e^{i\varphi_y}\right)\cos\theta\sin\theta \end{bmatrix}.$$
(7)

The ratio of light passing through the analyzer to the light incident on the cornea is represented by the magnitude of this resulting Jones vector for a specific tissue rotation.

Using the measured transmission ratio and the position of the cornea, the phase rotation $(\varphi_x - \varphi_y)$ due to transmission through the cornea can be determined at each rotational position of the cornea. An average phase rotation was calculated for each spot sampled. Plots showing the vector magnitude and phase rotation for experimental data and theoretical curves were created.

3.3.2 Results

The control, phase rotation measurements of the QWP and HWP confirmed the accuracy of the system. The phase rotation was measured to be 90.0 and 180.5 degrees for the QWP and HWP, respectively. Figures 18(a) and 18(b) show an exceptionally good agreement (within the
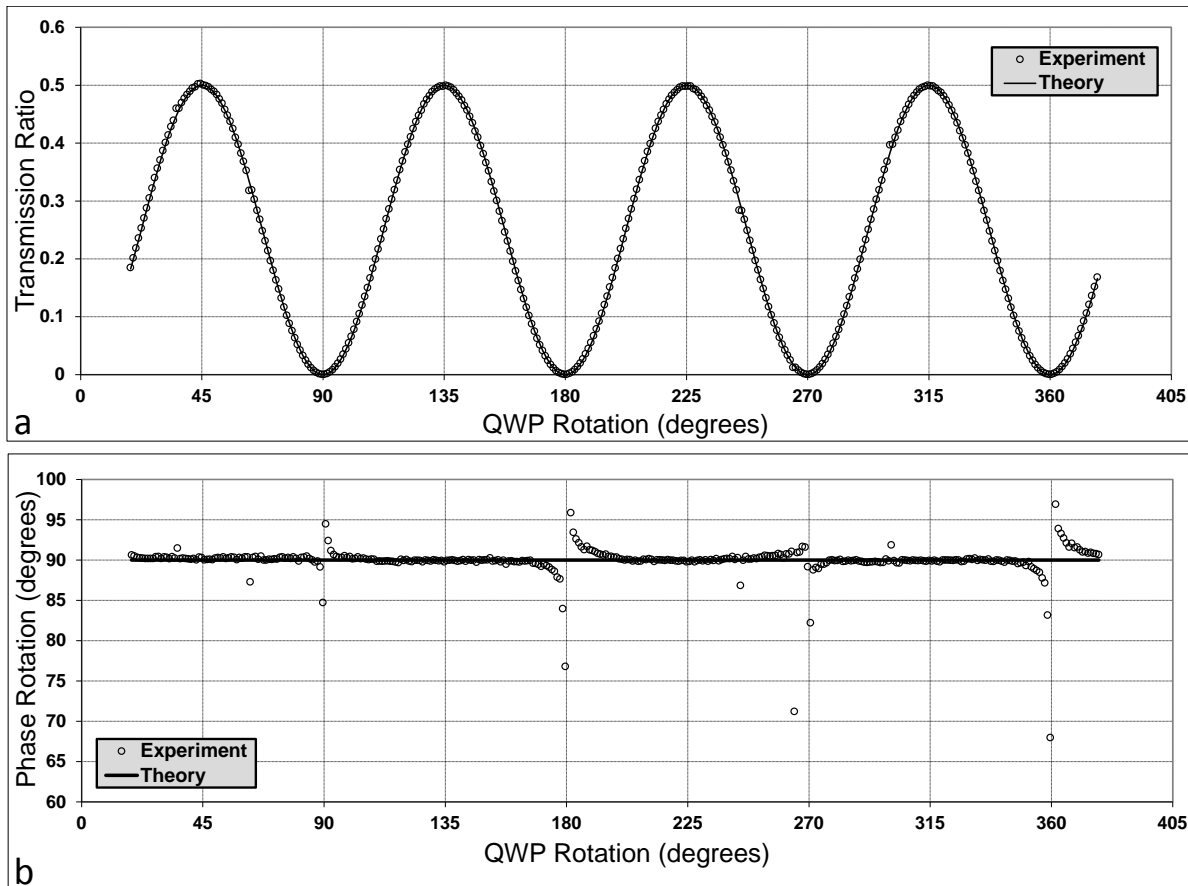
Figure 18. Experimental and theoretical control phase retardation assessment of a quarter-wave plate including: (a) transmission ratio measurements; and (b) phase rotation evaluation. Reprinted with permission from W. Calhoun, R. Weiblinger, A. Beylin, and I. K. Ilev, "Assessing the phase retardation in corneal tissues using a femtosecond laser," Rev Sci Instrum, vol. 84, p. 084301, Aug 2013. Copyright 2013, AIP Publishing LLC.

specified tolerances) between experimental and theoretical data for both the transmission ratio and the phase rotation data for the QWP. Similar results can be seen for the HWP in Figures 19(a) and 19(b). The theoretical dataset is generated using Jones vector analysis assuming a phase rotation of 90.0 and 180.0 degrees for the QWP and HWP, respectively.

Using the bovine corneal tissue samples and the experimental setup described in Chapter 3.3.1, typical transmission ratio plots and corresponding phase rotation plots, illustrated in Figures 20(a) and 20(b) respectively, were obtained. The theoretical dataset was generated for comparison purposes by using the average measured phase rotation value to generate a plot for
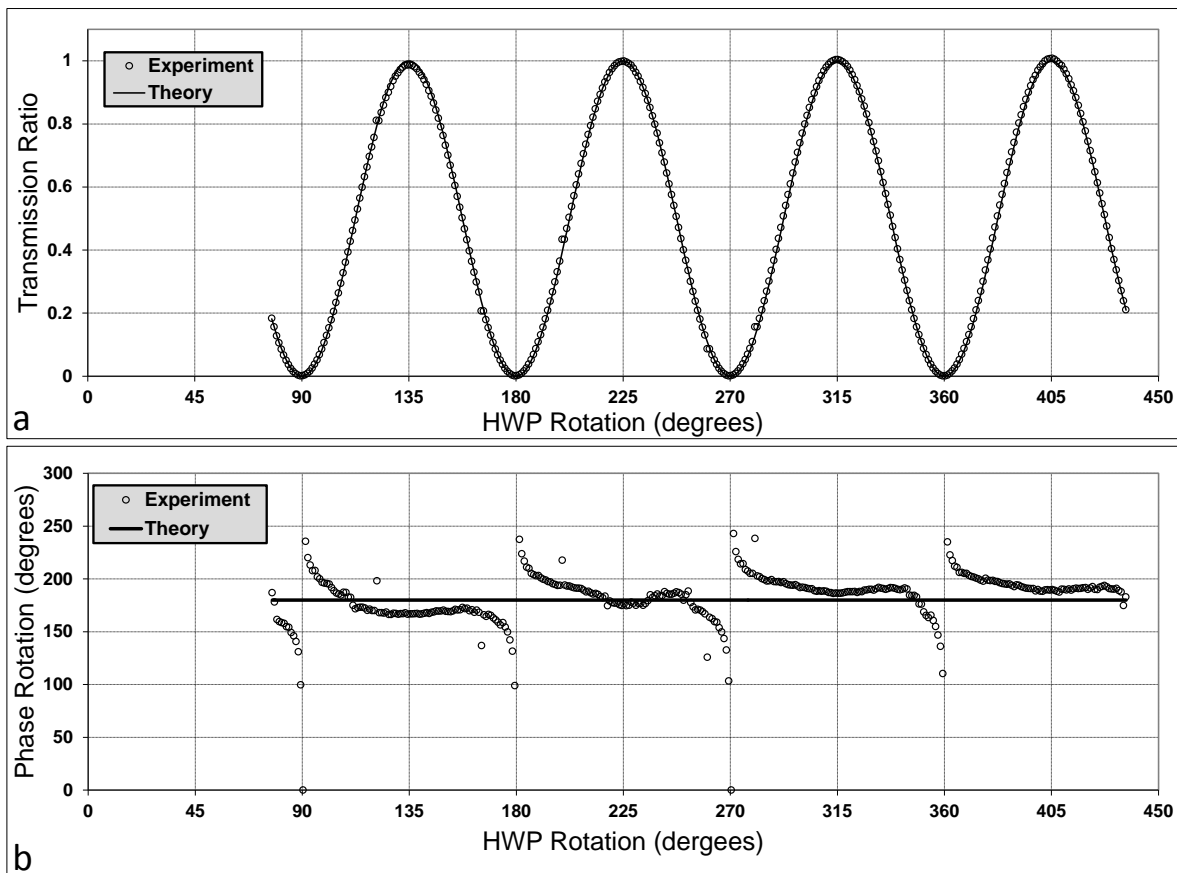
Figure 19. Experimental and theoretical control phase retardation assessment of a half-wave plate including: (a) transmission ratio measurements: and (b) phase rotation evaluation. Reprinted with permission from W. Calhoun, R. Weiblinger, A. Beylin, and I. K. Ilev, "Assessing the phase retardation in corneal tissues using a femtosecond laser," Rev Sci Instrum, vol. 84, p. 084301, Aug 2013. Copyright 2013, AIP Publishing LLC.
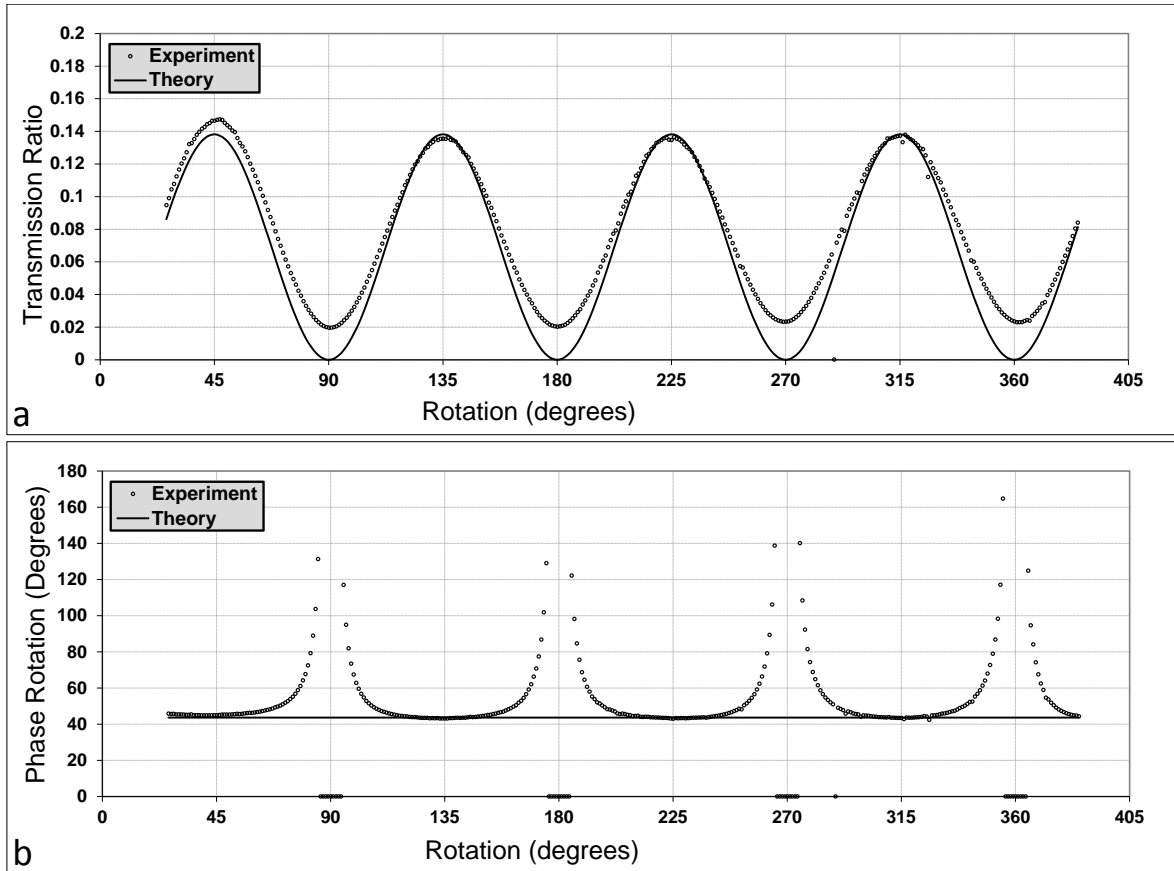
Figure 20. Typical experimental and theoretical phase retardation assessment of a corneal tissue including: (a) transmission ratio measurements; and (b) phase rotation evaluation. Reprinted with permission from W. Calhoun, R. Weiblinger, A. Beylin, and I. K. Ilev, "Assessing the phase retardation in corneal tissues using a femtosecond laser," Rev Sci Instrum, vol. 84, p. 084301, Aug 2013. Copyright 2013, AIP Publishing LLC.

all 360 degrees of rotation.

A summary of the phase rotation measurements performed for 49 locations on 8 cornea samples is presented in Table 3 and Figure 21(a). Phase rotation values ranged from 28.27 degrees to 67.71 degrees. There appeared to be no consistent patterns or trends in phase rotation values associated with central cornea location. The average phase rotation, phase rotation range, and standard deviation for each cornea are summarized in Table 4 and plotted in Figure 21(b). Average corneal phase shift ranged from 40.1 to 58.22 degrees. Intra-corneal phase rotation range was as little as 11.8 and as high as 34.84 degrees, showing large variations even within a

44

Table 3. Phase rotation at each location on each of 8 corneas. Reprinted with permission from W. Calhoun, R. Weiblinger, A. Beylin, and I. K. Ilev, "Assessing the phase retardation in corneal tissues using a femtosecond laser," Rev Sci Instrum, vol. 84, p. 084301, Aug 2013. Copyright 2013, AIP Publishing LLC.

Cornea	Location [mm]						
	1	2	3	4	5	6	7
1	38.5	38.4	45	53.1	44.8	41	42.3
2	42	39.6	34.3	39.5	46.1	39.1	
3	52.5	39.4	37.5	55	49.2	46.8	
4	44.1	46.5	35.6	46.5	61.5	52.9	
5	59.29	41.68	40.3	46.3	55.12	43.65	
6	37.48	47.66	56.41	49.66	51.28	40.96	
7	56.22	53.34	49.97	61.37	60.73	67.71	
8	52.65	28.27	49.17	55.74	63.11	36.97	

single cornea. A variance analysis followed by a Tukey's HSD multiple comparison test was performed using the birefringence values. Significant differences were only found between corneal samples 7 and 2, and 7 and 1, using a confidence level of 95 percent. Finally, Figure 22 illustrates the experimental system's repeatability that was tested by measuring the phase rotation at the same corneal location for 60 min. In this test measurement, the phase rotation increased by 0.7 degrees after 60 min.

3.3.3 Discussion

We have developed a test method to measure corneal phase rotation due to corneal birefringence using dual, crossed polarizing beam splitters, computer controlled sample rotation, and power measurement, and an FSL. The system was validated with two optical standards of birefringence, a quarter-wave plate and a half-wave plate. The system measured their respective phase rotations to be 90.0 degrees and 180.5 degrees. In both cases these measurements were within the
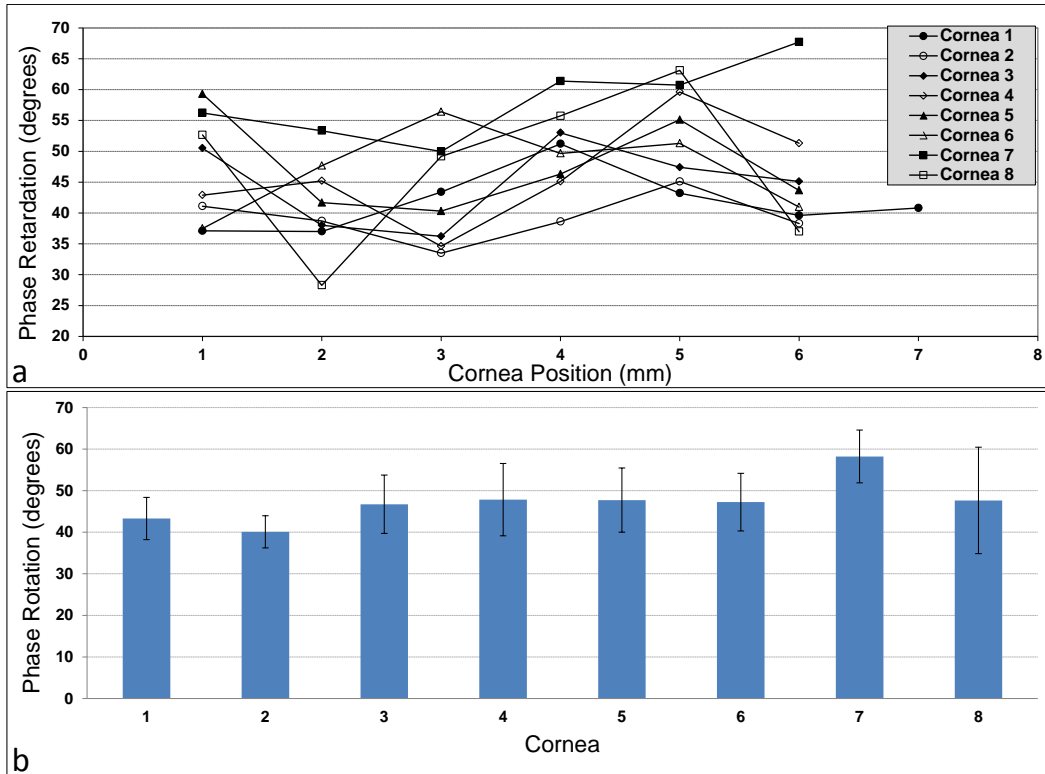
Figure 21. (a) Phase rotation and (b) mean retardation and standard deviation for all locations on all corneas. Reprinted with permission from W. Calhoun, R. Weiblinger, A. Beylin, and I. K. Ilev, "Assessing the phase retardation in corneal tissues using a femtosecond laser," Rev Sci Instrum, vol. 84, p. 084301, Aug 2013. Copyright 2013, AIP Publishing LLC.

specified 1.8 degrees ± tolerance of these optical elements. Further, multiple measurements of

the same location on the quarter- wave plate resulted in identical phase rotations, demonstrating

the repeatability of this technique. Similarly, the results of repeated measurements of the same

location on a corneal sample show the precision and stability of this technique. Some relatively

small jumps in phase rotation can be seen at intervals of $\frac{\pi}{2}$ radians. This is due to extremely

small differences between the experimentally measured transmission ratio and theoretically

expected values from scattering and detector accuracy at very low values. At these rotations, the

expected transmission is extremely low and goes to zero. When calculating the phase rotation at

these locations, very small differences result in large changes in phase rotation. However, at

Table 4. Mean phase rotation, phase rotation range, and phase rotation standard deviation for each cornea. Reprinted with permission from W. Calhoun, R. Weiblinger, A. Beylin, and I. K. Ilev, " Assessing the phase retardation in corneal tissues using a femtosecond laser," Rev Sci Instrum, vol. 84, p. 084301, Aug 2013. Copyright 2013, AIP Publishing LLC.

Cornea	Mean Phase Rotation [degrees]	Phase Rotation Range [degrees]	Standard Deviation [degrees]
1	43.30	14.70	5.07
2	40.10	11.80	3.87
3	46.73	17.50	7.02
4	47.85	25.90	8.71
5	47.72	18.99	7.73
6	47.24	18.93	6.94
7	58.22	17.74	6.36
8	47.65	34.84	12.82

rotations $\frac{\pi}{4}$ radians shifted from minimum transmission there are maxima. At these locations similar differences between experimental and expected transmission values have no significant effect on the calculated phase rotation. For this reason, the region surrounding the maxima is used for determining the phase rotation for any tested sample.

Using the bovine corneal tissue samples, the experimentally measured phase rotations indicate variations between corneal samples and within corneas. These variations were expected as they have been reported in previous studies [92]. Since corneal birefringence is closely related to the stromal collagen [90], normally occurring variations in collagen orientation and density, and non-uniformities that exist from eye to eye, generate variation in corneal birefringence [87, 94]. If indeed, LIB is polarization-dependent in ophthalmic procedures, patient to patient differences would be important to consider, as well as intracorneal differences.

The cornea is modeled as a curved bi-axially birefringent material due to the overall layered, orthogonally oriented, uniaxial lamellae within the stroma of the cornea [92, 94].

47

However, this is not a perfect model since there are many collagen fibrils not parallel to one of the major perpendicular axis. During the experiments, this caused some phase rotation, even when one of the major collagen axis is oriented parallel to the laser polarization. This results in non-zero values for the transmission ratio, different from a theoretical, ideal model of biaxial birefringence at corneal rotations of multiples of 90 degrees (Figure 19(a)). Further, similar to the reference waveplates, this results in undefined phase rotation values at these corresponding positions (Figure 19(b)). Additionally, scattering and other depolarizing events may contribute to the non-zero values. However, based on pre-experimental measurements of the corneal samples, typical transmission values are greater than 92 percent at the 1064 nm. This indicates that scattering and absorption are relatively low. Furthermore, the mammalian cornea has been shown to have a negligible depolarization effect [96], which also indicates that scattering is not significant. As previously described, these non-zero values do not affect the calculated phase rotation since values are averaged from regions $\frac{\pi}{4}$ radians between axes.

Another area where the experimental data depart from the theoretical plots can be seen when comparing the peak to peak consistency in the transmission ratios. As previously discussed these inconsistencies are typically insignificant. In order to investigate if there were any inconsistencies in the corneal surface, optical coherence tomography (OCT) was used to map the front and back surfaces of the cornea with the cornea in the cradle used during the phase rotation experiments. The images showed that the corneal thickness varied in some cases since the curvature of the cradle did not match exactly the natural curvature of the cornea and because the central portion of the cornea was intentionally flattened to ensure normal laser incidence. It is likely that despite the rotational stage being centered on the laser axis to eliminate any sample wobbling, there may have been very minor wobbling present in some cases. This would cause
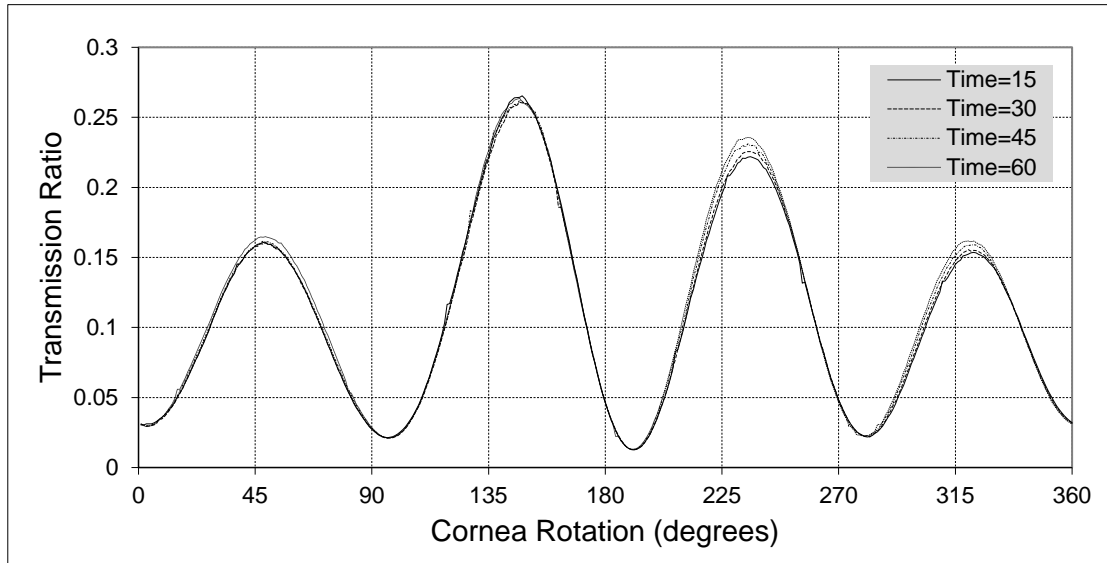
Figure 22. Repeatability of phase rotation measurement system. Reprinted with permission from W. Calhoun, R. Weiblinger, A. Beylin, and I. K. Ilev, "Assessing the phase retardation in corneal tissues using a femtosecond laser," Rev Sci Instrum, vol. 84, p. 084301, Aug 2013. Copyright 2013, AIP Publishing LLC.

the laser to sample different corneal thicknesses as the sample rotated, resulting in slightly different peak intensities within one sample location.

The corneal phase retardation values found in this study are lower than recently reported values by Bueno and Jaronski [97]. Several factors may be responsible for these differences. The birefringence is likely affected by chromatic dispersion, as infrared light (1064 nm) was used in these experiments, while visible light (633 nm) was used in the referenced study. In addition, there may be contributions from the cornea's nonlinear refractive index due to the significantly higher intensities generated by the FSL used in this study. Finally, there may also be differences in birefringence between the corneal tissues used in each study as there are many different types of animals under the bovine sub-family name.

Furthermore, in comparison to some alternative techniques employed to study and map the birefringence of the cornea such as polarization-sensitive optical coherence tomography

(psOCT) [98] and scanning laser polarimetry (SLP) [94, 97], the proposed FSL based test method has essential advantages. Unlike the low-power continuous-wave (CW) laser sources used in these techniques, FSLs generate intensities orders of magnitude higher than these lasers. These high intensities are capable of changing the optical properties of the tissue, including birefringence [99]. Therefore, it is important to measure the birefringence using a clinically relevant FSL. Additionally, the intention is not to map or image the corneal birefringence, but rather to sample the central cornea to generate a reference point for the laser parameters associated with this FSL.

Conclusion

An accurate, precise, and highly repeatable test method for quantification of phase retardation in corneal tissues using an FSL was demonstrated. Employing the experimental system and analytical model, the method's high accuracy and repeatability potential was validated by testing control phase retardation samples. The phase retardation of an FSL through bovine corneal samples was measured and found that there is a considerable, location dependent, variation in retardation values.

The experimental and theoretical results obtained can be utilized in studying and optimizing basic FSL parameters to make their application in ophthalmic procedures safer and more effective. Considering that many nonlinear optical processes are polarization dependent [100], understanding the effect the cornea has on FSL polarization is important for attempts to control unwanted and desired effects of therapeutic procedures that use FSLs. In addition, attempts to measure the birefringence of other ocular structures, such as the retinal nerve fiber layer or the aqueous media, need to compensate for corneal effects.

Moreover, the advanced features of the test method developed can be employed for further investigation of the dependence of birefringence effects in various ocular tissues on the FSL pulse energy using a single FS laser to simulate either low-energy (pre-therapeutic) or high-energy (therapeutic) quasi continuous-wave laser emission. These studies can further contribute toward the evaluation of safety and efficacy of novel FSL therapeutic technologies and devices.

3.4 Nonlinear optical effects

Nonlinear optical effects are phenomena that occur due to a modification of a material's optical properties by an intense optical field, usually provided by a laser. They are nonlinear because the intensity of the effect depends in a nonlinear way on the intensity of the optical field. For example, the intensity of second- and third-order nonlinear effects will increase with the square and cube of the applied optical field. Under ordinary conditions, most optical effects can be considered linear and their intensity can be related to the strength of an applied optical field, $\tilde{E}(t)$, through the Equation for the polarization, $\tilde{P}(t)$, of a material system:

$$\tilde{\boldsymbol{P}}(t) = \epsilon_0 \boldsymbol{\chi}^{(1)} \tilde{\boldsymbol{E}}(t) , \tag{8}$$

where, ϵ_0 is the permittivity of free space and $\chi^{(1)}$ is the linear susceptibility of the material. For many applications this equation describes the material polarization very well due to low material nonlinear susceptibilities and/or low optical field intensities.

Equation (8) can be expanded to account for nonlinear optical effects:

$$\tilde{\boldsymbol{P}}(t) = \epsilon_0 \boldsymbol{\chi}^{(1)} \tilde{\boldsymbol{E}}(t) + \epsilon_0 \boldsymbol{\chi}^{(2)} \tilde{\boldsymbol{E}}^2(t) + \epsilon_0 \boldsymbol{\chi}^{(3)} \tilde{\boldsymbol{E}}^3(t) \dots , \tag{9}$$

where, $\chi^{(2)}$ and $\chi^{(3)}$ are the second- and third-order nonlinear susceptibilities, respectively. Both $\tilde{P}(t)$ and $\tilde{E}(t)$ are time varying vectors, and $\boldsymbol{\chi}^{(1)}$, $\boldsymbol{\chi}^{(2)}$ and $\boldsymbol{\chi}^{(3)}$ are second-, third- and fourth-

order tensors, respectively, that relate the amplitudes of the electric field to the material polarization. Equation 9 can also be expressed as the sum of individual polarization contributions,

$$\widetilde{\boldsymbol{P}}(t) = \widetilde{\boldsymbol{P}}^{(1)}(t) + \widetilde{\boldsymbol{P}}^{(2)}(t) + \widetilde{\boldsymbol{P}}^{(3)}(t) \dots \tag{10}$$

with $\widetilde{\boldsymbol{P}}^{(1)}(t)$, $\widetilde{\boldsymbol{P}}^{(2)}(t)$, and $\widetilde{\boldsymbol{P}}^{(3)}(t)$ being the linear, second- and third-order polarizations, respectively. Without specific actions to optimize NOEs their efficiency can be low. Additionally, as Equation (9) indicates, the strength of a particular nonlinear effect increases with the square or cube of the electric field strength, in the case of second order and third order NOEs respectively. For these reasons, optical fields generated by conventional CW lasers often produce very weak NOEs. However, ultrashort pulsed lasers, such as therapeutic FSLs, generate optical fields approaching the atomic field strength (E_{at}) of 5.14×10^{11} V/m, overcoming low efficiencies to produce observable NOEs.

Polarization in terms of a time varying electric field is often used to describe NOEs because, according to Larmor's theorem, accelerated charges generate electromagnetic radiation [101]. This can be seen in the wave-equation, derived from Maxwell's equations, that takes into account propagation through nonlinear media:

$$\nabla^2 \widetilde{\boldsymbol{E}} - \frac{1}{c_0^2} \frac{\partial^2 \widetilde{\boldsymbol{E}}}{\partial t^2} = \frac{1}{\mu_0} \frac{\partial^2 (\widetilde{\boldsymbol{P}}^L + \widetilde{\boldsymbol{P}}^{NL})}{\partial t^2}, \tag{11}$$

where, c_0 is the vacuum speed of light, μ_0 is the permeability of free space, and $\widetilde{\boldsymbol{P}}^{NL}$ and $\widetilde{\boldsymbol{P}}^L$ are the induced nonlinear and linear polarizations respectively. The partial derivative of the nonlinear polarization with respect to time term is a measure of acceleration of charges and supports the principle that the nonlinear polarization can generate light , including light having different wavelengths [101].

Although there are many nonlinear optical effects, the scope of this dissertation focuses primarily on harmonic generation, however the inherently nonlinear process of optical breakdown and effects of an intensity dependent refractive index as they relate to FSL based ocular surgery will be discussed.

3.4.1 Laser induced breakdown

The laser tissue cutting effect induced by USP lasers is known as photodisruption. It occurs when laser energy is rapidly deposited into a small volume, creating a high field intensity that generates free electrons. As the free electron concentration grows plasma is formed. In tissues, or other aqueous environments, the plasma vaporizes surrounding water and tissue and rapidly expands. This action generates a gas bubble followed by cavitation. This process is known as laser induced breakdown (LIB). Photodisruption is unique compared with ablation by longer pulse durations and different laser wavelengths. Most ablation mechanisms rely on linear absorption of laser photons which generates thermoelastic destruction and photochemical degradation of tissue. In LIB, nonlinear absorption of photons leading to plasma mediated ablation occurs without thermal destruction.

The NOE that initiates LIB and is responsible for the success of FSL based ocular surgery is nonlinear absorption. Nonlinear absorption occurs when multiple photons are absorbed by a molecule and elevate a single electron to a higher energy level. In order for this to occur, two or more photons must arrive at the molecule at the same location and time. Until the development of USP lasers, high enough fluences weren't obtainable and this requirement could not be provided. Compared with linear absorption, multiphoton absorption (MPA) varies with the square of the electric field intensity, in the case of two photon absorption, as opposed to linearly. By comparing traditional fluorescence microscopy with a technique that utilizes MPA,

53

two-photon excitation microscopy (TPEM), the precision that nonlinear absorption provides can be illustrated as shown in Figure 23. In fluorescence microscopy, emission is generated by linear absorption throughout the laser field within the sample. In TPEM, emission only occurs at the beam waist where the electric field intensity is sufficiently high enough to generate MPA. Similarly, during LIB, the infrared photons travel through ocular tissues experiencing very low absorption until a high enough intensity is achieved at the beam waist where MPA occurs. Consequently, LIB can produce extremely localized tissue destruction inside tissues, organs and even cells with significantly reduced collateral damage compared with ablation based on linear absorption.
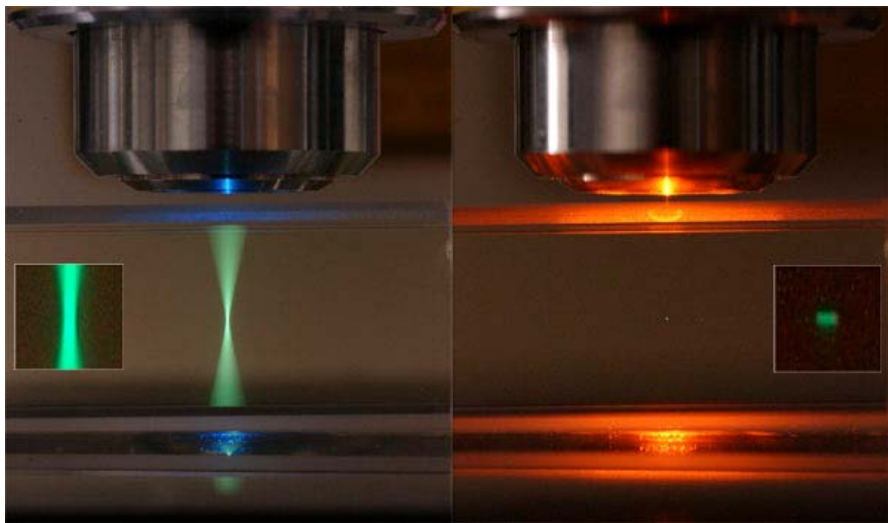
Figure 23. Comparison of (left) linear optical absorption and (right) nonlinear 2-photon absorption principles . Reprinted with permission from Ms. Holly Aaron and Dr. Steve Ruzin.

LIB is a process that involves MPA and avalanche ionization when induced by FSL pulses. Ocular tissues have similar optical LIB thresholds as water [102], and therefore have an excitation energy of ΔE=6.5 eV [103]. This requires that six photons be simultaneously absorbed to elevate an electron into the conduction band, assuming the laser wavelength is near 1040nm, where most clinical FSLs typically operate. MPA generates free electrons that act as seed free

electrons in the avalanche ionization process (Figure 24). Once an electron is excited into the conduction band, it can absorb energy from additional photons in a process called inverse Bremsstrahlung absorption (IBA). After 6 IBA events, the electron will have enough kinetic energy to exceed the band gap energy once again. At this point it can collide with and free another bound electron. This process repeats and exponentially generates free electrons. If the laser irradiance is high enough, the concentration of free electrons will grow and overcome losses from diffusion away from the focal region and recombination. MPA occurs on a time scale of a few femtoseconds while IBA occurs in about one femtosecond [104].

As the free electron concentration increases, plasma is formed upon reaching a critical free electron density approximately $\rho_{cr} \approx 10^{21}$ cm^{-3} for femtosecond pulses [105]. The plasma is generated before the beam waist and grows towards waist as the irradiance increases until the intensity peak of the pulse. The plasma shields the tissue after the focus during plasma growth. Energy absorbed after the pulse peak heats the plasma but doesn't elongate it [106-108]. This
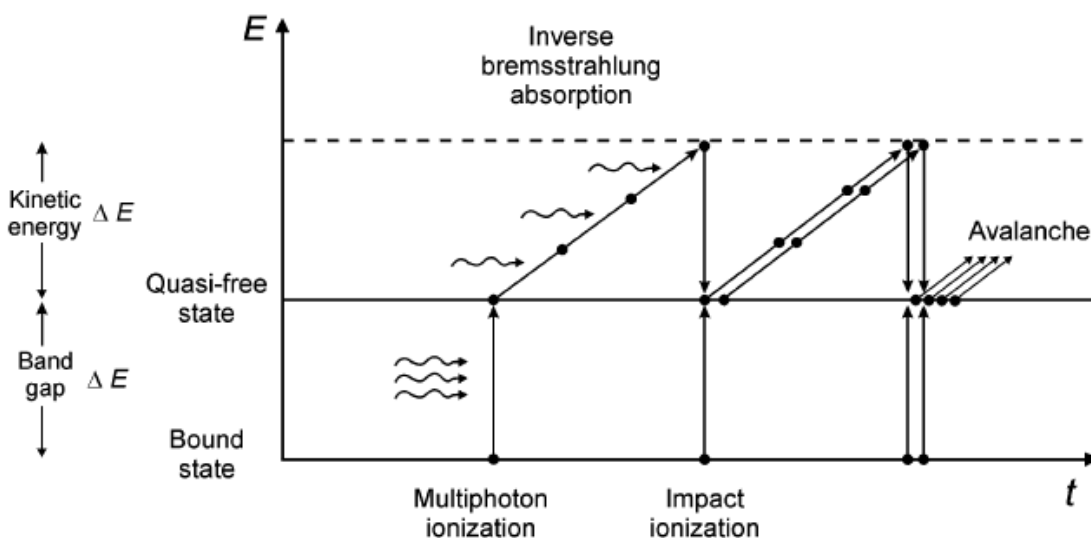
Figure 24. Description of avalanche ionization. Reprinted with permission from A. Vogel and V. Venugopalan, "Mechanisms of pulsed laser ablation of biological tissues," Chem Rev, vol. 103, pp. 577-644, Feb 2003. Copyright 2003, American Chemical Society.

heat is then transferred to the surrounding medium. With FSLs, the laser pulse is shorter than the electron cooling and recombination times and therefore very little energy is transferred to the surrounding medium. For FSL pulses with a Gaussian intensity profile, the length of the plasma from the beam waist towards the incoming laser, Z_{max}, can be predicted by the following Equation:

$$Z_{max} = Z_R\sqrt{\beta - 1} \,, \tag{12}$$

where, Z_R is the Rayleigh range and β is the ratio between the achieved peak irradiance and the threshold irradiance for LIB[107].

Plasma formation in tissue generates a shock wave and bubble formation, followed by cavitation. Since the plasma is superheated, it explosively expands causing tissue disruption beyond the plasma volume of tissue vaporization [103]. The exception to this is during ablation on the surface of tissues when the plasma isn't mechanically confined. In this case, the tissue disruption is close to the laser focal spot size [109]. As the bubble expands, rapid adiabatic cooling occurs, limiting thermal diffusion to fractions of a micrometer. Within the plasma, in addition to thermal degradation, chemical decomposition of molecules by free electrons occurs, including reactive oxygen species formation [110].

3.4.2 Second-harmonic generation

Second-harmonic generation (SHG) is a second-order NOE and a specific case of the larger family of NOEs known as frequency mixing processes. It was first demonstrated in 1961 by Franken et al., who focused a 694.3-nm wavelength, 3-J pulse energy, ms-pulse duration, Ruby laser into a quartz crystal (Figure 25(a)) generating some light with twice the frequency (347.2 nm) [111]. In quantum theory, SHG occurs when two photons at the fundamental laser frequency
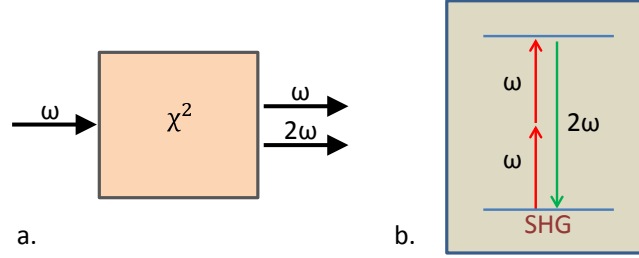
Figure 25. Description of second-harmonic generation in (a) wave and (b) quantum theory.

(ω) coalesce to produce a single photon having twice the frequency of the fundamental (2ω) (Figure 25(b)) according to the conservation of energy and the Planck-Einstein relation:

$$E = h\upsilon, \tag{13}$$

where, E is the photon energy, h is Planck's constant and υ is the photon frequency, or the inverse wavelength. The source of the doubled frequency can be found by considering the equation for the induced second order polarization as introduced in Equations (9) and (10):

$$\widetilde{\boldsymbol{P}}^{(2)}(t) = \epsilon_0 \boldsymbol{\chi}^{(2)} \widetilde{\boldsymbol{E}}^2(t). \tag{14}$$

If a simple oscillator is assumed for the input optical field,

$$\widetilde{\boldsymbol{E}}(t) = E_0 \sin \omega t, \tag{15}$$

then Equation (14) becomes,

$$\widetilde{\boldsymbol{P}}^{(2)}(t) = \epsilon_0 \boldsymbol{\chi}^{(2)} (E_0 \sin \omega t)^2 = \frac{\epsilon_0 \boldsymbol{\chi}^{(2)}}{2} E_0^2 (1 - \cos 2\omega t). \tag{16}$$

Further expanded, Equation (16) becomes

$$\widetilde{\boldsymbol{P}}^{(2)}(t) = \frac{\epsilon_0 \boldsymbol{\chi}^{(2)}}{2} E_0^2 - \frac{\epsilon_0 \boldsymbol{\chi}^{(2)}}{2} E_0^2 \cos 2\omega t. \tag{17}$$

The first term of the expanded second-order polarization indicates that a constant polarization of the medium is generated. This is known as optical rectification. The second term is a time dependent oscillation at frequency 2ω, the source of the second harmonic wave [58, 82]. All of these components, including the input optical field are plotted in Figure 26.

57
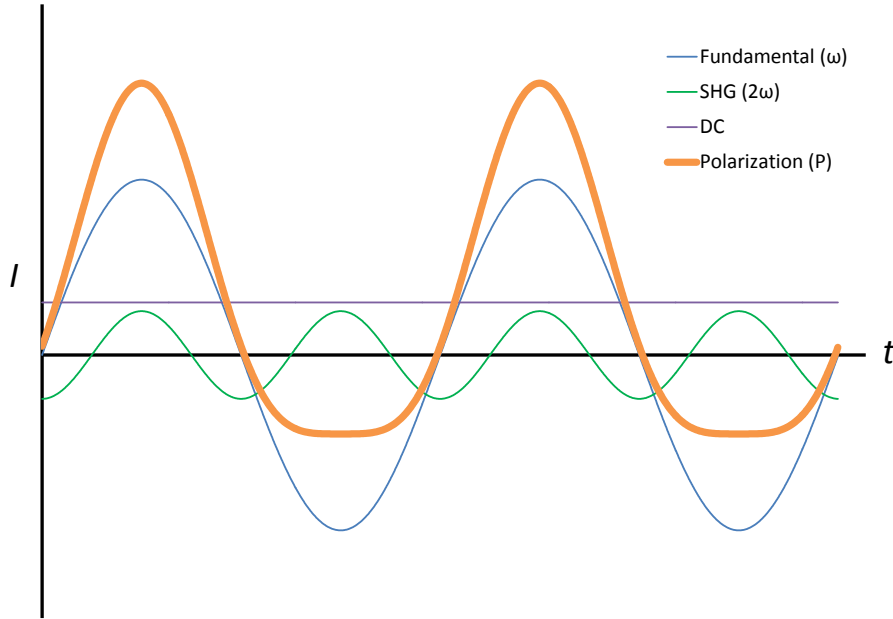
Figure 26. Example of component oscillation intensity (I) of the second-order nonlinear material polarization.

SHG will only occur in materials that have no center of symmetry, known as noncentrosymmetric materials. This corresponds with the mathematical description of the second-order nonlinear polarization (Figure 26) which shows an asymmetric oscillation. In amorphous or centrosymmetric materials, the motion of an electron in an optical field is symmetric and therefore, second-order NOEs cannot occur. In the case of SHG, a component oscillation at twice the fundamental frequency cannot occur in centrosymmetric materials; otherwise the polarization would be asymmetric. This can also be shown using Equations 14 and 15. If the sign of the electric field is changed, so must that of the polarization since the material is assumed to be centrosymmetric. Therefore,

$$-\widetilde{\boldsymbol{P}}^{(2)}(t) = \epsilon_0 \boldsymbol{\chi}^{(2)}\left[-\widetilde{\boldsymbol{E}}(t)\right]^2, \tag{18}$$

which becomes,

$$-\widetilde{\boldsymbol{P}}^{(2)}(t) = \epsilon_0 \boldsymbol{\chi}^{(2)} \widetilde{\boldsymbol{E}}^2(t). \tag{19}$$

Combined with Equation (14), it can be seen that

$$-\widetilde{\boldsymbol{P}}^{(2)}(t) = \widetilde{\boldsymbol{P}}^{(2)}(t), \tag{20}$$

which can only be true if $\chi^{(2)} = 0$ in centrosymmetric media.

SHG efficiency depends largely upon the phase relationship between the second harmonic oscillation and the fundamental frequency. This relationship can be described using the wave number, k, the magnitude of the wave vector (**k**),

$$k = \frac{2\pi}{\lambda} = \frac{n\omega}{c}, \tag{21}$$

where, λ is the wavelength and c is the vacuum speed of light. For ideal SHG,

$$k_\omega - 2k_{2\omega} = \Delta k = 0, \tag{22}$$

where, k_ω and $k_{2\omega}$ are the wave numbers for the fundamental and second harmonic waves, respectively, and Δk is known as the phase mismatch. When $\Delta k = 0$, optimal SHG will occur. This condition is known as being phase matched. In most materials however, due to the material dispersion, Δk is usually not zero and there is a phase mismatch (Figure 27(a)). The magnitude of the phase mismatch will determine, largely, the amplitude of the second harmonic field. With phase mismatch, energy will flow back and forth between the second-harmonic and fundamental fields, oscillating with propagation distance, and not constructively building (Figure 28). A
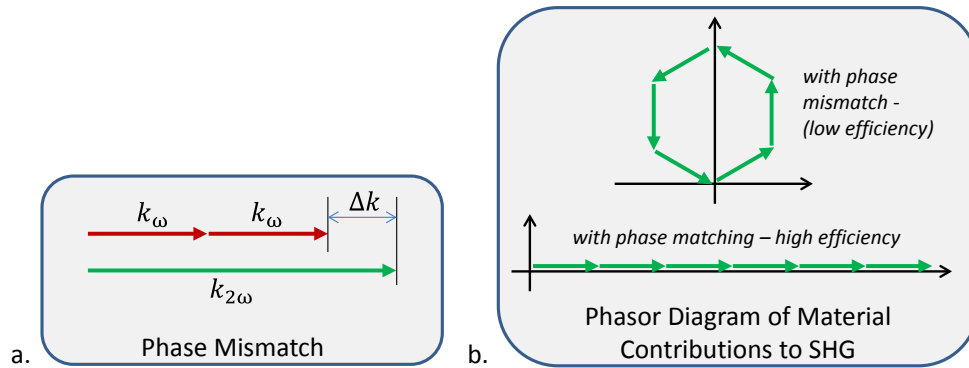
Figure 27. (a) Phase mismatch and (b) associated phasor diagram of material contributions related to second-harmonic generation.

59

method for reducing the phase mismatch, and therefore, increasing the SHG field amplitude, is by exploiting birefringence, a common property of many materials with significant second-order nonlinear susceptibilities.

Birefringence can be used to compensate for dispersion by reducing the difference in the refractive index of the respective waves. For example, a collimated laser beam with vertical polarization passes through a positive uniaxial crystal along the optical axis (z-axis) and produces a second harmonic field with horizontal polarization (Figure 29). The refractive indices along the x and y axes (n_1, n_2), in the x-y plane, are equal, and the refractive index in the z-direction (n_3) is higher. By rotating the crystal about the x-axis, the refractive index experienced by the vertical, fundamental electric field can be adjusted, while that of the horizontal harmonic field remains unchanged. At a critical angle, the 2 fields will be in-phase and the resulting SHG field will grow exponentially with propagation (Figure 27(b) and Figure 28).
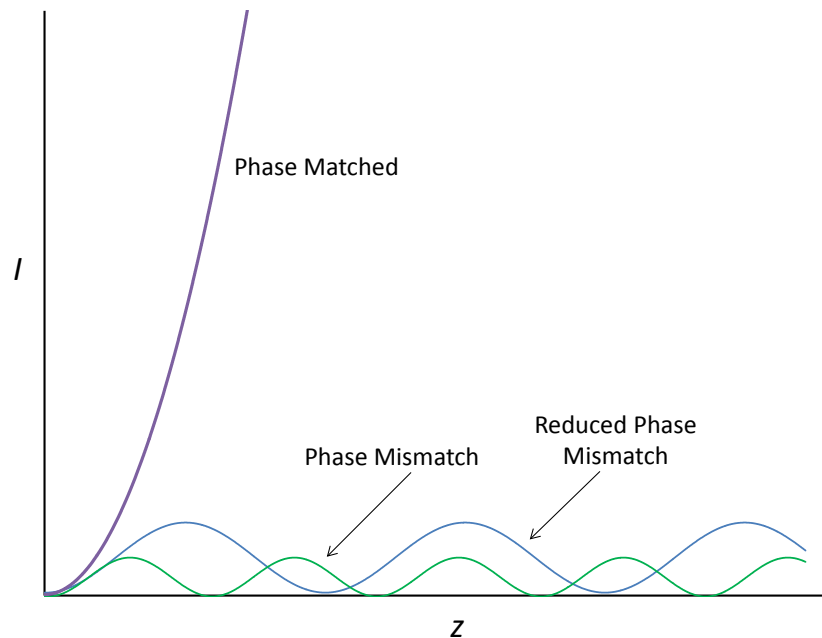
Figure 28. Growth of the second-harmonic generation intensity (I) with propagation distance (Z) with vary degrees of phase matching.
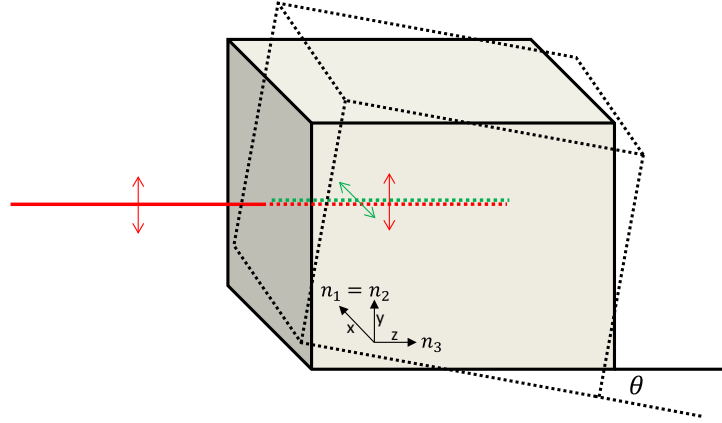
Figure 29. Example of birefringent phase matching using a birefringent crystal.

3.4.3 Third-harmonic generation

Similar to SHG, THG is another type of frequency mixing process; however, it is a third-order nonlinear event. Unlike second-order processes, third-order NOEs can occur in centrosymmetric materials as wells as amorphous materials which have a random organization that leads to a symmetric material polarization. The intensity of third order NOEs varies with the cube of the electric field intensity as shown in Equation (9). The resulting material polarization in a centrosymmetric material can be formed by substituting Equation (15), an arbitrary optical wave, into the formula for the 3rd order nonlinear polarization, $\widetilde{\boldsymbol{P}}^{(3)}(t)$:

$$\widetilde{\boldsymbol{P}}^{(3)}(t) = \epsilon_0 \boldsymbol{\chi}^{(3)}(E_0 \sin \omega t)^3 = \frac{\epsilon_0 \boldsymbol{\chi}^{(2)}}{4} E_0^3 (3\sin \omega t - \sin 3\omega t), \tag{23}$$

The resulting second term shows a time varying component with frequency 3ω. The resulting material polarization in a centrosymmetric material can be seen in Figure 30. In terms of quantum theory, 3 incident photons at the fundamental frequency (ω) coalesce to form a single photon having three times the frequency of the fundamental (3ω) (Figure 31(a) and 31(b)).

61
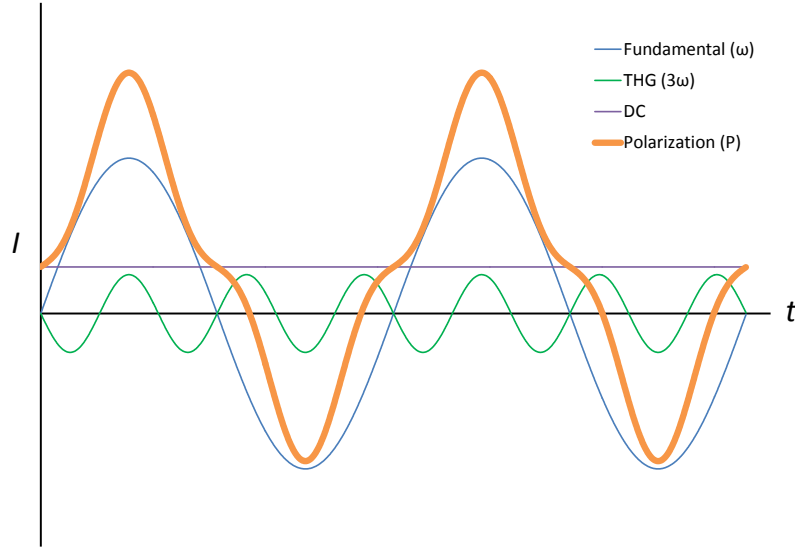
Figure 30. Example of component oscillation intensity (I) of the third-order nonlinear material polarization.

Phase matching is also important for improving the efficiency of THG. However, greater compensation is necessary as there is a larger separation between the fundamental and third harmonic frequencies as seen in the ideal wave vector Equation:

$$k_\omega - 3k_{3\omega} = \Delta k = 0. \tag{24}$$

3.4.4 Intensity-dependent refractive index

In general, the refractive index of a material is considered to be a constant optical property, only respective of frequency. However, when the optical field strength reaches significantly higher values, the refractive index can be expressed in the following Equation:

$$n = n_0 + n_2 I, \tag{25}$$

where, n_0 is the linear refractive index and n_2 is the nonlinear refractive index, a function of the optical field intensity, I, which is defined as:

$$I = 2n_0\epsilon_0 c|E(\omega)|^2 . \tag{26}$$
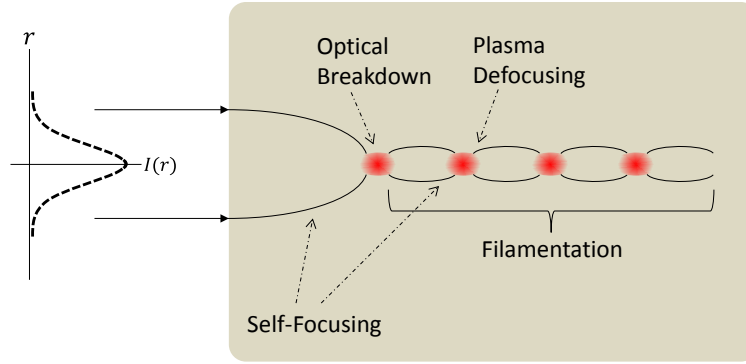
Figure 31. Self-focusing and filamentation effects of the intensity dependent refractive index, induced by Gaussian femtosecond laser beam profile.

For this reason n_2 is also known as the intensity dependent refractive index and responsible for the optical Kerr effect.

Several phenomena occur as a result of the Kerr effect, one of which is called self-focusing. Self-focusing occurs when the intensity profile of a light propagating through a material in not uniform and induces a similar refractive index profile in the medium. In the case of a Gaussian beam intensity profile (Figure 32), which has an intensity profile that peaks at the beam axis and decreases with radial position, a similar index will be induced in a material. The material will then behave as a positive lens, focusing the beam onto itself. Self-focusing may also lead to filamentation propagation. Filamentation propagation is the repetitive process of self-focusing leading to LIB and plasma formation, which then defocuses the beam until self-
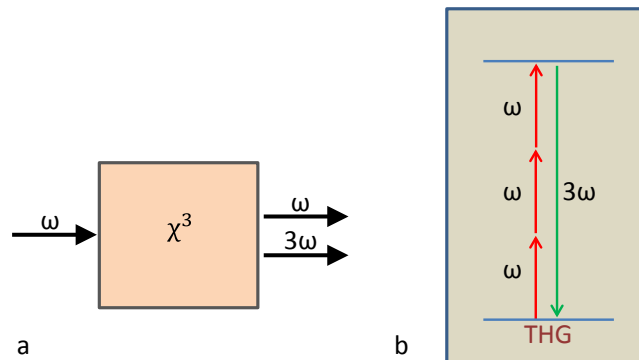
Figure 32. Description of third-harmonic generation in (a) wave and (b) quantum theory.

63

focusing is dominant once again. The result of this recurring focus of the beam is a sequence of material destruction. This effect was observed during fabrication of retinal optical phantoms using FSL pulse focused into silicone substrates by Baxi, Calhoun et al. [112]. Not only was the achieved focal depth dependent on pulse energy, but filamentation was generated (Figure 33).
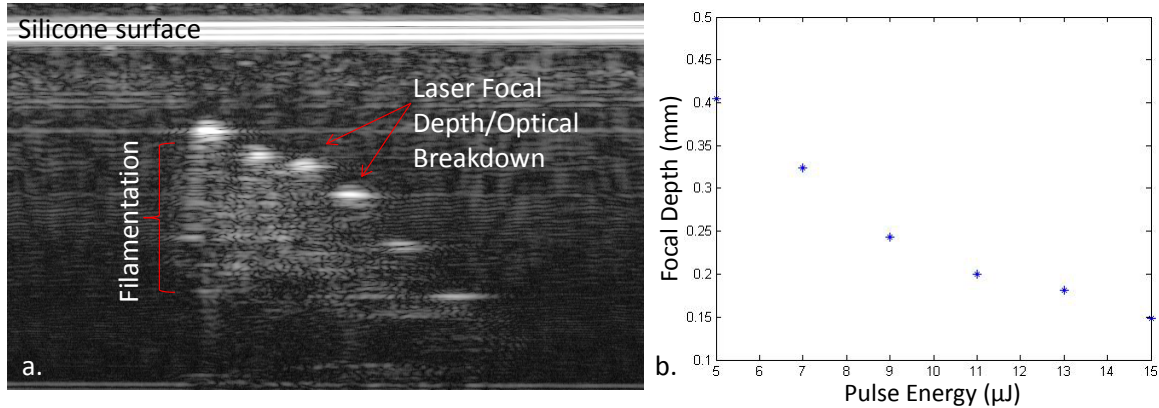
Figure 33. (a) Optical coherence tomography image of femtosecond laser induce self-focusing and filamentation in silicone retinal phantoms; and (b) measured ablation depth with respect to pulse energy.

3.5 Safety concerns

An important application of this work relates to the safety of FSL based surgical devices used in ophthalmic procedures. As the use of therapeutic FSLs in ophthalmology is young, the understanding of the safety issue is also not well formed. To date, most safety studies related to FSL use have focused on immediate damage of retina and corneal endothelium. Since the therapeutic laser is focused on ocular structures in the anterior segment of the eye, the irradiance on the retina (posterior segment) is orders of magnitude lower and not capable of generating LIB. For this reason most retinal safety analysis has evaluated photothermal and photochemical injury potential. Lund, Stuck and Edsall showed that retinal damage generated by laser exposures in the

64

blue visible wavelengths using pulse durations from 0.1 s to 100 s is primarily from thermal injury, not photochemical [113]. In 2002, Cain et al. established MPEs regarding thermal injury to retinal tissue using FSL pulses with 130 fs duration, 1 kHz repetition rate and 800nm wavelength [114]. More recently, Wang et al. determined thermal damage thresholds for various cataract surgical scanning patterns for different retinal perfusion states [115].

Endothelial cell damage is also of interest since it is critical to the performance of the cornea and can greatly affect the visual outcome of the procedure. Most of these studies have examined endothelial cell count and morphology following FSL based procedures and compared them with the manual versions which they have replaced. Results indicate that FSL assisted therapies have reduced endothelial cell loss [48].

With respect to NOEs, Heisterkamp et al. demonstrated THG in corneal tissue using therapeutic FSL parameters, but did not examine how laser parameters influence this event or if it poses a safety concern[116]. Another group recognized that SHG and frequency conversion, as well as other nonlinear effects, need to be considered when using FSLs for corneal procedures[117]. Several reviews addressing retinal damage mechanisms are available [67, 118, 119]. Although there is some discussion of NOEs such as LIB, self-focusing and filamentation, none of them examine HG as a potential safety concern.

Under normal circumstances, UV wavelengths are not considered a threat to retinal safety because the cornea and lens absorb almost all radiation in this range. In the case of THG produced at the corneal endothelium, THG will produce UV light that will experience significantly less attenuation as it propagates to the crystalline lens.. The most current laser safety standards do not appropriately address HG in corneal tissue, including THG in corneal tissue. Despite the previously discussed studies, no published works have directly addressed the

occurrence of harmonic generation in corneal tissue from a safety perspective. A detailed safety

discussion is presented in Chapter 6.

Chapter 4 – Tissue Specific Effects on Harmonic Generation

4.1 Introduction

The nonlinear material susceptibility is a constant of proportionality that relates the amplitude of the nonlinear polarization to the incident optical field amplitude. It depends greatly on the structure of the material through which the optical wave is travelling as was discussed in Chapter 3. Since the FSL is focused to produce precise photodisruption, a high intensity field is generated for only a small tissue volume along the optical axis. Therefore, as the laser focus moves to different locations the high intensity field will interact with a varying environment and one can expect various degrees of HG. Changes in HG efficiency can be due to several specific properties that affect the HG process. Not only is the cornea composed of several layers, each having unique optical properties, but there is also variation in the optical properties within each layer. Further, corneal optical properties vary from eye to eye. In this Chapter changes in HG due to tissue contributions will be investigated.

Harmonic microscopy (HM), a type of nonlinear microscopy (NLM), has been used extensively to image collagenous tissues including human [24, 120, 121], bovine [122] and porcine [123-125] corneal tissue for its ability to form high contrast images without the need for exogenous contrast mechanisms or high optical fluence that can be cause photo bleaching and tissue damage. Many of the studies involving corneal tissue are focused on determining collagen and lamellar orientation as well as changes in structure associated with pathologic states. Jay et

al induced HG in porcine cornea tissue using an FSL (1060nm) and collected the THG and SHG signals [23]. They found that peaks in THG corresponded with interfaces between the surrounding medium and the corneal tissue, and to a lesser extent, with interfaces between corneal layers. SHG was limited to the corneal stroma. Several other groups had similar findings [120-122, 126]. Other sources of THG in corneal tissue are heterogeneities such as cell walls, nuclei and lamellar interfaces, while the SH signal is generated within the collagen molecule.

4.2 Tissue layer effects on second- and third-harmonic generation

There is a significant difference between FSLs used for NLM and therapeutic FSLs used for generating LIB in ophthalmic procedures. In microscopy, FSL pulse energies on the order of several nanojoules (10^{-9} J) are used to prevent damaging the sample, which requires photomultiplier tubes to amplify the resulting weak HG signal. Further, high numerical aperture (NA) focusing objectives (NA > 0.8) are used for precise optical sectioning and for gathering as much of the weak harmonic signal as possible. For ophthalmic procedures, pulse energies are approximately 1 µJ, 2-3 orders of magnitude larger, and focused at relatively low NA, approximately 0.1-0.3. Therefore, it can be expected that HG will be significantly more intense when using therapeutic FSLs. To this regard, the first objective of this study was to determine specific tissue layer contributions to HG processes using therapeutic FSLs.

4.2.1 Material and methods

To elucidate the effects of tissue layer on SHG and THG, the setup illustrated in Figure 34 was employed. A diode-pumped FSL (1042-nm, 300-fs; Spectra Physics) was focused onto the cornea sample using a single plano-convex lens (50 mm focal length) to minimize group velocity dispersion. The repetition rate and pulse energy were maintained below LIB threshold at 100
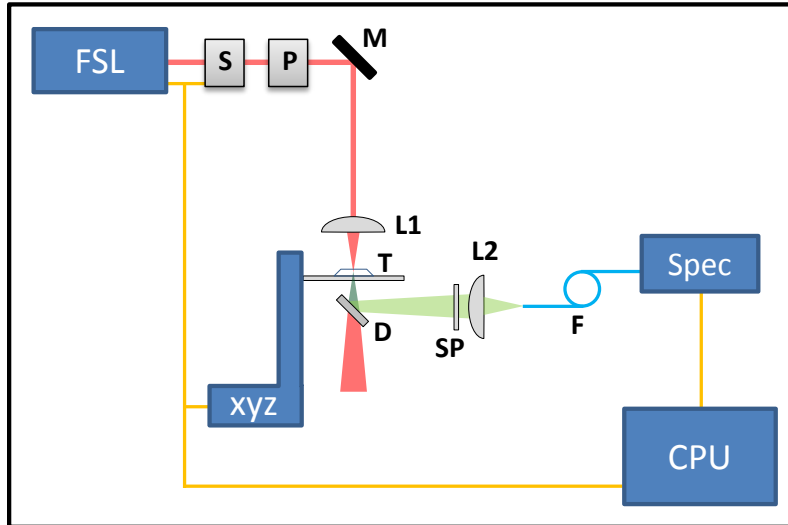
Figure 34. Principle optical experimental setup for measuring tissue (T) harmonic generation using a computer-controlled (CPU) femtosecond laser (FSL), shutter (S), translation stage (xyz), and spectrometer (Spec). M mirror; L1, L2 lens; D dichroic beam splitter; SP short-pass filter; F fiber.

kHz and 300 nJ respectively. The laser beam was linearly polarized by a Glan-Laser type polarizer (Thorlabs). Laser exposure and corneal sample position were controlled using an automated shutter and 3-axis micro-positioning stage. Transmitted SHG and THG were separated from the fundamental wavelength using a dichroic long-pass filter (Edmund Optics) and collected using a fiber coupling lens (Thorlabs) and 600-μm core diameter fiber (Ocean Optics) attached to a spectrometer (Ocean Optics). A short-pass edge filter (Semrock) was used to remove any remaining fundamental frequency prior to fiber coupling.

Freshly enucleated bovine globes were obtained from a local slaughterhouse and stored on ice. Immediately prior to testing, a 10-mm trephine was used to remove the central cornea. The corneal button was placed on a glass slide and positioned in front of the laser. Several drops of BSS were added to the cornea to prevent corneal drying. Only corneas that appeared clear and lacking any pathologies were used.

SHG and THG intensity were measured as the corneal button was scanned through the laser focus as depicted in Figure 35. A custom LabVIEW program automated the corneal button positioning, laser exposure and spectrophotometric measurements. The spectrometer acquired one data point per corneal position with a 20-µm step size.
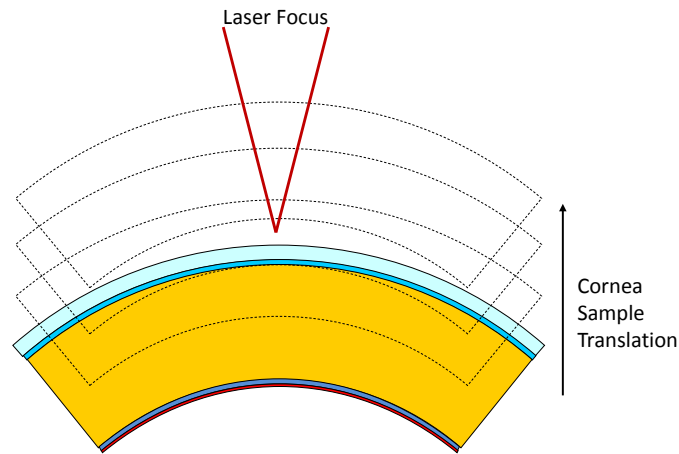
Figure 35. Direction of corneal tissue motion during depth specific harmonic generation measurements.

4.2.2 Results

The spectral intensity was recorded at each focal position for the entire z-scan (Figure 36(a) and 36(b)). To better compare SHG and THG occurrence, the spectral intensity at the specific wavelengths 521 nm and 347 nm, representing SHG and THG respectively, were plotted together (Figure 36(c) and 36(d)). After scanning 60 locations on 6 corneal buttons, two HG patterns emerged. In all cases, a strong broad SHG peak was observed that corresponded with the bulk of the corneal button thickness.

Several narrower THG peaks occurred. THG peaks commonly appeared before and after the tissue thickness that correlated with the air-BSS interface and the slide-air interface respectively (Figure 36(c)). THG peaks also occurred at locations that surrounded the SHG peak and were spaced approximately 1-mm apart, the tissue thickness (Figure 36(d)). These peaks
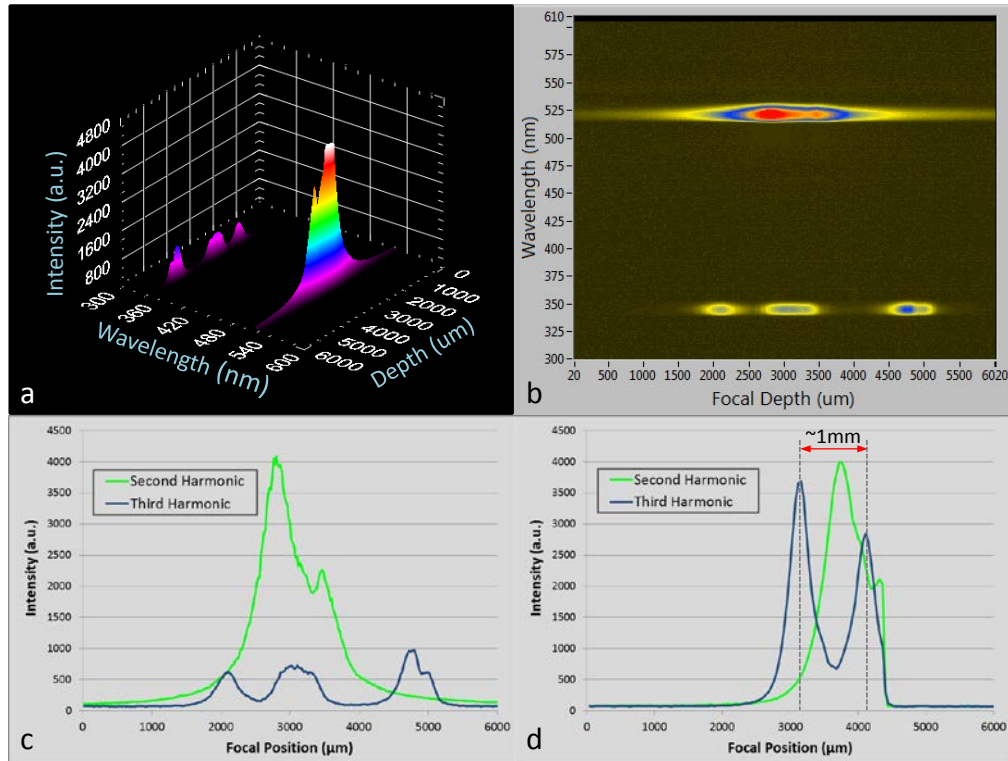
Figure 36. Second and third-harmonic generation measurements with respect to corneal depth presented in (a) 3-D and (b) intensity plots, and (c),(d) 2-D profile plots.

corresponded with the BSS-cornea interfaces. In most cases, although weak, there was also THG present in the central tissue region, occurring with SHG.

The SHG signal was significantly stronger than THG, saturating the detector at times. In these situations, in order to make comparisons with THG peaks, the SHG intensity was plotted for a wavelength several pixels away from 521nm, the central SHG wavelength.

4.2.3 Discussion

The results of this study support many of the HG features seen in NLM with some exceptions. As expected, the intensity of both SHG and THG were significantly greater than that generated in NLM, simply demonstrated by the ability to detect these signals without any powerful multi-order amplification such as that provided by photomultiplier tube detection approaches employed in NLM designs. In fact, the harmonics are visible to the naked eye.

71

THG produced peaks whose position corresponded to changes in significant refractive index such as the interfaces between Air-BSS, BSS-epithelium, endothelium-glass, and glass-air. Although THG can occur in both centrosymmetric and noncentrosymmetric, homogenous materials, when using a focused beam with Gaussian intensity profile, the Gouy shift that occurs near the laser focus results in destructive interference between harmonics generated before and after the focus [82, 121]. However, at locations with optical inhomogeneities, the destructive interference is disrupted and THG can occur [121].

There was variability in THG peak appearance and intensity, with not all tissue scans producing THG peaks at all interfaces. This variability can be explained by the 20-µm step size used for tissue translation along the z-axis. The step size was chosen so that the full thickness of tissue could be scanned before thermal effects began to deteriorate the tissue. Although below the LIB threshold, thermal effects can accumulate if the tissue is exposed to the laser for longer periods of time due to linear absorption at the fundamental wavelength. The initial tissue position was chosen so that the laser focus began comfortably above the tissue. Further, given a certain amount of intercorneal thickness variation, the laser spectral intensities were recorded at random locations with respect to optical landmarks, with the possibility that the laser focal position could be located up to 10 µm away from an optical interface. Additional variability in peak intensity is due to varying phase mismatch, caused by different collagen orientations. This concept will be explored further later in the Chapter.

SHG was emitted from the corneal stromal region, however, in most cases the broad peak extended beyond 1 mm, the average bovine corneal thickness [36]. This result is a product of the large Rayleigh range, or confocal parameter. Focusing the 4-mm-diameter beam using a lens with 50 mm focal length produces a Rayleigh range of approximately 415 µm. As the optical

field intensity is approximately constant over this range, SHG occurs over a similar, but slightly smaller scale. As the beam waist approaches the stromal boundary, the Raleigh range extends into the stroma and generates a second harmonic signal that gradually grows until the full Rayleigh range is contained within the stroma. The opposite progression occurs as the Rayleigh range begins to exit the tissue. A similar effect can be seen with THG at the previously mentioned interfaces. Ophthalmic surgical lasers typically use lower numerical apertures than those used in NLM and therefore will likely generate both SHG and THG over a range that extends beyond the precise dimensions of the cornea and the location of its interfaces.

Another product of using lower numerical apertures is decreased resolution on the optical axis. This may have resulted in averaging of HG over a longer tissue volume, proportional to the Rayleigh range. For this reason, individual smaller peaks associated with the lamellae structure as well as corneal layer interfaces such as the epithelial-stromal boundary cannot be seen as they are in NLM [23, 126].

4.3 Collagen orientation

An important relationship for nonlinear processes is the orientation of the material with respect to the electric field vector or laser polarization. In the case of corneal tissue, the important relationship is the orientation of collagen fibrils with the laser polarization. Individual collagen molecules have a triple helix structure [127] and organize into fibrils 30 nm in diameter. The helices are aligned parallel to each other and approximately parallel to the fibril axis. Collagen in the cornea is primarily type 1. The fibrils are organized parallel to each other into lamellae which are oriented approximately parallel to the corneal surface and therefor in the same plane as the electric field vector of the laser. Although the angles between adjacent lamellae vary, there

appears to be preferential angles that correspond with stromal depth. Using scanning (SEM) and transmission (TEM) electron microscopy techniques, Radner et al. measured the angle between adjacent lamellae in the central cornea throughout the thickness of the stroma. In the anterior section, they found a higher proportion of angles at or near 45 degrees with about 17 percent of the angles greater than 85 degrees. In the posterior layers, the major proportion of angles were near 90 degrees [34]. This trend was confirmed by Morishege et al. Using SHG microscopy they found a similar progression toward orthogonal orientation with stromal a depth. They also showed that despite the overall parallel orientation of lamellae with respect to the cornea surface, some lamellae in the anterior stroma were transverse with a z-component to their orientation.

Figure 37 diagrams a laser beam focused onto a single collagen fibril aligned with the x-axis. The second harmonic dipole moment induced in the collagen molecule ($\mu_{2\omega}$) by the incident electric field (E_w) which is parallel to the plane containing the collagen fibril can be expressed as

$$\vec{\mu}_{2\omega} = \frac{1}{2}\vec{E}_\omega^2 \times \begin{pmatrix} \beta_{xxx}\cos^2\alpha + \beta_{xyy}\sin^2\alpha \\ \beta_{xyy}\sin 2\alpha \\ 0 \end{pmatrix}, \tag{27}$$

where, α is the angle between the incident electric field polarization and the collagen fibril, and β_{xxx} and β_{xyy} are the hyperpolarizability along the collagen fibril in the x- (along the fibril axis) and y-directions (across the fibril), respectively [128-130]. $\boldsymbol{\beta}$ is directly related to the second order nonlinear susceptibility, $\boldsymbol{\chi}^{(2)}$, by the following relation:

$$\boldsymbol{\chi}^{(2)} = N\boldsymbol{\beta}, \tag{28}$$

where, N is the volume density of molecules contributing to the polarization. If a linearly polarized laser along the x-axis is assumed ($\alpha = 0$), Equation (27) then becomes:
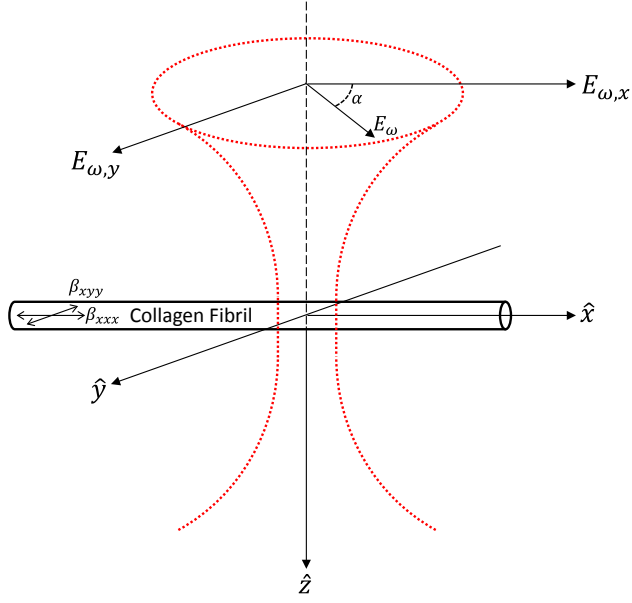
Figure 37. Geometric description of laser-collagen interactions.

$$\vec{\mu}_{2\omega} = \frac{1}{2}\vec{E}_{\omega}^2 \times \begin{pmatrix} \beta_{xxx} \\ 0 \\ 0 \end{pmatrix}, \tag{29}$$

which allows the omission of the vectorial nature of the components and the equation simplifies to

$$\mu_{2\omega,x} = \frac{1}{2}E_{\omega}^2\beta_{xxx} . \tag{30}$$

Similarly, if the incident field is polarized in the *y*-direction ($\alpha = \frac{\pi}{2}$), Equation (27) simplifies to

$$\mu_{2\omega,y} = \frac{1}{2}E_{\omega}^2\beta_{xyy} . \tag{31}$$

And since the material nonlinear polarization is related to the induced dipole by

$$\boldsymbol{P}^{(2)} = N\vec{\mu}_{2\omega} \tag{32}$$

it is apparent that the laser polarization has a strong effect on the induced nonlinear polarization.

SHG dependence on laser polarization can be related to the ratio of longitudinal to transverse hyperpolarizabilities $\rho = \beta_{xxx}/\beta_{xyy}$ which is approximately 2.6 for type 1 collagen

75

[129, 131, 132]. This indicates that the fibril has a significantly higher susceptibility along the length of the fibril and will generate a stronger second harmonic signal when the laser polarization is aligned with the fibril axis. Both theoretical studies [84, 128, 129]and experimental data [130, 133] support this notion.

The other important determinant of SHG is phase matching. As previously shown in Chapter 3.3, cornea tissue has a strong birefringent effect on IR FSL pulses [95]. Therefore the phase mismatch between the fundamental and second harmonic frequencies due to dispersion will vary as the laser polarization with respect to the corneal collagen orientation varies. As the phase mismatch decreases, the SHG efficiency will increase and vice versa.

Unlike many of the theoretical and experimental studies that examine the effect of FSL polarization on single collagen fibrils, or single groups of aligned fibrils, using low intensity microscopy-based FSLs and high NA focusing lenses for high resolution axial sectioning, therapeutic lasers use high power FSLs and low NA lenses that induce nonlinear polarizations in a larger depth of focus. In order to determine the affect laser polarization has on SHG induced by a therapeutic FSL in corneal tissue, composed of a superposition of lamellae with different alignments, the following study was conducted.

4.3.1 Materials and methods

A diode-pumped FSL (1042-nm, 300-fs; Spectra Physics) delivered a 4-mm-diameter collimated beam through central corneal tissue (Figure 38). The repetition rate and pulse energy were maintained below LIB threshold at 100 kHz and approximately 1 µJ, respectively, in order to collect data over the time required to complete 360 degrees of polarization rotation (approximately one minute). The corneal tissue was placed onto a microscope slide which was attached to an X-Y translation stage. A polarizing beam splitter (PBS) was used to purify the
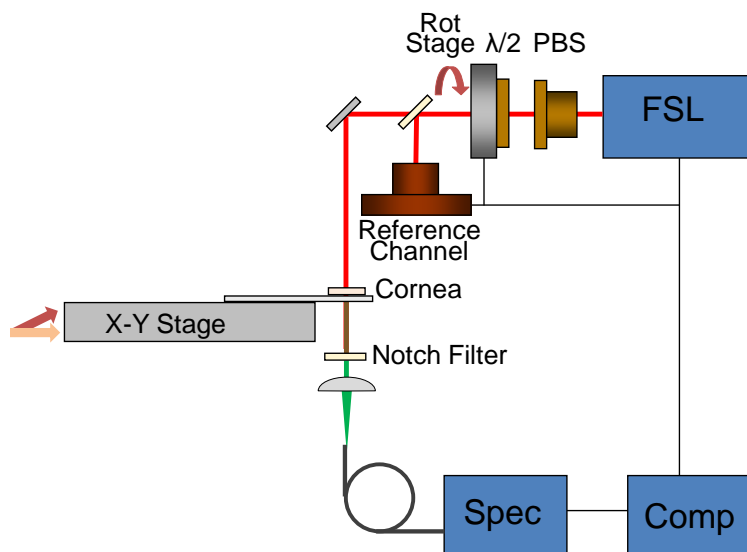
Figure 38. Principle optical experimental setup for measuring second-harmonic generation with respect to collagen orientation using computer (comp) controlled half wave plate (λ/2) and spectrometer (spec). PBS polarizing beam splitter.

laser's linear polarization. A half wave plate (HWP) mounted on a rotational stage was used to rotate the polarization. SHG was measured using a spectrometer as the HWP was rotated 180 degrees with a 2.5 degree step size. A notch filter was used to remove the FSL fundamental wavelength from SHG.

The central cornea of freshly enucleated whole bovine globes was removed using an 8-mm trephine. Five locations separated by 1 mm on each of 4 corneas were sampled for a total of 20 locations. Only transparent, healthy appearing corneas were used. The normalized maxima and minima SHG intensities were averaged and then subtracted to produce an average change in SHG intensity for each corneal location.

4.3.2 Results

A typical plot of SHG intensity as a function of the laser polarization angle with 4 maxima and 4 minima can be seen in Figure 39. Although there was a general sinusoidal appearance to the plots, they weren't ideal and there was some variation from true sinusoidal oscillation. Most

77
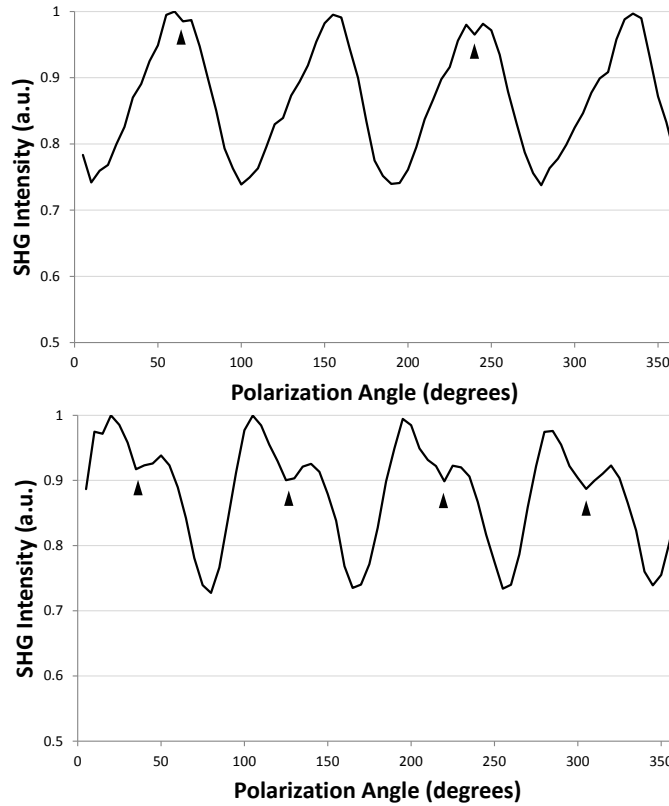
Figure 39. Typical second-harmonic generation measurements with respect to laser polarization containing some repeating inconstancies (arrowheads).

plots displayed some type of periodic discrepancy (Figure 39(a) and 39(b), arrow heads). The distribution of average SHG intensity ranges for each location is plotted in Figure 40. The average change in SHG intensity with respect to laser polarization was $21.6 \pm 5\%$. The majority of locations had between 17% and 23% variation in SHG intensity.

4.3.3 Discussion

The sinusoidal nature of the data suggests that the birefringent property of the corneal stroma affected SHG efficiency periodically. Having a period of $\pi/2$, the data corresponds to a model of stromal birefringence, which was demonstrated in Chapter 3. The phase mismatch associate with the fundamental and second harmonic frequencies in type 1 collagen is

$$\Delta k = 2k_\omega - k_{2\omega} = \frac{2\omega|n_\omega - n_{2\omega}|}{c} = 2.63 \times 10^5 \qquad (33)$$

The resulting coherence length (L_{coh}) can be found using the simple relation:

$$L_{coh} = \frac{\pi}{|\Delta k|} . \qquad (34)$$

In this case a coherence length of 11.94 μm is produced. The phase mismatch can be reduced as the polarization is rotated allowing the birefringence associated with the bulk tissue to reduce the difference in refractive index due to chromatic dispersion associated with the two wavelengths. Using the phase rotation caused by corneal birefringence, which was found in the previous experiment, the difference in refractive index between the two principle axes can be calculated using this equation:

$$n_y - n_x = \Delta n = \frac{\Delta \emptyset \lambda}{2\pi d} , \qquad (35)$$

where, $\Delta \emptyset$ is the polarization rotation expressed in radians, d is the sample thickness and n_y and n_x are the principle refractive indices. The calculated change in refractive index associated with 47.35 degrees average rotation is $\Delta n = 1.379 \times 10^{-4}$. This corresponds very well to $\Delta n = 1.4 \times 10^{-4}$ reported by van Blokland and Verhelst in their experimental study of corneal polarization
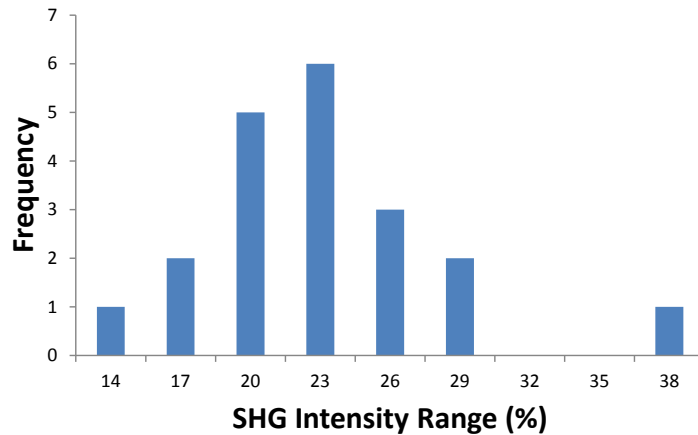
Figure 40. Distribution of average second-harmonic generation intensity fluctuation values for all corneas.

using a low-power, cw laser source [93] and calculated by Mission [92] in his theoretical model of corneal birefringence, and to the estimated value found in the scanning laser polarimetry study by Knighton et al. [94], $\Delta n = 1.2 \times 10^{-4}$. Using the calculated difference in refractive index to offset the material dispersion the reduced phase mismatch and resulting coherence length are 2.59×10^5 and 12.09 µm, respectively. The change in SHG intensity associated with the phase matching provided by the tissue birefringence can be calculated using the following relationship,

$$I_{SHG}^{max} \propto \frac{1}{\Delta k^2} , \tag{36}$$

where, I_{SHG}^{max} is the maximum SHG intensity. Using this relationship and the phase mismatches for the conditions of no BPM and maximum BPM, the difference in maximum SHG intensity is found to be 2.6%. This is relatively small compared with the average change in intensity that was seen with laser polarization rotation, which indicates that BPM contributes only a small amount of the observed polarization dependence of SHG.

The majority of the polarization effect is therefore due to the polarization sensitive interactions of the fundamental field with collagen fibrils. This agrees well with the previously established collagen organization of the stroma. As the stroma lamellae have a preferred orthogonal orientation [34, 133-135], rotating the laser polarization 360 degrees will produce SHG oscillations with a period of $\pi/2$ as peak SHG will occur when the laser polarization is parallel with a lamellae orientation.

Since a collimated beam was used in this experiment and the extinction coefficient at this frequency is low, there is contribution to the second harmonic signal from lamellae throughout the stromal beam path. Perpendicularly orientated lamellae are concentrated in the posterior third of the stroma. The anterior two thirds contain more randomly oriented lamellae [133, 135]. The contribution to the SHG signal that these randomly oriented lamellae provide as the polarization

is rotated can be thought of as a superposition of individual smaller sinusoids with different phases and smaller amplitudes. This explains the substantial SHG signal regardless of polarization. Depending on the specific lamellae orientations in the beam path the superposition of SHG signals could lead to the periodic discrepancies seen in Figure 39 or simply to the waveform's departure from a symmetric oscillation.

As the coherence length of the nonlinear interaction is on the same scale as the lamellar thickness in the posterior stroma, approximately 5-9 μm [133], coherent addition from multiple lamellae in the posterior stroma in a similar manor to quasi-phase matching (QPM) may explain the reasonably strong HG that was observed. QPM is a technique to compensate for a nonzero phase mismatch by periodically changing the material orientation and therefore the nonlinear susceptibility. This avoids destructive interference that normally occurs once the harmonic wave propagates past the coherence length when the field strength would normally decrease. Instead, the susceptibility changes and the wave grows in this coherent amplification process. This theory is supported by the work of LaComb et al. [83]. QPM is likely the cause of the polarization sensitivity at specific orientations and the reason why a more constant SHG signal isn't produced at all polarization angles. Finally, the dependence on laser polarization may be even stronger in human corneal tissue which has a higher concentration of orthogonally oriented lamellae when compared with bovine corneal tissue [133].

4.4 Collagen crosslinking

Changes in collagen structure can manifest in certain corneal pathologies that hinder or completely disrupt proper refraction as part of the visual process. One example that has received much attention recently is keratoconus. Keratoconus is characterized by the thinning and conical

growth of the cornea and occurs in about 1 in 2000 people. It normally occurs bilaterally and affects vision significantly, with about 20% of patients undergoing full penetrating keratoplasty to prevent further degradation in vision. Other, less invasive treatments only target the refractive error and don't address the continuous progression of the disease [136]. EM and X-ray scattering measurements have shown a reduced number of transverse lamellae running from the anterior to posterior stroma [137, 138], which normally provide support for the stress bearing anterior stromal lamellae. Further, it has been shown that there is a significant difference in elasticity between corneas with Keratoconus and healthy ones [139, 140]. For these reasons, a less invasive treatment called corneal crosslinking (CXL) has emerged. CXL uses topical application of riboflavin and UV light to induce intermolecular crosslinking in collagen that stiffens the cornea tissue. Crosslinks between individual collagen molecules push the molecules apart increasing molecular spacing [141] which then increases collagen fibril diameter [142]. CXL causes a differential fibril diameter increase from the anterior to posterior stroma as UV light attenuation increases with optical path length.

Penetrating keratoplasty, the primary treatment for advanced cases of keratoconus, requires a healthy donor cornea. For reasons described in Chapter 3, availability of fresh donor corneas are a major factor preventing cornea transplantation in less developed nations. Further, regardless of donor tissue availability, given the young age at which corneal transplant is performed to treat keratoconus, immune related rejection is commonly occurs. This further supports the use of a sterilized graft, as discussed in Chapter 3, to replace fresh donor tissue. Gamma (γ)-irradiation is used to terminally sterilize the graft. A side effect of γ-irradiation of collagen structures is that it can change the amount of collagen crosslinking, either increasing or decreasing it.

82

Since collagen fibril size and spacing influence HG, crosslinking associated with CXL or corneal sterilization may also affect SHG in corneal tissue. This may be of particular interest in the case that a patient who has undergone CXL to halt progression of Keratoconus and then undergoes any FSL-based procedure [143]. Further, changes in HG may provide insight on the fundamental nonlinear interactions and relationship to collagen fibril size and spacing. In this study, differences in HG are examined in sterilized, γ-irradiated human corneas and fresh human corneal tissue.

4.4.1 Materials and methods

In order to measure HG in 2 human corneas types, fresh donor corneas and γ-irradiated (VisionGraft, Tissue Banks Internationa), an experimental setup similar to the previous study was used (Figure 38). FSL parameters were constant for all samples (100 kHz, 300 fs, 1 μJ), and a removable focusing lens (50 mm focal length) and z-axis translation stage for translating the tissue along the optical axis were added. SHG was generated in 4 corneas, 2 fresh and 2 γ-irradiated human donor corneas. The laser was focused into the mid-stroma at 4 locations and unfocused in one location for each cornea. The laser focus was positioned into the stroma by advancing the tissue toward the laser focus until a peak in SHG was generated. Transmitted HG intensity was measured using a spectrometer as the laser polarization was rotated. The polarization was rotated 360 degrees with a 4 degree step size. Cornea position, polarization rotation, laser shutter and HG intensity collection were controlled using a custom LabView program.

4.4.2 Results

As expected, SHG intensity varied with polarization rotation, similar to the previous experiment using bovine corneas. SHG and THG intensity were averaged for each cornea and for all samples

of each cornea type (Figure 41). Sterile, gamma-irradiated tissue produced significantly more SHG and THG than fresh donor tissue. As there were a limited number of unfocused samples, HG intensity was only averaged for each cornea type (Figure 42). Similarly, sterile tissue produced more SHG and THG than fresh donor tissue.

In both fresh and sterile cornea, focused FSL pulses generated more intense SHG and THG than unfocused laser–cornea interactions.

4.4.3 Discussion

HG was compared in two human cornea types, one with natural stromal collagen structure and one with an altered collagen structure. The results showed a significant difference in both SHG and THG intensity between the two cornea types. The γ-irradated, sterile corneas produced significantly more intense SHG and THG signals than fresh donor tissue. This increased HG intensity seems to be related to collagen fibril size or spacing with respect to the coherence length of the nonlinear interaction. Ideal QPM occurs when the following relationship is met:

$$L_{pole} = 2L_{coh} = \frac{2\pi}{|\Delta k|} , \tag{37}$$

where, L_{pole} is the length of one period of material susceptibility alternation[82], which is
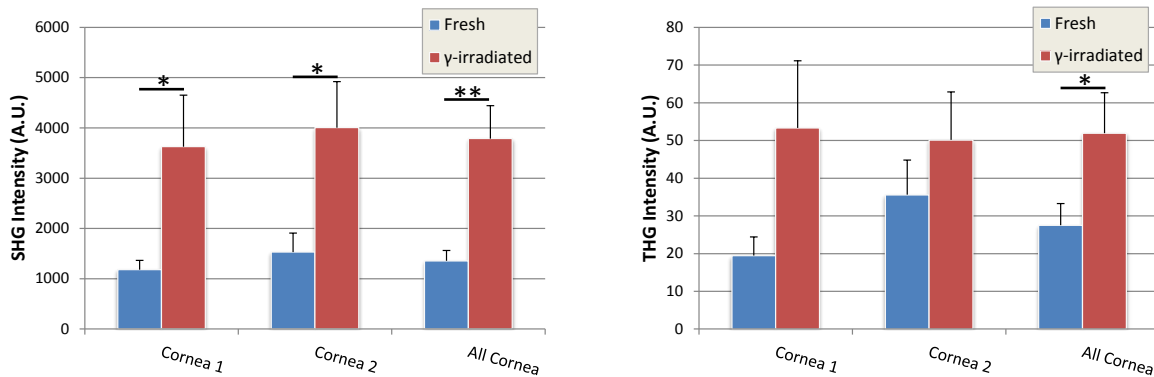
Figure 41. (a) Second- and (b) third-harmonic generation measurements induced by collimated femtosecond laser beam in fresh and gamma-irradiated corneal tissue; *p<0.05, **p<0.005.

comparable to the lamellae spacing in this context. This relationship will determine the quality of the QPM, which greatly determines the intensity of the generated harmonics. Sikder et al. determined that γ-irradiation caused no significant change in collagen fibril size in VisionGraft γ-irradiated corneas. However, they did find a change in collagen fibril spacing in the posterior cornea, but not in the anterior portion [144]. This finding correlates with the previous conclusion that SHG occurs most efficiently in the posterior stroma where a process similar to QPM can occur in the presence of a higher concentration of periodically spaced perpendicularly oriented collagen fibrils. Consequently, changes in collagen spacing in this region will likely have a prominent effect on SHG, as seen in the results. Increased fibril spacing caused by γ-irradated is also supported by the work of Chae et al. who characterized Vision Graft cornea using differential scanning calorimetry. They found that γ-irradated corneas have a decreased melting temperature compared to fresh corneal tissue, which is indicative of decreased crosslinking density [145]. Decreased crosslinking can also be related to an increase in interfibril spacing [146]. Increased interfibril spacing in γ-irradated corneas may have led to the observed increase
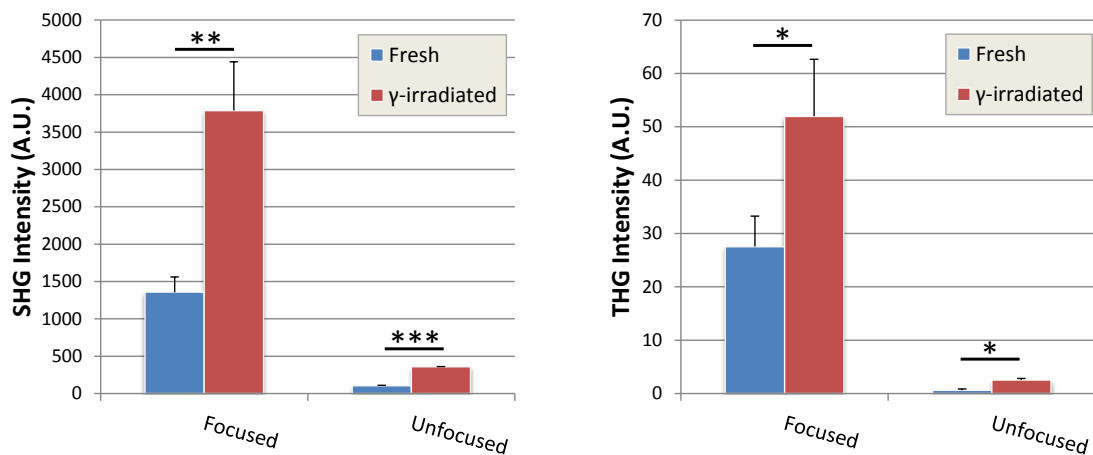
Figure 42. (a) Second- and (b) third-harmonic generation measurements induced by focused and collimated femtosecond laser beam in fresh and gamma-irradiated corneal tissue. *p<0.05, **p<0.01, ***p<0.0001.

in HG intensity by reducing the difference between L_{coh} and the distance between parallel lamellae in the orthogonally oriented posterior stroma.

Focusing the FSL generated more intense HG than unfocused FSL interactions. As HG is proportional to the field strength of the fundamental frequency and focusing the laser generates field strengths orders of magnitude larger than unfocused pulse, this outcome is expected. Further, although unintentional, the method used for positioning the laser focus within the stroma likely positioned the focus within the posterior stroma where QPM, and more efficient HG, occurs.

4.5 Conclusions

After examining the relationship that tissue composition (depth location), collagen orientation and collagen crosslinking have on HG, it is apparent that each of these tissue properties has a significant impact on HG induced with high-power FSLs. SHG and THG varied greatly depending on the depth of the laser focus. At certain locations SHG occurred alone, THG occurred alone, or both occurred simultaneously. The relative intensity also varied with corneal depth. Varying the collagen orientation with respect to the laser polarization produced a significant oscillation in SHG intensity where BPM only provides a minor reduction in phase mismatch, while QPM seems to play a more dominant role. Lastly, the degree of collagen crosslinking also has a significant effect on both SHG and THG and seems to be related to collagen fibril spacing.

The improved understanding of the impact on HG that each of these tissue properties has should be taken into consideration when developing a treatment strategy in order to minimize unwanted effects from generating coherent harmonic frequencies in the eye, an organ very

sensitive to optical frequencies. Safety aspects will be considered in detail in Chapter 6. From the opposite perspective, the relationship between tissue properties and HG may be exploited to benefit current and future ophthalmic procedures by providing information about local tissue properties, such as orthogonality, degree of crosslinking and collagen fibril spacing. For example, this knowledge may be used to target specific corneal locations, monitor progress of FSL based treatments, or simultaneously evaluate therapeutic results.

Chapter 5 – Laser Specific Effects on Harmonic Generation

5.1 Introduction

Similar to corneal tissue properties, laser parameters also play an important role in the FSL-tissue interactions leading to HG. As HG intensity is proportional to the square of the optical field, laser parameters that affect the field intensity are important to consider. Important FSL parameters include numerical aperture (NA), pulse duration, pulse energy and fundamental laser wavelength (optical frequency). Further, as the potential impact on ocular safety will be considered, the repetition rate of the laser is also important to consider. As most clinical FSLs operate at similar fixed wavelengths (1040–1060 nm) and pulse durations (300-500 fs) [18, 55] that the surgeon cannot adjust, pulse repetition rate, NA and pulse energy are more relevant to inter-patient and inter-device HG variation. Depending on the patient's corneal anatomy, the type of procedure being performed and the preferences of the surgeon, the laser pulse energy can be adjusted, in addition to other scanning settings. The therapeutic FSL requires stable coupling the patient's eye to provide a precise, predictable optical interface through which the laser is focused. As the coupling technique varies between devices with some using corneal applanation and others using curved interfaces, the focusing optics cover a range of NAs. Lastly, as newer FSL are developed to improve the precision, quality, speed and range of ocular surgical procedures, FSLs with higher pulse repetition rates are being developed (see Chapter 2.2.3).

FSLs are typically characterized by their pulse properties since the pulse duration and photodisruption occur on a time scale much smaller than the period between pulses. The optical intensity of the pulse, I_{pulse}, can be found using this formula:

$$I_{pulse} = \frac{\left(\frac{E_{pulse}}{t_{pulse}}\right)}{A}, \tag{38}$$

where, t_{pulse} and E_{pulse} are the time duration and energy contained within a single femtosecond pulse, respectively, and A is the cross-sectional area of the laser beam at the focus. For a laser beam with Gaussian intensity profile at small focal angles, A can be found using the following equations:

$$A = \pi w_0^2, \tag{39}$$

$$w_o = \left(\frac{2\lambda}{\pi}\right)\left(\frac{F}{D}\right), \tag{40}$$

where, w_o is the waist radius of the beam (radius at the laser focus), F is the focal length of the lens and D is the lens aperture.

5.2 Effect of pulse energy, repetition rate and numerical aperture on harmonic generation intensity and duration

Ophthalmic surgical procedures utilize FSLs with intensities three orders of magnitude higher than intensities used for imaging applications [55]. Other NOEs occurring also at significantly lower intensities, such as self-focusing and filamentation, have recently been studied using therapeutic FSL parameters [116, 117, 147]. SHG and THG have been reported during photodisruption in corneal tissue [116, 117, 148], but no investigation to has examined the relationship between laser parameters and HG characteristics at these energy levels. As NOEs

such as HG are greatly dependent on laser intensity, an investigation of the relationships between HG elicited by clinically important FSL parameters at these energy levels is warranted.

Currently, FSLs can be grouped into two major classes (see Chapter 2.2.3). Conventional FSLs employ lower pulse repetition rates (kHz) and higher (μJ) pulse energies. In an attempt to further improve precision and reduce collateral effects, the new regime of FSLs employ higher repetition rates (MHz) and lower (nJ) pulse energies, which allow for more precise and smooth tissue cutting [13, 55]. Since HG is dependent on laser intensity, different classes of FSLs may produce different degrees of HG.

The following investigation examines the influence that NA, pulse energy and repetition rate have on SHG and THG intensity and duration produced in corneal tissue [149].

5.2.1 Materials and methods

To induce HG in corneal tissue and quantify the transmitted light, the setup illustrated in Figure 43 was employed. A 1042-nm wavelength, 300-fs pulse duration FSL (Spectra Physics) was focused onto the cornea sample using single plano-convex lenses to avoid temporal pulse dispersion. Laser exposure and corneal sample position were controlled using an automated shutter and 3-axis micro-positioning stage. Transmitted SHG and THG were separated from the fundamental wavelength using a dichroic long-pass filter (Edmund Optics) and collected using a fiber coupling lens (Thorlabs) and 600-µm core diameter fiber (Ocean Optics) attached to a spectrometer (Ocean Optics). A short-pass edge filter (Semrock) was used to remove any remaining background at the fundamental wavelength prior to fiber coupling.

Freshly enucleated bovine globes were obtained from a local slaughterhouse and stored on ice. Immediately prior to testing, a 10-mm trephine was used to remove the central cornea. The corneal button was placed on a glass slide and positioned in front of the laser. Several drops
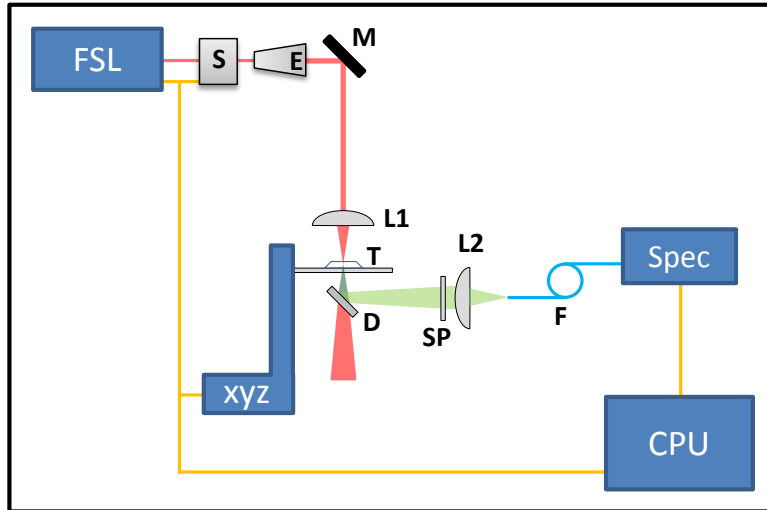
Figure 43. Principle optical experimental setup for measuring tissue (T) harmonic generation intensity and duration with respect to femtosecond laser pulse energy repetition rate and numerical aperture using a computer-controlled (CPU) femtosecond laser (FSL), shutter (S), translation stage (xyz), and spectrometer (Spec). M mirror; L1, L2 lens; D dichroic beam splitter; SP short-pass filter; F fiber. Reprinted with permission from W. R. Calhoun, 3rd and I. K. Ilev, "Effect of therapeutic femtosecond laser pulse energy, repetition rate, and numerical aperture on laser-induced second and third harmonic generation in corneal tissue," Lasers Med Sci, Mar 17 2015. Copyright 2015, Springer Science and Business Media.

of balanced salt solution were added to the slide to prevent corneal drying. For testing FSL repetition rate and pulse energy, specific combinations of laser parameters were randomly assigned to positions on a 1-mm spaced grid to ensure no locations were overlapped and to avoid effects of regionally specific tissue parameters, if present. Using 5 corneas, each combination of parameters was tested 20 times, 4 per cornea. For the effect of changing NA, each NA was tested at 13 locations on each of 2 corneas. Measurements were completed within 15 minutes of trephination of each cornea.

SHG and THG intensity and duration were measured for every combination of three FSL repetition rates (100 kHz, 500 kHz and 1 MHz) and three pulse energies (0.38 µJ, 0.94 µJ and 1.89 µJ). The FSL pulse energies are determined using the average power values measured after the focusing lens. In addition, SHG and THG intensity were measured for 3 different NAs (0.148, 0.169, and 0.233) by changing the focusing lens, while maintaining the pulse energy and

repetition rate constant at 1.89 µJ and 100 kHz, respectively. A custom LabVIEW program automated the sample positioning, laser exposure (900 ms) and spectrophotometric measurements. High-speed spectrometer acquisition was started immediately prior to each laser exposure and ended after shutter closure. For this study, HG optical intensity is defined in arbitrary units as the highest achieved intensity during the laser exposure, and duration is defined as the time spent above a threshold set slightly above the noise level.

Data for each laser parameter combination or NA were averaged over all cornea samples and compared with each other using a Student's t-test assuming unequal variance to determine statistical significance. Differences were considered significant for p-values < 0.05. Ninety-five percent confidence intervals were calculated for each group with values stated as mean ± 95% confidence bound.

5.2.2 Results

In general, SHG was considerably more intense than THG. Figure 44 illustrates typical experimentally recorded SHG and THG signals which are plotted as intensity distribution as a function of time (Figure 44).

Mean SHG and THG intensity, grouped by pulse energy, are summarized in Figure 45. For all pulse energies, SHG and THG intensity increased with repetition rate. Exposures using 1 MHz repetition rates produced some of the highest HG intensities. The 100 kHz repetition rates produced the largest variability.

Mean SHG and THG duration are summarized in Figure 46. As the temporal resolution of the spectrometer was about 10 ms, HG intensity produced by the FSL pulse train is integrated over multiple pulses and appears as a continuous plot, despite the individual HG pulses having durations similar to the FSL pulses. As opposed to HG intensity, for each pulse energy, SHG
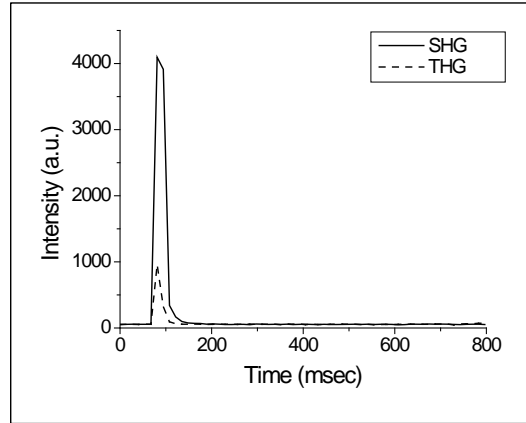
Figure 44. Typical experimentally recorded second- and third- harmonic generation signal intensity with respect to time. Reprinted with permission from W. R. Calhoun, 3rd and I. K. Ilev, "Effect of therapeutic femtosecond laser pulse energy, repetition rate, and numerical aperture on laser-induced second and third harmonic generation in corneal tissue," Lasers Med Sci, Mar 17 2015. Copyright 2015, Springer Science and Business Media.

duration decreased with increasing repetition rate. In the case of THG, duration for 100 kHz was substantially longer than 500 kHz and 1 MHz in the 0.38 μJ and 0.94 μJ pulse energy groups. THG duration in the 1.89 μJ pulse energy group increased with increasing repetition rate. THG duration was shorter than SHG duration. In general, 1 MHz repetition rates generated the highest HG intensities but shortest durations while 100 kHz repetition rates generated the lowest HG intensities and longest durations.

The resulting SHG and THG intensity for the three NAs tested is summarized in Figure 47. There was a corresponding increase in SHG and THG intensity with increasing NA, however increases in THG intensity were small in comparison with SHG.

5.2.3 Discussion

Repetition rate, pulse energy and NA are important FSL parameters for achieving the desired tissue cutting therapeutic effect in many ophthalmic procedures employing FSLs. This study aims to evaluate the dependence of harmonic generation in corneal tissue on these key laser parameters that are similar to those used in current therapeutic applications. The results of this
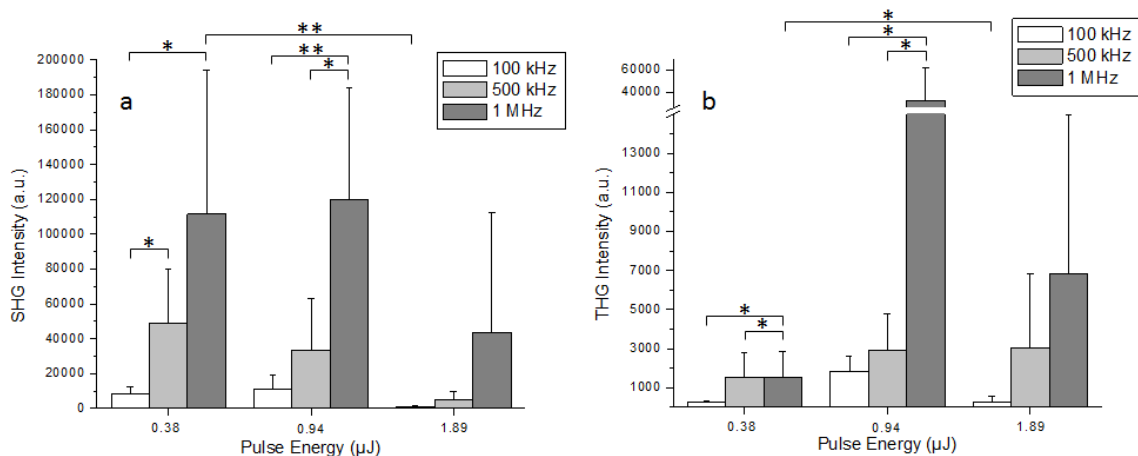
Figure 45. (a) Second-harmonic generation and (b) third-harmonic generation intensity as a function of femtosecond laser pulse energy and repetition rate; *p<0.05, **p<0.01. Reprinted with permission from W. R. Calhoun, 3rd and I. K. Ilev, "Effect of therapeutic femtosecond laser pulse energy, repetition rate, and numerical aperture on laser-induced second and third harmonic generation in corneal tissue," Lasers Med Sci, Mar 17 2015. Copyright 2015, Springer Science and Business Media.

initial study do not include the exact replication of specific ophthalmic surgical procedures, which may involve some special scanning of the laser focus. Although not directly observed, the concurrence of photodisruption, the therapeutic effect, is predicted since the minimal intensity generated by the FSL parameters was approximately 8×1012 W/cm2, which is twice the threshold for LIB [15]. This was confirmed experimentally by the presence of a microscopic bubble at each focal location on the cornea.

SHG occurs in non-centrosymmetric materials, such as the stromal collagen, while THG is strongest at interfaces between materials where there is a change in the nonlinear refractive index, such as the Bowman's Layer-Stromal boundary [25, 38, 39]. This principle was used in this study to center the FSL focus in the stroma. This also explains why observed SHG intensities were higher than observed THG intensities (see Figures 44 and 45). Further, since SHG and THG are second and third order nonlinear processes whose intensities vary with the square and cubic intensity of the incident laser [23], a weaker THG intensity would be expected
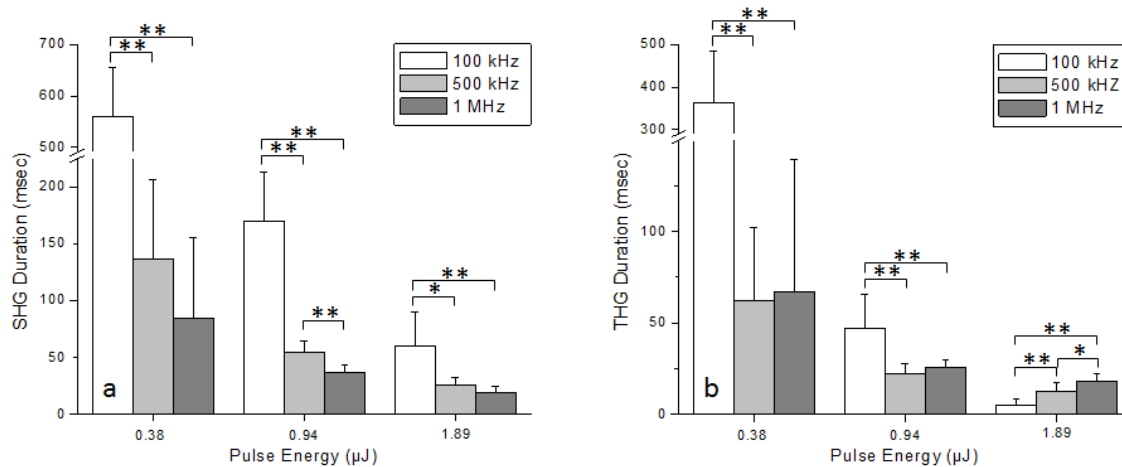
Figure 46. (a) Second-harmonic generation and (b) third-harmonic generation duration as a function of femtosecond laser pulse energy and repetition rate; *p<0.05, **p<0.01. Reprinted with permission from W. R. Calhoun, 3rd and I. K. Ilev, "Effect of therapeutic femtosecond laser pulse energy, repetition rate, and numerical aperture on laser-induced second and third harmonic generation in corneal tissue," Lasers Med Sci, Mar 17 2015. Copyright 2015, Springer Science and Business Media.

even if all other factors were equal. The increase in HG intensity observed with increasing laser pulse repetition rate at a given pulse energy can be attributed to a higher number of FSL pulses, and therefore HG pulses, within the spectrometer's integration period.

HG duration decreased with increasing repetition rate for most pulse energies (Figure 46). Shortening the period between pulses causes an increased rate of tissue destruction which shortens HG duration. Additionally, as the tissue is destroyed, more plasma absorption and scattering of HG away from the collecting fiber occurs, which further reduces HG duration. A similar explanation can be made for the decrease in HG duration observed with increasing pulse energy. Higher pulse energy results in larger plasmas with higher free electron densities that destroy more tissue per pulse [15]. In clinical therapies, FSLs are rapidly scanned to produce a tissue cutting effect. This motion limits the laser exposure at any single location to periods much shorter than both the exposure time used and the HG durations observed in this experiment.

However, since the highest HG intensity is generated instantaneously, rapid scanning of the laser constantly exposes fresh tissue which creates HG with constant peak intensity values.

Changing the NA leads to changes in beam waist at the laser focus as well as changes in the Rayleigh length related to the beam depth of focus. Normally, these changes would tend to have opposite effects on HG. For example, decreasing the beam waist results in a higher intensity and correspondingly higher HG intensity, but decreasing the Rayleigh length decreases the volume of tissue interacting with an intense optical field resulting in a decrease in HG intensity. Experimentally, a significant increase in HG intensity was observed by increasing NA (Figure 47). Previous studies using harmonic microscopy to image cornea have shown [25] that SHG signal intensity oscillates with tissue depth, with intensity peaks separated by approximately 100 μm. This effect may well be related to a varying degree of phase matching. The change in Rayleigh length associated with the tested NAs is approximately 35 μm. It is likely that since the laser focus was positioned in the stromal region by optimizing the SHG signal, extending the Rayleigh length 35 μm into low SHG efficiency stromal regions will have a
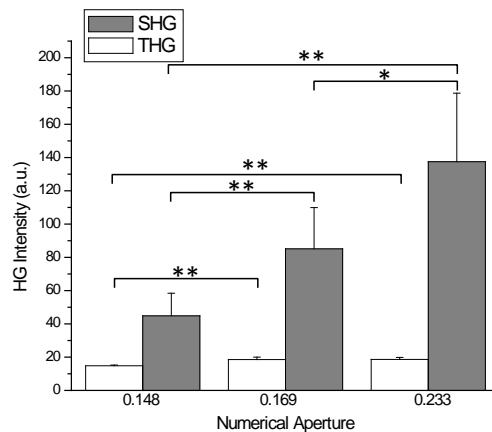
Figure 47. Second-harmonic generation and third-harmonic generation intensity as a function of numerical aperture; *p<0.05, **p<0.01. Reprinted with permission from W. R. Calhoun, 3rd and I. K. Ilev, "Effect of therapeutic femtosecond laser pulse energy, repetition rate, and numerical aperture on laser-induced second and third harmonic generation in corneal tissue," Lasers Med Sci, Mar 17 2015. Copyright 2015, Springer Science and Business Media.

small effect on the overall SHG production. Therefore, changes in the beam waist will affect HG intensity more than changes in Rayleigh length.

Although some significant increases in THG were observed with increasing NA, they were minor in comparison to SHG. Changes in THG intensity of an already weak field, in which most efficient THG occurs at the stromal interfaces, may explain the resulting small changes in THG intensity.

A large amount of variability was seen in HG which is likely a result of varying collagen orientations at different locations and depths within and across corneas [39, 40]. As previously shown, the orientation of collagen with respect to the laser polarization has a significant effect on HG efficiency. As previously noted, this is likely a result of different degrees of phase matching. Despite this variability, there were many significant differences in HG intensity and duration at all repetition rates. Many of the strongest differences occurred when comparing 1 MHz with 100 kHz repetition rates for intensity and duration measurements. The experimental groups that most closely represent current commercial therapeutic devices are (100 kHz, 0.94 µJ), (100 kHz, 1.89 µJ) and (1 MHz, 0.38 µJ) [29]. In this comparison, the 1 MHz repetition rate produced SHG intensities one and two orders of magnitude higher than the 100 kHz repetition rate at 0.94 µJ and 1.89 µJ respectively. The same comparison with respect to THG reveals no significant difference between (1 MHz, 0.94 µJ) and (100 kHz, 0.94 µJ) and a significantly higher 1 MHz THG intensity compared with (100 kHz, 1.89 µJ). Differences in SHG and THG duration were mostly not significant.

Laser parameters representing the newest generation of therapeutic FSLs may produce more intense SHG and THG than conventionally used FSLs. Since therapeutic FSLs allow the operator to adjust some of the laser parameters to customize the surgical procedure, and as both

frequencies of light generated during SHG and THG have the potential to produce damaging effects to ocular tissues, future studies that determine HG irradiance at the crystalline lens and retina are warranted to determine if a safety concern exists.

5.3 Quantitative evaluation of harmonic generation

To improve the understanding of the established relationships between FSL parameters, pulse energy and pulse repetition rate, and HG, further experiments were conducted to measure and quantitatively evaluate key HG parameters including HG intensity in absolute units and improve HG duration measurements. These measurements will extend the quantitative evaluation of HG beyond the temporal resolution limit of approximately 13.5 ms, which was determined by the temporal resolution of the spectrometer used in the previous fundamental study of the effect of critical FSL parameters on HG efficacy (Chapter 5.2) An extended quantitative evaluation of HG will greatly expand the discussion and analysis of the safety of HG generated in the eye and provide a better understanding of HG in therapeutic conditions.

5.3.1 Materials and methods

For improving SHG duration measurements, the addition of a photodiode to the previous setup was accomplished using a 1 × 2 fiber bundle (Figure 48(a)). This allowed simultaneous temporal and corresponding spectral data to be collected. The photodiode had a temporal resolution of 2 μs and was connected to the computer using a PC interface. Further, instead of measuring the duration of the SHG signal above a threshold set slightly above the noise level, the threshold was set to the SHG plateau level following the initial peak decay.

   For recording SHG in absolute units, a different photodiode (PD-300-UV, Ophir) was placed directly below the sample and the fiber and spectrometer were eliminated from the setup
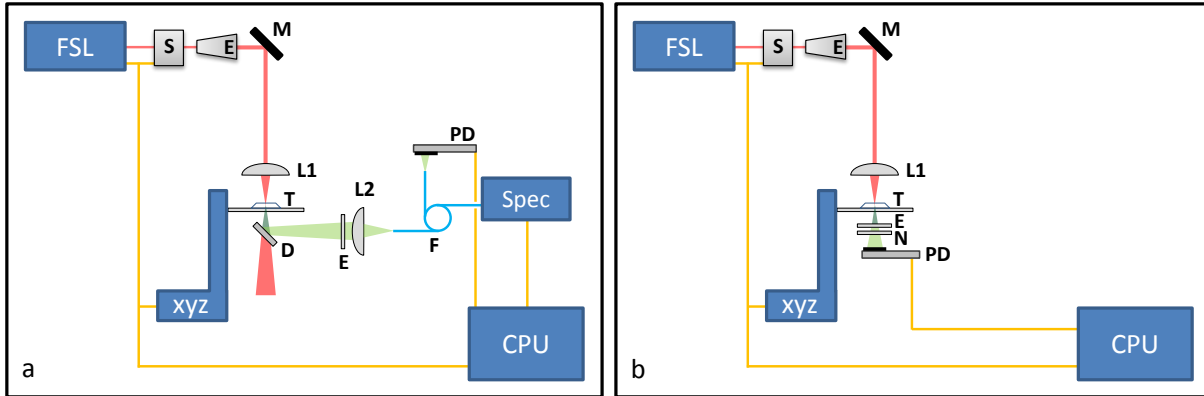
Figure 49. Principle optical experimental setup for measuring tissue (T) (a) second-harmonic generation intensity and duration of multiple pulses and (b) second-harmonic generation pulse energy and conversion efficiency of single pulses with respect to femtosecond laser (FSL) pulse energy using computer-controlled (CPU) translation stage (XYZ), laser and shutter (S). E beam expander; M mirror; L1, L2 lens; D dichroic beam splitter; SP short-pass filter; E edge-pass filter; N notch filter; PD photodiode sensor; F fiber; Spec spectrometer.

(Figure 48(b)). A short-pass, edge filter and a notch filter (Figure 49) were positioned immediately in front of the photodiode sensor to eliminate all power at the fundamental FSL wavelength.

Similar to the previous experiment, all combinations of 3 pulse energies (460 nJ, 800 nJ and 1.15 μJ) and 3 repetition rates (100 kHz, 500, kHz and 1 MHz) were tested using 4 locations for each laser parameter combination on each of 5 bovine corneas. The same laser and focusing lens (NA = 0.233) were used and general procedures were followed as described for the previous
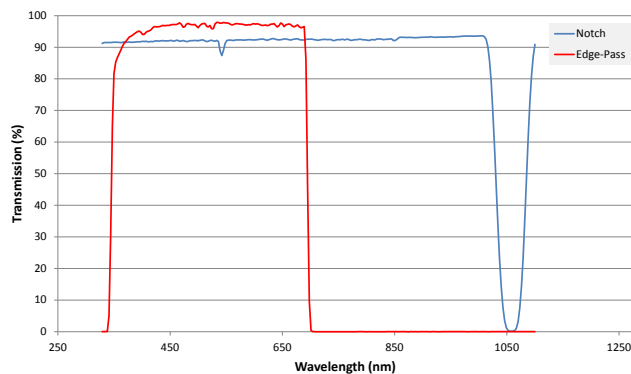
Figure 48. Spectral transmission measurement of optical filters used in optical experimental setups.

experiment (Chapter 5.2).

5.3.2 Results

As expected, the SHG power, measured for this similar set of FSL parameters, shows the same trends and reinforces previous experiments. The power of SHG ranged from values as low as 10 µW in the case of laser parameter combination (100 kHz, 460 nJ) to over 3 mW with laser parameter combination (1 MHz, 1.15 µJ) (Figure 50). Increasing pulse repetition rate or pulse energy increased SHG power.

With improved temporal resolution, the time duration of the initial peak in HG intensity is much shorter than previously measured for high pulse repetitions rates and pulse energies. Peak durations ranged from 7 ms to 500 ms, the duration of laser exposure (Figure 51). Using the laser parameter combination (100 kHz, 400 nJ) the initial peak intensity lasted the entire duration of the laser exposure in all samples. In contrast, the combination (1 MHz, 1.15 µJ) generated the shortest peak duration. Increasing pulse energy or repetition rate led to significantly decreased peak durations in most cases.
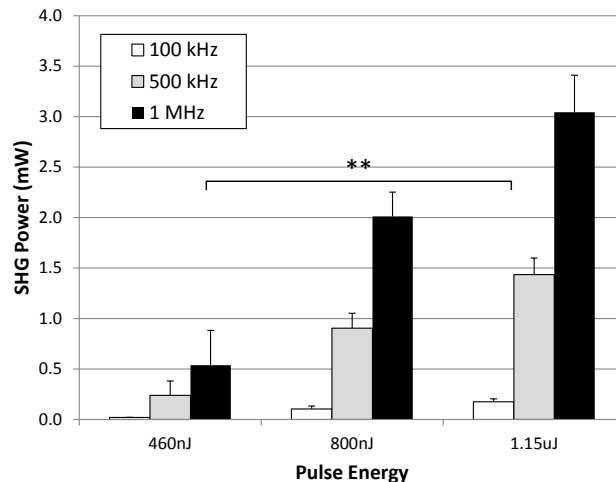
Figure 50. Average absolute second-harmonic generation power measurements with respect to femtosecond laser pulse energy and repetition rate; **p<0.001.

100
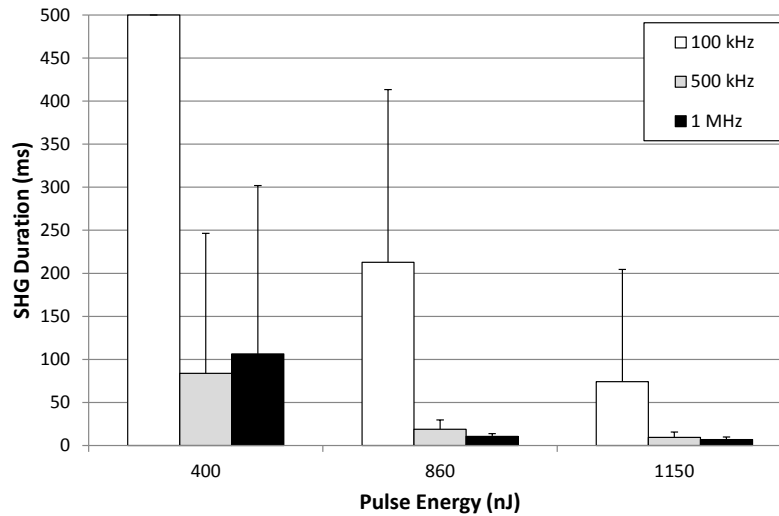
Figure 51. Average second-harmonic generation peak duration measurements with respect to femtosecond laser pulse energy and repetition rate.

5.3.3 Discussion

The improved measurements of SHG power and duration have not only provided absolute measurements of SHG and more accurate SHG duration measurements, but also improved the understanding of the dynamic behavior of clinically relevant FSL-induced HG in corneal tissue.

Previous HG durations measured using a high-speed spectrometer were unable to measure the true brevity of the initial peak in HG intensity and also averaged smaller and broader peaks into the much larger HG signal (i.e. Figure 52).

The results of this study demonstrate a dynamic, but repeatable, behavior to the HG signal. Initially, a strong peak in SHG occurs upon laser irradiation which quickly decays to a more stable level before eventually decreasing to near zero levels (Figure 52). The following interpretation of this behavior is formed by the well documented, and previously discussed, affect LIB has on the surrounding tissue. Since LIB is a threshold event that occurs at much higher optical field intensities than HG, the tissue source of the SHG signal extends beyond the
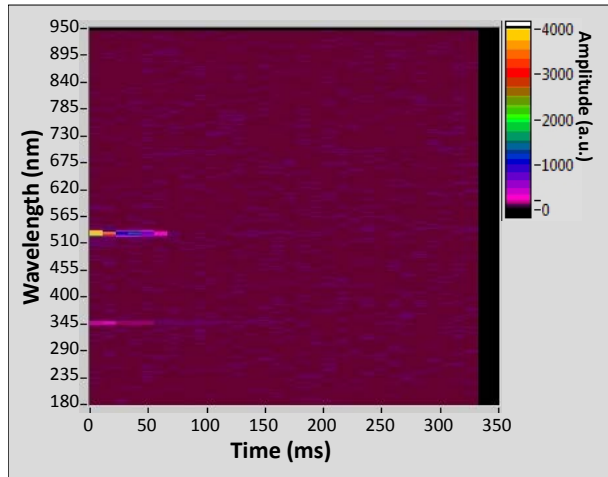
Figure 52. Typical spectral recording of harmonic generation using high femtosecond laser pulse energy and repetition rate. An initial intensity peak followed by plateau that eventually decays can be seen.

volume of tissue that is quickly destroyed by LIB. SHG occurs most intensely at the beam waist before multiphoton ionization and ensuing avalanche ionization generate a large concentration of free electrons (Figure 53, t_1). As the pulse increases in intensity, HG increases, but so does plasma generated at the beam waist as part of the LIB process (Figure 53, t_2), which then destroys the tissue architecture responsible for strongest HG. Plasma absorbs and, to a lesser extent, scatters incident light allowing only a small fraction to transmit [150], decreasing SHG transmission. This instantaneous SHG peak, occurring in the first fraction of the laser pulse, was not resolved in this study, as this would require temporal resolution on the femtosecond regime. Nearing the end of the FSL pulse, HG decreases with pulse intensity and the plasma has generated a cavitation bubble (Figure 53, t_3) that will further attenuate HG generated during subsequent pulses. During a single pulse, the zone of thermal damage is insignificant, less than 1 µm [151], but after many pulses, this zone will increase the volume of tissue destruction (Figure 53, t_4). This seems to be responsible for the initial decay in SHG signal seen in the data. After even more pulses, linear absorption of the NIR energy becomes significant as heat accumulates
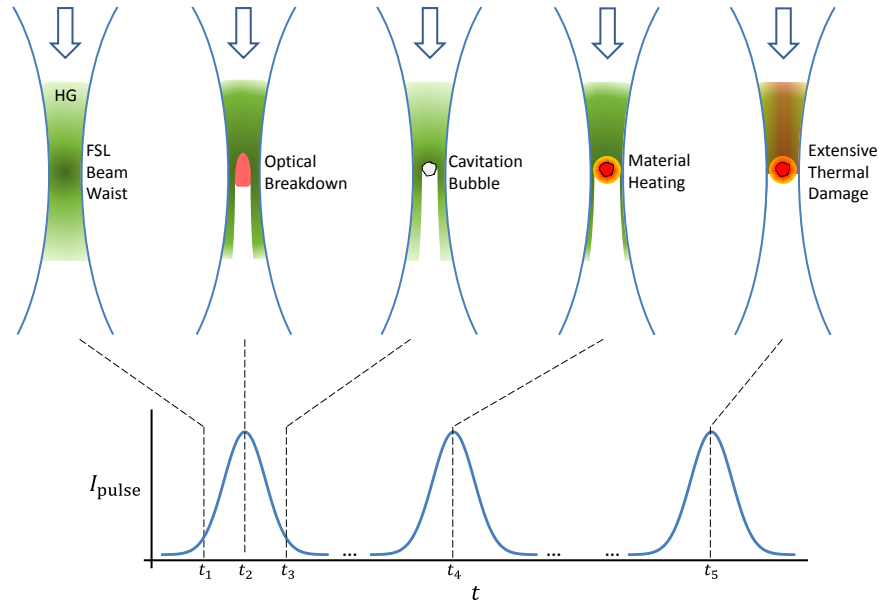
Figure 53. Temporal behavior of harmonic generation governed by laser-induce breakdown effects on tissue.

and thermal degradation of tissue occurs, well below the ablation threshold (Figure 53, t_5) [103]. This delayed tissue damage mechanism is likely responsible for the final decay in SHG seen in the data.

Similar to previous findings, the laser parameter pairs representing conventional FSLs (100 kHz, 1.15 μJ) and the emerging FSL class (1 MHz, 40 nJ) show a significant difference in power, with the latter producing more than 2.5 times higher SHG power. Although the emerging FSL class also produced SHG durations 44% longer than the conventional FSL, this difference wasn't statistically significant. The results confirmed the previous finding that SHG power increases with laser pulse repetition rate and pulse energy.

An important finding, confirmed with the improved temporal resolution of this study, is the presence of strong SHG produced after the initial FSL pulses. This implies that the maximum SHG peak power preceding and during the first pulses was at least as powerful as those found in the study. The safety implications of these values will be explored in the following Chapter.

5.4 Effect of femtosecond laser parameters on single pulse harmonic generation energy and efficiency

In ophthalmic procedures, single laser pulses are deposited at each location, separated by a few micrometers. This allows the photodisruptive effect to be as precise as possible with minimal collateral tissue damage. In this technique, there will be negligible heat transfer from the plasma volume to surrounding tissues [151, 152] and linear absorption leading to thermal destruction can be disregarded.

HG in collagenous tissues induced by focused Gaussian beams has been described using a phased array antenna model (Figure 54) in the majority of related studies [82, 153-155]. In this model, the total HG exiting a specific volume of tissue is described as the summation of contributions from smaller tissue segments (dz'). In the case of a focused laser, the focal volume ellipse can be approximated using the following Equations:

$$w_{x,y} = \frac{0.32\lambda_\omega}{n_\omega \sin\theta} \quad \text{and} \quad w_z = \frac{0.53\lambda_\omega}{n_\omega(1-\cos\theta)}, \qquad \text{(41) and (42)}$$

where, $w_{x,y}$ and w_z are the focal ellipse radii in the *x-y* and *z* directions respectively and θ is the laser focus half angle. Using these Equations and appropriate values from these experimental procedures, the focal volume ellipse is approximately 40 µm long (in the *z*-direction) and 3 µm wide (in the transverse direction). As corneal lamellae are typically 5-9 µm thick, a number of
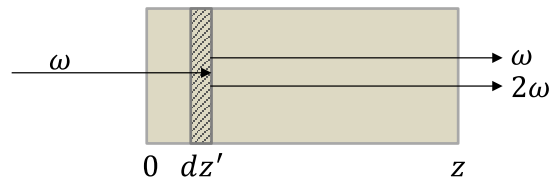
Figure 54. Antenna model of second-harmonic generation.

104

regions, each producing similar HG, will be encountered in the focal ellipse. This sequence of laser tissue interactions coordinates well with the antenna model.

As previously shown and discussed, the HG power will be highest during the first laser pulse and decrease with subsequent pulses as the tissue is degraded. It is important then to know the HG power generated by a single laser pulse. With this information conclusions regarding safety that are directly applicable to current surgical devices and related procedures can be formed.

An important parameter related to HG is efficiency (η_{HG}), determined by the following Equation:

$$\eta_{\text{SHG}} = \frac{E_{\text{pulse},2\omega}}{E_{\text{pulse},\omega}}, \tag{43}$$

where, $E_{pulse,\omega}$ and $E_{pulse,2\omega}$ are the pulse energy of the input pulse at the fundamental frequency and the induced, second harmonic pulse. HG in crystals with uniform structure and the ability to precisely phase-match via crystal rotation or thermal control, or use a quasi-phase-matched technique, can achieve efficiencies greater than 50 percent in a single-pass interaction [156, 157]. Conversion efficiency can approach and surpass 100% when using multi-pass techniques or incorporating nonlinear materials into a resonant cavity. In corneal tissue, the collagen structure is well organized by tissue standards, but is far from ideal as a nonlinear material. As previously shown, corneal rotation, in an attempt to decrease the phase mismatch, has a very minor effect on SHG. As there is no robust method to reduce the phase-mismatch, low efficiencies are likely.

No previous studies have measured SHG pulse energy or the conversion efficiency in corneal tissue using clinically relevant FSL parameters. Several studies have formulated predictions regarding how collagen fibril size and spacing will affect relative conversion

efficiency and emission direction [83, 131, 154]. Other groups have modeled, and in some cases measured, the effect of varying polarization, NA and the fundamental wavelength on relative SHG power [84, 128]. Most studies assume a single collagen fibril orientation and some include the presence of significant tissue scattering. In the case of ophthalmic clinical applications of FSLs, several fibril orientations need to be considered and very low scattering is present. As HG will be generated over several lamellar orientations throughout the laser focal volume, the resulting HG efficiency will be an average of the specific efficiencies associated with each lamellar-laser interaction.

In this study, the absolute SHG pulse energy and effective SHG conversion efficiency induced in corneal tissue using clinical therapeutic FSL settings was determined. This will provide valuable metrics for comparing clinical procedures with safety standards as well as predicting HG produced by laser parameters not specifically tested.

5.4.1 Material and methods

As in previous work (Chapter 5.2), fresh bovine corneas were trephined immediately prior to testing using a 10-mm punch. Only clear, healthy appearing corneas were used. The corneal button was placed on a glass microscope slide with a drop of BSS to prevent desiccation. To measure the HG energy produced from a single FSL pulse, the same setup was used from the previously discussed SHG power measurement study (Figure 48(b)). The FSL was focused with a numerical aperture of 0.233, the same as in previous studies, into the mid-stroma by optimizing the SHG signal at low power to avoid tissue damage.

Three FSL pulse energies were tested (548 nJ, 1.37 µJ, 2.19 µJ). Each pulse energy was tested at 10 locations on each of 3 corneas, with 2.19 µJ tested at 20 locations on one of the three

corneas, for a total of 40 measurements at that energy level. All measurements were averaged for each pulse energy and used to calculate HG conversion efficiency.

Prior to absolute SHG pulse measurements, corneal transmitted light was characterized with a spectrometer to ensure that only SHG was being measured.

5.4.2 Results

The average energy of the harmonic pulse produced for each of the three FSL pulse energies are summarized in Figure 55. All means were significantly different showing increased SHG pulse energy with increasing FSL pulse energy. SHG pulse energy values approached 1 nJ. Despite the increasing trend in SHG pulse energy, the SHG conversion efficiency, summarized in Figure 56, decreased with increase FSL pulse energy. Conversion efficiencies were the greatest for the 548 nJ FSL pulses at approximately 0.08 %.

5.4.3 Discussion

The results of these single pulse measurements demonstrate contradicting effects. Increasing the pulse energy of the FSL (at the fundamental frequency) should also increase the pulse energy of the generated harmonics as well as the conversion efficiency. This is due to the quadratic
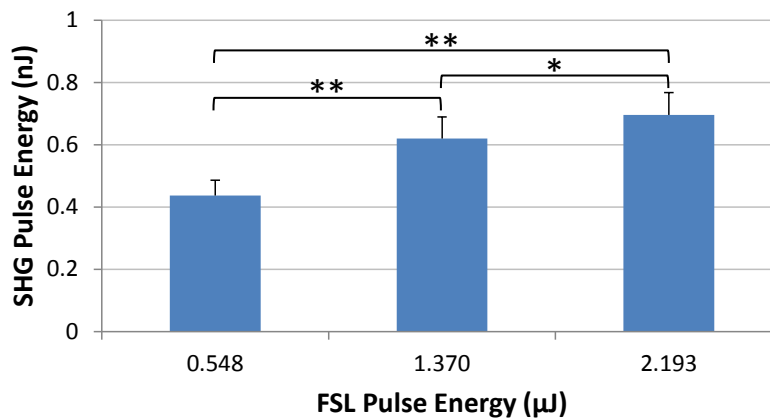
Figure 55. Average second-harmonic generation pulse energy measurements with respect to femtosecond laser pulse energy; *p<0.01, **p<0.001.
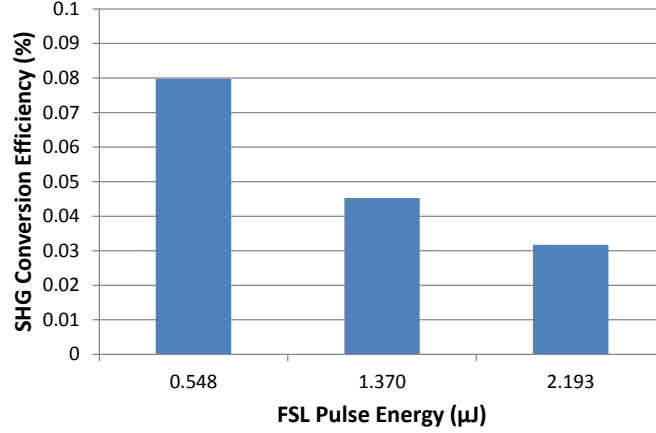
Figure 56. Average second-harmonic generation conversion efficiency with respect to femtosecond laser pulse energy.

relationship between the fundamental and second harmonic field strengths. Although the results do show an increase in HG pulse energy, it isn't proportional to the increase in pulse energy at the fundamental frequency. This is shown by the overall decrease in HG conversion efficiency.

The explanation for this contradiction, which correlates with the previous findings, is due to the competing NOE's, LIB and HG. As LIB destroys the tissue in the laser focal volume, HG cannot occur in the same volume. If tissue destruction occurs earlier in the pulse lifetime, HG will therefore generate less energy during the pulse and result in a lower efficiency since the pulse energy at the fundamental frequency remains the same. To understand the relationship between HG pulse energy and the occurrence of LIB, the rate equation most commonly used to describe the evolution of the volumetric density of free electrons (ρ) due to FSL irradiation should be considered [103, 105, 158-160]:

$$\frac{d\rho}{dt} = \eta_{\mathrm{mp}} + \eta_{\mathrm{casc}}\rho - g\rho - \eta_{\mathrm{rec}}\rho^2,\tag{44}$$

where, $\eta_{\mathrm{mp}}$and η_{casc} are the rate of free electrons produced by multiphoton absorption and cascade ionization, respectively. η_{rec} and g are the rate of free electron recombination and diffusion from the focal region, respectively. The dominant contributor to free electrons is

cascade ionization, which also generates free electrons significantly faster than multiphoton absorption due to its exponential growth characteristics. In the case of FSL pulse durations in corneal tissue, multiphoton absorption is the primary source of seed electrons necessary for cascade ionization. The multiphoton ionization rate depends solely on irradiance and is the rate limiting step in LIB [160]. Therefore, increasing the pulse energy of the fundamental frequency will allow significant cascade ionization to occur earlier in the pulse lifetime [103, 160, 161]. This explanation is also supported by previous results measuring the HG lifetime during multiple FSL pulses. When the laser pulse energy was increased, HG lifetime decreased.

If it is assumed that the HG pulse duration is comparable to the principal, FSL pulse, the peak power of the HG pulse can be estimated (Figure 57). The HG peak power increases with pulse energy from approximately 1.5 kW to over 2 kW. The true peak power is likely higher than these values as the majority of energy at the second harmonic frequency is generated over a time period shorter than the pulse width of the fundamental frequency due to the exponential relationship between the fundamental and second harmonic field intensities. Furthermore, as bulk HG is halted at some fraction of the principal pulse duration, due to LIB, the actual time
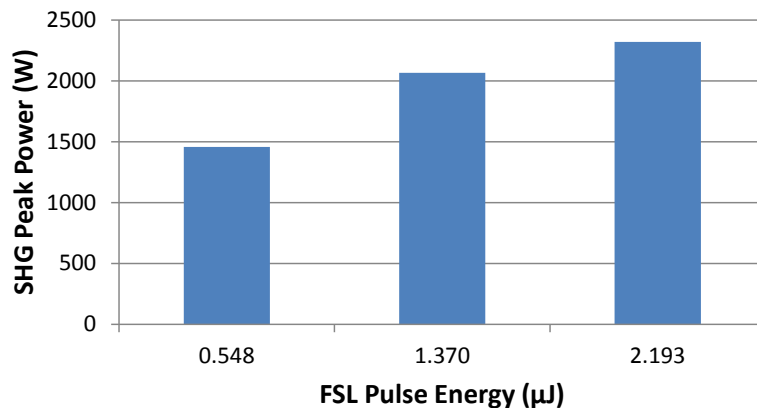
Figure 57. Average second-harmonic generation peak power with respect to femtosecond laser pulse energy.

during which the majority of energy is generated is even shorter.

Considering that current therapeutic FSLs typically have a range of pulse energies that can be selected by the user, it is important to consider the secondary effect of choosing specific pulse energies. A more complete discussion of safety consideration will follow in the next Chapter.

Chapter 6 – Safety Implications and Conclusions

6.1 Harmonic Generation and Safety

Parallel to the development of lasers for a broad range of purposes, laser safety has also advanced. Ophthalmic surgical procedures utilize FSLs with intensities three orders of magnitude higher than intensities used for imaging applications [55]. In addition, unlike fluorescence, HG is a coherent process, resulting in more intense light and therefore, more capable of causing unintended tissue damage. Damage to biological tissues can occur through photochemical, photomechanical and photothermal mechanisms. This safety evaluation will consider possible harmful effects caused by the second and third harmonic frequencies of clinical therapeutic lasers through photochemical and photothermal mechanisms. HG in clinical therapeutic scenarios does not generate nearly enough energy to cause any type of photomechanical effects. Photochemical damage generally is related to radiant exposure, a cumulative measure, since damage can occur over an elongated period of time. Photothermal injury is related to irradiance, as the temporal deposit of energy is critical with respect to the buildup of heat. The safety of the fundamental FSL frequency has been relatively well documented both in the literature and as part of the U.S. FDA device approval process. However, neither the literature nor the FDA review process has properly considered HG with respect to patient safety, and no proper analysis of HG occurring during clinical therapeutics has been performed.

Presently, there are several standards that govern laser safety and provide information regarding safe laser use. Table 5 summarizes the related standards. Conformation to these standards may be obligatory or voluntary depending on local regulation. Maximum permissible exposures (MPEs) are prescribed for different laser and exposure parameters, above which, the risk of injury is significant. These MPEs are chosen based on damage thresholds determined from experimental studies and incorporate a safety factor to further safeguard against injury. Damage thresholds are typically defined as a certain radiant exposure or irradiance, given a certain set of laser parameters and exposure characteristics, which causes tissue damage 50% of the time. The MPEs found in the ANSI and ISO standards most closely relate to ophthalmic therapeutic exposures.

Table 5. Relevant ocular safety standards.

Standard	Comment
US 21 CFR 1040.10	US mandatory standard applicable to manufacturers. Classifies laser products & specifies testing and performance requirements.
US 21 CFR 1040.11 (a)	US mandatory standard applicable to manufacturers. Specifies additional or modified requirements to CFR 1040.10 for medical laser products.
ANSI Z136.1 (2014)	US voluntary standard provides guidance for the safe use of lasers and laser systems. It is the basis for the ANSI laser standards.
IEC 60825-1 (2014)	Safety of laser products, International Electrotechnical Commission, 2007. The standard is a 3 part standard. Two parts have requirements and specifications similar to CFR 1040.10. Standard is mandatory in countries that adopt it. Third part is informative and includes tables and MPEs. Countries can adopt all or only parts of the standard.
ISO 15004-2 (2007)	International standard for fundamental requirements and test methods regarding light hazard protection in ophthalmic instruments.

In order to ensure safety, it is necessary that individual pulses do not exceed the appropriate MPE. In addition, since clinical FSLs employ very high pulse repetition rates, where cumulative effects need to be considered, it is necessary to ensure that the average exposure of a pulse train does not exceed the appropriate MPE for a single pulse with the same duration as the pulse train. This scenario can be applied to a region of tissue over which the laser is scanned, or

in the case of a scan failure and the laser focus remains in one location. It is also necessary to consider three critical tissues: cornea, crystalline lens, and retina. With approximately perpendicular laser incidence, weak scattering of harmonic frequencies excludes damage to collateral tissues.

6.1.1 Corneal hazard analysis

As the cornea is virtually transparent to visible wavelengths (Figure 14), SHG won't cause any damage at these already low levels, and therefore this analysis will consider only THG. Ocular exposures usually result in much higher irradiances at the retinal plane than at the cornea. As such, most exposure guidelines do not prescribe MPEs for preventing corneal damage. Instead, worst case scenarios may be compared with published corneal and endothelial damage thresholds at the appropriate wavelength. The literature reports values for endothelial damage threshold at 347 nm ranging from approximately 7.2 J/cm^2 to 60 J/cm^2 [162-166]. Some of the variation can be explained by differences in experimental procedures, specific wavelengths tested and endpoints used.

Three cases should be considered that would serve as worst-case scenarios with respect to corneal endothelial exposure:

(1) A single pulse exposure with the laser focus 50 μm anterior to the endothelium, the deepest corneal procedure that intends to preserve the underlying endothelial cells, using a low NA.

(2) An anomalous exposure in which laser scanning fails and the laser focus resides in a location 50 μm anterior to the endothelium for a prolonged period of time, using a low NA.

(3) A prolonged exposure as the laser focus is scanned to create an 8-mm diameter planar cut in the stroma, 50 μm anterior to the endothelium, using a low NA.

In the single pulse scenario (case (1)), using conservative values for THG pulse energy, using experimental measurements, and low NA, the resulting radiant exposure at the endothelial plane is four orders of magnitude below the lowest reported injury threshold values. Even considering that the spot size of the THG is likely smaller than that of the fundamental frequency due to HG occurring over an area smaller than the beam waist, the radiant exposure remains substantially below injury threshold values.

During a scan failure (case (2)), the radiant exposure would increase with each pulse. Most therapeutic lasers have safety shutters that will interrupt the laser in this event. If a typical pulse repetition rate is assumed (150 kHz), the lowest damage thresholds will be exceeded after approximately 80 ms. However, it is important to consider the previously described rapid decay in HG with subsequent pulses. This will have the effect of extending the safe period of a stationary focus. However, if a higher pulse repetition rate (65 MHz) is considered, accompanied by a correspondingly lower THG pulse energy, the damage threshold will be exceeded in about 600 μs. Once again, the spot size of the THG is likely smaller than that of the fundamental frequency which would serve to shorter the estimated time period. Conversely, the effect of reduced harmonic energy with successive pulses would serve to elongate the estimated time period. Nonetheless, the effect of the higher pulse repetition rates can be seen. These higher repetition rates have not yet been seen in clinically approved devices, but are commonly used in research settings. Given the clinical historical trend and a stronger desire for faster and more accurate procedures, it is likely that these repetition rates will be seen in clinical practice in the future.

Finally, for a scanning exposure (case (3)), the THG pulse intensity will remain high for every pulse as each is deposited into virgin tissue. Assuming a typical 8-mm diameter planar cut, with the same proximity to the endothelium, a pulse repetition rate of 150 kHz and total exposure duration of 20 s (values typical for current LASIK procedures), the resulting radiant exposure of approximately 2.9 mJ/cm^2 remains significantly below reported injury thresholds, but very close to the MPE (ISO 15004-2) of 3 mJ/cm^2. If a higher pulse repetition rate is assumed (65 MHz) with corresponding pulse energy, the radiant exposure grows to 350 mJ/cm^2, two orders of magnitude greater than the MPE, but still below reported damage thresholds. However, small variations in laser parameters or procedure duration could potentially increase the radiant exposure to dangerous levels.

The conclusion that THG induced during commonly performed LASIK and keratoplasty surgeries is safe is supported by studies that examine endothelial cell health post FSL treatment [48, 167] and intrinsically by receiving FDA approval. However, studies examining endothelial cell health following procedures such as deep anterior lamellar keratoplasty (ALK), Descemet's membrane endothelial keratoplasty (DMEK) and Descemet's stripping automated endothelial keratoplasty (DSAEK), which involve positioning the FSL focus in closer proximity to the endothelium ($\leq$ 100 μm), have shown increased endothelial cell injury [41, 168]. Generating mechanical perturbation, including ultrasonic transient waves, in close proximity to this sensitive cell layer may be responsible for the observed endothelial injury. Nevertheless, these procedures typically require higher pulse energies to combat increased scattering at these corneal depths, which could generate higher THG pulse energies. Since no studies have identified the injury mechanism in these cases and FSLs have not yet received approval for these off-label uses,

future studies investigating photochemical endothelial damage thresholds in these circumstances should be performed.

6.1.2 Crystalline lens hazard analysis

The second critical tissue to consider in the light propagation pathway to the retina is the crystalline lens. Harmonic frequencies generated in the cornea pass into the crystalline lens which is most sensitive to damage by UV radiation, a major risk factor in cataract formation [169]. Typically, the cornea absorbs as much as 50% of incident UVA light. Cataract is a cumulative disease in which structural protein, crystallins, are modified posttranslationally by non-enzymatic glycation and other biochemical and biophysical processes including photooxidation [170, 171] resulting in the formation of chromophores and protein aggregation that increases light absorption and scattering, respectively, over time. THG produces coherent UVA light that is almost completely absorbed by the lens [166]. Significant UVA absorption can damage the lens by inducing damage to lens epithelial cell membrane lipids, cytoskeletal elements and the antioxidant enzyme catalase, and induce oxidation as well as other cell disruptive effects that lead to cataract formation. NADPH and 3-hydroxykynurenine have been identified as major chromophores in the lens with maximum absorption peaks at 355 nm and 365 nm respectively [169, 172-174].

Several studies have established damage thresholds with respect to cataract formation in the crystalline lens [79, 166, 175, 176], with the most recent and reliable one identifying this threshold to be about 92 J/cm^2 at the third harmonic frequency. The endpoint of these studies was a visible lesion within a short period of time, less than 36 hours. This endpoint is quite different than the typical cumulative nature of cataract formation, and as such, damage to the lens occurs on a much smaller scale at significantly lower values. Alternatively, these studies do

116

provide a good sense of the action spectra for lens tissue. In a smaller scale study, 3 J /cm^2 was required to interfere with lens epithelial cell functions.

The following cases should be considered as worst-case scenarios with respect to lens exposure:

(1) A single pulse exposure with the laser focus at the corneal endothelial plane – the shortest distance to the lens where THG will be produced – using a low NA.

(2) An anomalous exposure in which laser scanning fails and the laser focus resides at the endothelial plane for a prolonged period of time, using a low NA.

(3) A prolonged exposure as the laser focus is scanned to create a planar cut in the stroma, 50 μm anterior to the endothelium – the shortest distance to the lens for a planar cut to be made – using a low NA.

For a single pulse deposited at the endothelium (case (1)), which is conservatively 3 mm from the lens, using a NA of 0.1, the resulting radiant exposure would be less than 100 nJ/cm^2, orders of magnitude less than the lowest reported damage threshold and the MPE of 3 mJ/cm^2. This estimate ignores losses provided by the remaining 50 μm of stroma, cornea-aqueous interphase, and 3 mm of aqueous.

In the event of a scan failure (case(2)), the 3 mJ/cm^2 MPE would be reached in about 140 ms. If a higher pulse repetition rate is considered once again (65 MHz), the MPE is reached in only 1.1 ms. These estimations are assuming a 15% loss during propagation to the lens [177].

During scanning procedures (case(3)), the illuminated area of the lens is slightly larger than the scanned area in the posterior stroma due to the beam divergence and 3 mm distance separating the lens from the cornea. For an 8-mm diameter cut in the posterior stroma, requiring 20 s, the radiant exposure for the lens is 2.2 mJ/cm^2. This is slightly below the 3 mJ/cm^2 MPE. If

117

the same procedure using an FSL with a higher pulse repetition rate (65 MHz) is again considered, the radiant exposure becomes approximately 260 mJ/cm^2, almost 2 orders of magnitude above the MPE for photochemical lenticular damage. Again, this is assuming a 15% loss during propagation to the lens.

Lenticular damage may be the most difficult to gauge. Although these values are near or above the MPE, they are below the damage thresholds seen in the literature. The point at which UV exposure begins to generate cumulative changes that contribute to and accelerate cataract formation is and may continue to be difficult to identify. The most important finding from this analysis maybe that UVA radiation, at wavelengths known to contribute to cataractogensis, is being generated in significant quantities during FSL-based ophthalmic procedures. This will be an important occurrence to consider as FSLs and ophthalmic procedures evolve. The use of FSL based procedures while a patient is using a drug that has photo-sensitizing effects is even more important to consider in these situations.

6.1.3 Retina hazard analysis

The retina is most sensitive to light in the 400 nm to 550 nm range. Excessive absorption at these wavelengths can cause oxidative damage that may cause diminished vision known as photoretinitis. The retina may be further sensitized by the use of a number of drugs [67, 174, 178]. SHG induced by therapeutic FSLs produces light in the short wavelength visible region most dangerous to the retina. The cornea, aqueous humor, lens and vitreous humor are transparent to these wavelengths allowing almost 100% of the energy to propagate to the retina. The same pathway only allows a small percentage of THG that also occurs to reach the retina. As such, this analysis will only consider the effects of SHG on the retina.

The following cases should be considered as worst-case scenarios with respect to retinal exposure:

(1) A single pulse exposure with the laser focus at the centered on the eye and located near the corneal endothelia-aqueous interface, using a low NA.

(2) An anomalous exposure in which laser scanning fails and the laser focus resides at the same location described for a single pulse exposure for a period of time, using a low NA.

(3) A prolonged exposure as the laser focus is scanned to create a planar cut in the stroma, 50 μm anterior to the endothelium, using a low NA.

For a single pulse (case(1)), photochemical damage is disregarded since the amount of energy delivered in such a short pulse isn't nearly enough to elicit a significant cellular response. Appropriately, there are no MPE's for photochemical damage for ultrashort pulse durations. The photothermal MPE (ANSI) for retinal exposure to a single pulse at 521 nm is 1.33×10^{-4} J/cm^2. Using the minimal spot size that could be created on the retina given the focal position and numerical aperture, 1.69 mm diameter, the radiant exposure of a single pulse of SHG would be 3.12×10^{-8} J/cm^2. Clearly, a single pulse doesn't introduce a photothermal threat.

For longer exposures in the case of a scanning failure (case (2)), the photothermal MPE becomes dependent on the exposure duration. Figure 58 shows the MPE as well as the radiant exposure generated during a scan failure. It can be seen that at both pulse repetition frequencies the radiant exposure remains well below the MPE for all exposure durations up to approximately 18 s for the 65 MHz repetition rate. This is due to the fact that the thermal confinement time for pulse energies of this magnitude is less than the period between pulses. Although providing a shutter response within 18 s of a scan failure is easily achieved, this is an important safety
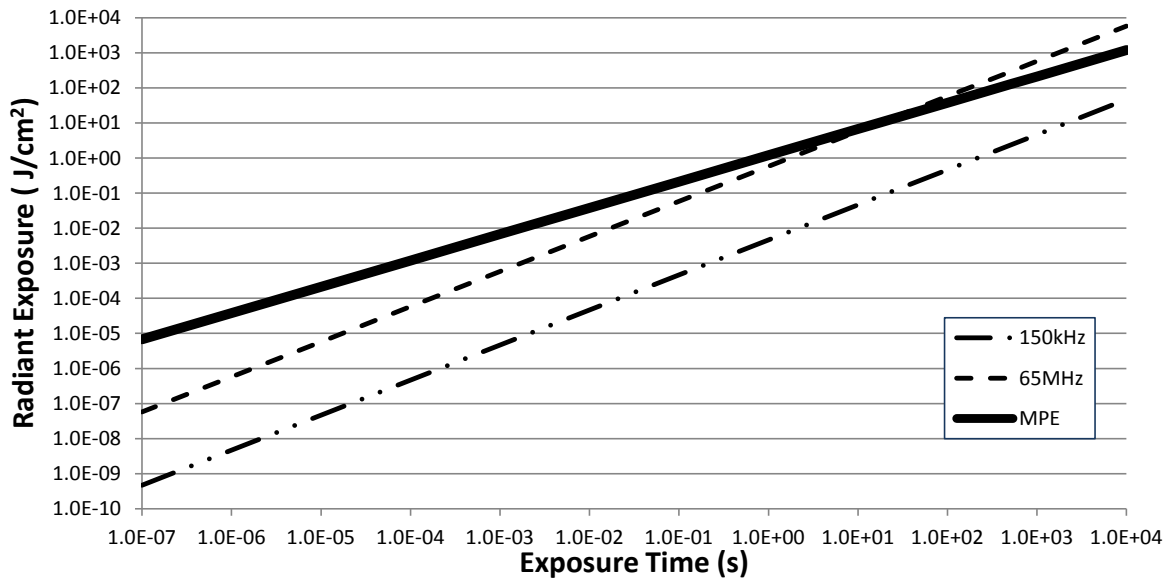
Figure 58. Maximum permissible exposure and estimated exposure caused by second-harmonic generation with respect to retina photothermal injury.

consideration as technology and ophthalmic procedures continue to evolve where shutter response time may become more relevant to retinal damage.

The photochemical hazard also needs to be considered for multiple pulses during a scan failure exposure. The exposure times required to reach both ISO and ANSI MPE's for retinal photochemical damage are very similar and significantly longer than any realistic exposure time, on the order of hours.

Finally, the total exposure during a scanning planar cut should be considered (case (3)). Assuming an 8-mm planar cut in the posterior stroma requiring 20 s, a 150 kHz pulse repetition rate would result in a radiant exposure of approximately 0.2 mJ/cm^2 and a 65 MHz repetition rate would result in an approximate radiant exposure of 18 mJ/cm^2. These are both significantly less than the ISO and ANSI prescribed guidelines, which are in good agreement themselves at 10 J/cm^2 and 10.5 J/cm^2.

6.2 Safety conclusions

A review of HG during selected worst-case scenarios that may occur during ophthalmic, FSL-based procedures sheds light on a previously unexamined yet important topic which will inevitably grow as FSLs continue to introduce new therapeutic solutions and improve numerous medical procedures. A hazard analysis was performed for the corneal endothelium, crystalline lens, and retina, for FSL based corneal incisions and planar cuts performed in LASIK, keratoplasty and other procedures involve stromal incisions. Laser and procedure parameters were chosen to closely represent currently performed therapeutic procedures as well as future ones.

It is apparent from the large separation between estimated radiant exposures and reported damage thresholds and standard MPEs that individual SHG and THG pulses do not pose a threat to any of the mentioned tissues when using pulse energies of the therapeutic (fundamental) wavelength below several microjoules. As SHG and THG pulse energies are in the sub-nanojoule range, cumulative photochemical and photothermal effects are more important to consider. In particular, during a laser scan failure, currently used pulse repetition rates demonstrate the importance of a safety shutter response in less than 200 ms to maintain exposures below standard MPE. If higher repetition rates are used in future devices and procedures, estimations show response times may need to be in the sub-ms range. Cumulative effects of a planar stromal cut over a 20 s time period using current pulse repetition rates generates radiant exposures below, but in the vicinity of, MPEs for the anterior segment tissues. Using higher repetition rates, slightly longer exposures, and/or higher pulse energies may very well cause the MPE to be exceeded. Due to the beam divergence, retinal cumulative radiant exposures were substantially below MPEs.

These findings should also be considered as clinical lasers continue to evolve and operate with different laser parameter values that weren't tested, including different fundamental wavelengths. Slightly shorter near-IR fundamental wavelengths will generate SHG and THG at more damaging wavelengths closer to the retinal blue-light hazard and higher energy UV photons. As new therapeutic procedures are developed that feature the photodisruptive effect of FSLs for larger tissue manipulations requiring longer exposures, cumulative effects will be very important. Changes to the corneal structure also need to be considered. FSL based refractive surgery following corneal crosslinking (a very plausible scenario) may result in much more intense HG that could possibly be damaging.

6.3 Summary of findings

The studies conducted as part of this dissertation, which is focused on improving the understanding of therapeutic, FSL-induced HG in corneal tissue, have generated many important findings that will improve future procedures, safe guard against ocular damage, and possibly lead to new applications exploiting HG in this important tissue, as well as others. The findings resulting from these studies can be summarized in several major directions.

(1) Investigation of critical corneal tissue properties affecting HG:

- Evaluated broadband UV, visible and near-IR spectral transmission characteristics of human and bovine corneal tissues.

- Assessed cornea birefringent effects using a novel, experimentally and theoretically validated FSL-based test methodology that revealed significant inter- and intra- corneal variation.

- Evaluated SHG and THG throughout the corneal thickness which revealed depth specific HG effects.

- Investigated the effect that the relationship between collagen orientation with respect to FSL polarization has on SHG. The results showed that BPM had only a minor contribution to SHG while QPM occurring in the posterior stroma had a larger impact.

- Investigated the effect that collagen crosslinking has on SHG and THG. The results showed that changes to collagen fibril spacing can greatly affect HG by affecting the efficiency of QPM.

(2) Investigation of critical FSL parameters affecting HG:

- Evaluated the effect of FSL pulse energy, NA and repetition rate on SHG and THG. Results showed that increasing any of these parameters lead to increased HG intensity and decreased duration.

- Assessed precise temporal HG characteristics which revealed that the evolution of LIB has a significant effect on HG intensity.

- Quantified single pulse HG intensities which revealed that HG pulse energies approach 1 nJ; HG conversion efficiencies approach 0.1% and decrease with increasing pulse energy, and peak HG powers were above 2 kW.

(3) Evaluation of safety concerns

- Single HG pulses don't seem to present any photochemical or photothermal safety concerns for any ocular tissues using typical therapeutic FSL parameters.

- Conventional clinical FSLs can generate exposures exceeding corneal and lenticular standard MPEs in the event of a scan failure in less than 200 ms. Higher repetition rates may exceed safe retinal exposures in less than 1 ms.

- Scanning exposures using typical procedure parameters and durations can generate corneal and lenticular exposures approaching the MPE. Procedures using slightly higher pulse energies, smaller scan areas, or scan for more than 20 s may generate unsafe exposures.

The major results obtained from some of these individual studies have been published as peer-reviewed journal papers, conference proceedings and abstracts, as selected and listed below:

- **W. Calhoun**, and I. Ilev, "Effect of therapeutic femtosecond laser pulse energy, repetition rate and numerical aperture on laser induced second and third harmonic generation in corneal tissue", *Lasers in Medical Science*, vol. 30, pp. 1341-6, May 2015.

- **W. Calhoun**, E. Akpek, R. Weiblinger, and I. Ilev, "Evaluation of broadband spectral transmission characteristics of fresh and gamma-irradiated corneal tissues", *Cornea*, vol. 34, pp. 228-34, Feb 2015.

- **W. Calhoun**, A. Beylin, R. Weiblinger, and I. Ilev, "Quantification of polarization effects through corneal tissue using ultrashort femtosecond lasers", *Review of Scientific Instruments*, vol. 84, pp. 084301-7, Aug 2013.

- J. Baxi, **W. Calhoun**, Y. Jamal Sepah, D. X. Hammer, I. Ilev, T. J. Pfefer, Q. D. Nguyen, and A. Agrawal, "Retina-simulating phantom for optical coherence tomography," *Journal of Biomedical Opt*ics, vol. 19, pp. 021106-1, Feb 2014.

- **W. Calhoun**, and I. Ilev, "Effect of femtosecond laser pulse energy and repetition rate on laser induced second and third harmonic generation in corneal tissue", *OSA Technical Digest – CLEO: 2014*, Paper ATh3P.5, June 2014.

- **W. Calhoun**, D. Kernik, A. Beylin, R. Weiblinger, and Ilev I, "Nonlinear optical frequency conversions of femtosecond laser in corneal tissue", *Proc. SPIE*, vol. 8579, pp. 8579-10, 2013.

- **W. Calhoun**, A. Beylin, R. Weiblinger, and I. Ilev, "Quantification of phase retardation in corneal tissues using a femtosecond laser", *Proc. SPIE*, vol. 8567, pp. 85672B-1, 2013.

DISCLAIMER:

The mention of commercial products, their sources, or their use in connection with material reported herein is not to be construed as either an actual or implied endorsement of such products by the Department of Health and Human Services.

List of References

[1]   T. H. Maiman, "Stimulated Optical Radiation in Ruby," *Nature,* vol. 187, pp. 493-494, 1960.

[2]   K. Kincade and S. Anderson. (2005, 1 1) Laser Marketplace 2005: Consumer applications boost laser sales 10%. *Laser Focus World.*

[3]   R. Fork, L., B. Green, I., and C. Shank, V., "Generation of optical pulses shorter than 0.1 psec by colliding pulse mode locking " *Applied Physics Letters,* vol. 38, 1981.

[4]   W. Knox, H., M. Downer, C., and C. Shank, V., "Amplified femtosecond optical pulses and continuum generation at 5-kHz repetition rate," *Optics Letters,* vol. 9, pp. 552-554, 1984.

[5]   E. G. Faktorovich, "Femtodynamics: optimizing femtosecond laser settings and procedure techniques to optimize outcomes," *Int Ophthalmol Clin,* vol. 48, pp. 41-50, Winter 2008.

[6]   S. Kenth, J. P. Sylvestre, K. Fuhrmann, M. Meunier, and J. C. Leroux, "Fabrication of paclitaxel nanocrystals by femtosecond laser ablation and fragmentation," *Journal of pharmaceutical sciences,* vol. 100, pp. 1022-1030, 2011.

[7]   B. Cense, E. Koperda, J. M. Brown, O. P. Kocaoglu, W. Gao, R. S. Jonnal*, et al.*, "Volumetric retinal imaging with ultrahigh-resolution spectral-domain optical coherence tomography and adaptive optics using two broadband light sources," *Optics Express,* vol. 17, pp. 4095-4111, Mar 2 2009.

[8]   A. A. Lanin, I. y. V. Fedotov, D. A. Sidorov-Biryukov, L. V. Doronina-Amitonova, O. I. Ivashkina, M. A. Zots*, et al.*, "Air-guided photonic-crystal-fiber pulse-compression delivery of multimegawatt femtosecond laser output for nonlinear-optical imaging and neurosurgery," *Applied Physics Letters,* vol. 100, Mar 5 2012.

[9]   M. Dutra-Correa, G. Nicolodelli, J. R. Rodrigues, C. Kurachi, and V. S. Bagnato, "Femtosecond laser ablation on dental hard tissues—Analysis of ablated profile near an interface using local effective intensity," *Laser Physics,* vol. 21, pp. 965-971, 2011.

[10]   R. Meesat, H. Belmouaddine, J. F. Allard, C. Tanguay-Renaud, R. Lemay, T. Brastaviceanu*, et al.*, "Cancer radiotherapy based on femtosecond IR laser-beam filamentation yielding ultra-high dose rates and zero entrance dose," *Proc Natl Acad Sci U S A,* vol. 109, pp. E2508-13, Sep 18 2012.

[11]   S. H. Chung and E. Mazur, "Surgical applications of femtosecond lasers," *J Biophotonics,* vol. 2, pp. 557-72, Oct 2009.

[12]   W. Sibbett, A. Lagatsky, and C. Brown, "The development and application of femtosecond laser systems," *Optics Express,* vol. 20, pp. 6989-7001, 2012.

[13]   K. Ozulken, F. Cabot, and S. H. Yoo, "Applications of femtosecond lasers in ophthalmic surgery," *Expert Rev Med Devices,* vol. 10, pp. 115-24, Jan 2013.

[14]   H. K. Soong and J. B. Malta, "Femtosecond lasers in ophthalmology," *Am J Ophthalmol,* vol. 147, pp. 189-197 e2, Feb 2009.

[15]   C. L. Hoy, O. Ferhanoglu, M. Yildirim, K. H. Kim, S. S. Karajanagi, K. M. C. Chan*, et al.*, "Clinical ultrafast laser surgery: Recent advances and future directions," *Ieee Journal of Selected Topics in Quantum Electronics,* vol. 20, March/April 2014.

[16]   I. Ratkay-Traub, T. Juhasz, C. Horvath, C. Suarez, K. Kiss, I. Ferincz*, et al.*, "Ultra-short pulse (femtosecond) laser surgery: initial use in LASIK flap creation," *Ophthalmology clinics of North America,* vol. 14, pp. 347-55, viii-ix, 2001-Jun 2001.

[17]   H. Lubatschowski, G. Maatz, A. Heisterkamp, U. Hetzel, W. Drommer, H. Welling*, et al.*, "Application of ultrashort laser pulses for intrastromal refractive surgery," *Graefes Arch Clin Exp Ophthalmol,* vol. 238, pp. 33-9, Jan 2000.

[18]   G. D. Kymionis, V. P. Kankariya, A. D. Plaka, and D. Z. Reinstein, "Femtosecond laser technology in corneal refractive surgery: a review," *Journal of refractive surgery (Thorofare, NJ: 1995),* vol. 28, pp. 912-920, 2012.

[19]   A. A. Farjo, A. Sugar, S. C. Schallhorn, P. A. Majmudar, D. J. Tanzer, W. B. Trattler*, et al.*, "Femtosecond lasers for LASIK flap creation: a report by the American Academy of Ophthalmology," *Ophthalmology,* vol. 120, pp. e5-e20, Mar 2013.

[20]   G. M. Kezirian and K. G. Stonecipher, "Comparison of the IntraLase femtosecond laser and mechanical keratomes for laser in situ keratomileusis," *J Cataract Refract Surg,* vol. 30, pp. 804-11, Apr 2004.

[21]   R. Naranjo-Tackman, "How a femtosecond laser increases safety and precision in cataract surgery?," *Curr Opin Ophthalmol,* vol. 22, pp. 53-7, Jan 2011.

[22] K. P. Reddy, J. Kandulla, and G. U. Auffarth, "Effectiveness and safety of femtosecond laser-assisted lens fragmentation and anterior capsulotomy versus the manual technique in cataract surgery," *J Cataract Refract Surg,* vol. 39, pp. 1297-306, Sep 2013.

[23] L. Jay, A. Brocas, K. Singh, J. C. Kieffer, I. Brunette, and T. Ozaki, "Determination of porcine corneal layers with high spatial resolution by simultaneous second and third harmonic generation microscopy," *Optics Express,* vol. 16, p. 16284, 2008.

[24] N. Morishige, A. J. Wahlert, M. C. Kenney, D. J. Brown, K. Kawamoto, T. Chikama*, et al.*, "Second-harmonic imaging microscopy of normal human and keratoconus cornea," *Invest Ophthalmol Vis Sci,* vol. 48, pp. 1087-94, Mar 2007.

[25] "Eye Health Statistics at a Glance," American Academy of Ophthalmology2011.

[26] P. S. Binder, "Femtosecond applications for anterior segment surgery," *Eye Contact Lens,* vol. 36, pp. 282-5, Sep 2010.

[27] "Routine Preoperative Testing Before Cataract Surgery," US Department of Health and Human Services2000.

[28] T. Kohnen, M. Baumeister, D. Kook, O. K. Klaproth, and C. Ohrloff, "Cataract Surgery With Implantation of an Artificial Lens," *Deutsches Arzteblatt International,* vol. 106, pp. 695-U11, Oct 2009.

[29] "Global Intraocular Lens (IOL) Market 2013-18: Industry Nanotechnology Analysis, Size, Share, Strategies, Growth, Trends and Forecast Research Report " 2013.

[30] "Eye Banking Statistical Report," Eye Bank Association of America2013.

[31] T. P. Radhakrishnan, "Molecular structure, symmetry, and shape as design elements in the fabrication of molecular crystals for second harmonic generation and the role of molecules-in-materials," *Accounts of Chemical Research,* vol. 41, pp. 367-376, Mar 2008.

[32] J. F. McGilp, "Second-harmonic generation at semiconductor and metal surfaces," *Surface Review and Letters,* vol. 6, pp. 529-558, Jun-Aug 1999.

[33] P. J. Campagnola, H. A. Clark, W. A. Mohler, A. Lewis, and L. M. Loew, "Second-harmonic imaging microscopy of living cells," *Journal of Biomedical Optics,* vol. 6, pp. 277-286, Jul 2001.

[34] W. Radner, M. Zehetmayer, R. Aufreiter, and R. Mallinger, "Interlacing and cross-angle distribution of collagen lamellae in the human cornea," *Cornea,* vol. 17, pp. 537-543, Sep 1998.

[35]   R. Hamada, B. Graf, J. P. Giraud, and Poulique.Y, "Analytical and Statistical Study of Lamellae, Keratocytes and Collagen Fibrillae of Central Region of Normal Human Cornea - (Light and Electron-Microscope Study)," *Archives D Ophtalmologie,* vol. 32, pp. 563-&, 1972 1972.

[36]   M. J. Doughty, S. Petrou, and H. Macmillan, "Anatomy and morphology of the cornea of bovine eyes from a slaughterhouse," *Canadian Journal of Zoology-Revue Canadienne De Zoologie,* vol. 73, pp. 2159-2165, Nov 1995.

[37]   S. Hayashi, T. Osawa, and K. Tohyama, "Comparative observations on corneas, with special reference to Bowman's layer and Descemet's membrane in mammals and amphibians," *Journal of Morphology,* vol. 254, pp. 247-258, Dec 2002.

[38]   R. I. Angunawela, A. Riau, S. S. Chaurasia, D. T. Tan, and J. S. Mehta, "Manual suction versus femtosecond laser trephination for penetrating keratoplasty: intraocular pressure, endothelial cell damage, incision geometry, and wound healing responses," *Invest Ophthalmol Vis Sci,* vol. 53, pp. 2571-9, May 2012.

[39]   L. Buratto and E. Bohm, "The use of the femtosecond laser in penetrating keratoplasty," *American Journal of Ophthalmology,* vol. 143, pp. 737-742, May 2007.

[40]   H. K. Soong, S. Mian, O. Abbasi, and T. Juhasz, "Femtosecond laser-assisted posterior lamellar keratoplasty: initial studies of surgical technique in eye bank eyes," *Ophthalmology,* vol. 112, pp. 44-9, Jan 2005.

[41]   J. H. Kim, S. K. Choi, and D. Lee, "The comparison of femtosecond laser-assisted penetrating keratoplasty with conventional surgery in terms of endothelial safety: ex vivo study using porcine eyes," *Cornea,* vol. 28, pp. 812-6, Aug 2009.

[42]   L. He, K. Sheehy, and W. Culbertson, "Femtosecond laser-assisted cataract surgery," *Curr Opin Ophthalmol,* vol. 22, pp. 43-52, Jan 2011.

[43]   Z. Z. Nagy, K. Kranitz, A. I. Takacs, K. Mihaltz, I. Kovacs, and M. C. Knorz, "Comparison of Intraocular Lens Decentration Parameters After Femtosecond and Manual Capsulotomies," *Journal of Refractive Surgery,* vol. 27, pp. 564-569, Aug 2011.

[44]   D. V. Palanker, M. S. Blumenkranz, D. Andersen, M. Wiltberger, G. Marcellino, P. Gooding*, et al.*, "Femtosecond laser-assisted cataract surgery with integrated optical coherence tomography," *Sci Transl Med,* vol. 2, p. 58ra85, Nov 17 2010.

[45]   K. Hayashi, H. Hayashi, F. Nakao, and F. Hayashi, "Risk factors for corneal endothelial injury during phacoemulsification," *Journal of Cataract and Refractive Surgery,* vol. 22, pp. 1079-1084, Oct 1996.

[46]   J. Richard, L. Hoffart, F. Chavane, B. Ridings, and J. Conrath, "Corneal endothelial cell loss after cataract extraction by using ultrasound phacoemulsification versus a fluid-based system," *Cornea,* vol. 27, pp. 17-21, Jan 2008.

[47]   A. I. Takacs, I. Kovacs, K. Mihaltz, T. Filkorn, M. C. Knorz, and Z. Z. Nagy, "Central corneal volume and endothelial cell count following femtosecond laser-assisted refractive cataract surgery compared to conventional phacoemulsification," *J Refract Surg,* vol. 28, pp. 387-91, Jun 2012.

[48]   I. Conrad-Hengerer, M. Al Juburi, T. Schultz, F. H. Hengerer, and H. B. Dick, "Corneal endothelial cell loss and corneal thickness in conventional compared with femtosecond laser-assisted cataract surgery: three-month follow-up," *J Cataract Refract Surg,* vol. 39, pp. 1307-13, Sep 2013.

[49]   R. Yeilding, J. Villar-Kuri, R. Naranjo-Tackman, E. Stangogiannis, Y. Martinez, S. Garcia*, et al.*, "Evaluation of Size and Shape of Anterior Lens Capsules after Photodisruption Laser Capsulotomy and Continuous Curvilinear Capsulorrhexis," *Invest. Ophthalmol. Vis. Sci.,* vol. 50, pp. 1145-, April 11, 2009 2009.

[50]   L. Roach. (2013, July 2013) Femtosecond for Cataract: Are Lasers Good for Business? *Eye Net*. 44-50.

[51]   D. Sofikitis, L. Bougas, G. E. Katsoprinakis, A. K. Spiliotis, B. Loppinet, and T. P. Rakitzis, "Evanescent-wave and ambient chiral sensing by signal-reversing cavity ringdown polarimetry," *Nature,* vol. 514, pp. 76-79, 10/02/print 2014.

[52]   J. C. Kieffer and M. Chaker, "X-ray sources based on subpicosecond-laser-produced plasmas," *J Xray Sci Technol,* vol. 4, pp. 312-22, Jan 1 1994.

[53]   A. Vogel, J. Noack, G. Hüttman, and G. Paltauf, "Mechanisms of femtosecond laser nanosurgery of cells and tissues," *Applied Physics B,* vol. 81, pp. 1015-1047, 2005.

[54]   K. Sugioka and Y. Cheng, "Femtosecond laser processing for optofluidic fabrication," *Lab Chip,* vol. 12, pp. 3576-89, Oct 7 2012.

[55]   H. Lubatschowski, "Overview of commercially available femtosecond lasers in refractive surgery," *Journal of Refractive Surgery,* vol. 24, pp. 102-107, Jan 2008.

[56]   J. S. Pepose and H. Lubatschowski, "Comparing Femtosecond Lasers," in *Cataract and Refractive Surgery Today*, ed, 2008.

[57]   S. Serrao, L. Buratto, G. Lombardo, M. P. De Santo, P. Ducoli, and M. Lombardo, "Optimal parameters to improve the interface quality of the flap bed in femtosecond laser-assisted laser in situ keratomileusis," *J Cataract Refract Surg,* vol. 38, pp. 1453-9, Aug 2012.

[58]   E. Hecht, *Optics*. San Francisco: Pearson, 2002.

[59]   P. Rosales, M. Dubbelman, S. Marcos, and R. van der Heijde, "Crystalline lens radii of curvature from Purkinje and Scheimpflug imaging," *Journal of Vision,* vol. 6, pp. 1057-1067, 2006.

[60]   E. M. Beems and J. A. Van Best, "Light transmission of the cornea in whole human eyes," *Exp Eye Res,* vol. 50, pp. 393-5, Apr 1990.

[61]   E. A. Boettner and J. R. Wolter, "Transmission of the ocular media," *Investigative Ophthalmology,* vol. 1, pp. 776-783, 1962 1962.

[62]   J. Doutch, A. J. Quantock, V. A. Smith, and K. M. Meek, "Light transmission in the human cornea as a function of position across the ocular surface: theoretical and experimental aspects," *Biophys J,* vol. 95, pp. 5092-9, Dec 2008.

[63]   R. W. Hart and R. A. Farrell, "Light scattering in the cornea," *J Opt Soc Am,* vol. 59, pp. 766-74, Jun 1969.

[64]   J. V. Jester, T. Moller-Pedersen, J. Y. Huang, C. M. Sax, W. T. Kays, H. D. Cavangh*, et al.*, "The cellular basis of corneal transparency: evidence for 'corneal crystallins'," *Journal of Cell Science,* vol. 112, pp. 613-622, Mar 1999.

[65]   C. d. l'Eclairage, "Standard CIE S 017/E:2011," in *International Lighting Vocabulary*, ed, 2011.

[66]   L. Kolozsvari, A. Nogradi, B. Hopp, and Z. Bor, "UV absorbance of the human cornea in the 240-to 400-nm range," *Investigative Ophthalmology & Visual Science,* vol. 43, pp. 2165-2168, Jul 2002.

[67]   J. E. Roberts, "Ocular phototoxicity," *Journal of Photochemistry and Photobiology B-Biology,* vol. 64, pp. 136-143, Nov 2001.

[68]   B. G. Yust, L. C. Mimun, and D. K. Sardar, "Optical absorption and scattering of bovine cornea, lens, and retina in the near-infrared region," *Lasers Med Sci,* vol. 27, pp. 413-22, Mar 2012.

[69]   J. A. van Best, J. G. Bollemeijer, and C. C. Sterk, "Corneal transmission in whole human eyes," *Exp Eye Res,* vol. 46, pp. 765-8, May 1988.

[70]   P. V. Algvere, P. A. Torstensson, and B. M. Tengroth, "Light transmittance of ocular media in living rabbit eyes," *Invest Ophthalmol Vis Sci,* vol. 34, pp. 349-54, Feb 1993.

[71]   J. P. Whitcher, M. Srinivasan, and M. P. Upadhyay, "Corneal blindness: a global perspective," *Bull World Health Organ,* vol. 79, pp. 214-21, 2001.

[72]   N. Ehlers, "World eye banking," *Acta Ophthalmologica Scandinavica,* vol. 75, pp. 481-481, Oct 1997.

[73]   "Eye Banking Statistical Report," Eye Bank Association of America2009.

[74]   W. R. Calhoun, E. K. Akpek, R. Weiblinger, and I. K. Ilev, "Evaluation of broadband spectral transmission characteristics of fresh and gamma-irradiated corneal tissues," *Cornea,* vol. 34, pp. 228-34, Feb 2015.

[75]   J. S. Werner, "Childrens Sunglasses - Caveat-Emptor," *Optometry and Vision Science,* vol. 68, pp. 318-320, Apr 1991.

[76]   Z. Zhang, T. R. Gentile, A. L. Migdall, and R. Datla, "Transmittance measurements for filters of optical density between one and ten," *Applied optics,* vol. 36, pp. 8889-8895, 1997.

[77]   E. Walker and A. S. Nowacki, "Understanding equivalence and noninferiority testing," *J Gen Intern Med,* vol. 26, pp. 192-6, Feb 2011.

[78]   S. Prahl. Tabulated Molar Extinction Coefficient for ICG in Albumin [Online]. Available: http://omlc.ogi.edu/spectra/icg/omlc-albumin.html

[79]   O. M. Oriowo, A. P. Cullen, B. R. Chou, and J. G. Sivak, "Action spectrum and recovery for in vitro UV-induced cataract using whole lenses," *Invest Ophthalmol Vis Sci,* vol. 42, pp. 2596-602, Oct 2001.

[80]   L. T. Sharpe, A. Stockman, W. Jagla, and H. Jagle, "A luminous efficiency function, V*(lambda), for daylight adaptation," *J Vis,* vol. 5, pp. 948-68, 2005.

[81]   T. J. Freegard, "The physical basis of transparency of the normal cornea," *Eye,* vol. 11, pp. 465-471, 1997.

[82]   G. New, *An introduction to nonlinear optics*. Cambridge: Cambridge University Press, 2011.

[83]   R. LaComb, O. Nadiarnykh, S. S. Townsend, and P. J. Campagnola, "Phase matching considerations in second harmonic generation from tissues: Effects on emission directionality, conversion efficiency and observed morphology," *Optics Communications,* vol. 281, pp. 1823-1832, Apr 2008.

[84]   P. Stoller, B. M. Kim, A. M. Rubenchik, K. M. Reiser, and L. B. Da Silva, "Polarization-dependent optical second-harmonic imaging of a rat-tail tendon," *Journal of Biomedical Optics,* vol. 7, pp. 205-214, Apr 2002.

[85] C. Hnatovsky, V. G. Shvedov, N. Shostka, A. V. Rode, and W. Krolikowski, "Polarization-dependent ablation of silicon using tightly focused femtosecond laser vortex pulses," *Opt Lett,* vol. 37, pp. 226-8, Jan 15 2012.

[86] S. Ho, M. Haque, P. R. Herman, and J. S. Aitchison, "Femtosecond laser-assisted etching of three-dimensional inverted-woodpile structures in fused silica," *Optics Letters,* vol. 37, pp. 1682-1684, May 15 2012.

[87] L. J. Bour, "Polarized light and the eye," *Visual Optics and Instrumentation,* pp. 310-325, 1991.

[88] M. Bom and E. Wolf, "Principles of optics," in *Pergamon Oxford (Ed.)*, ed, 1980.

[89] M. Wolman and F. H. Kasten, "Polarized light microscopy in the study of the molecular structure of collagen and reticulin," *Histochemistry,* vol. 85, pp. 41-9, 1986 1986.

[90] D. M. Maurice, "The structure and transparency of the cornea," *J Physiol,* vol. 136, pp. 263-86, Apr 30 1957.

[91] D. M. Maurice, "The cornea and the sclera," in *The Eye*, H. Davson, Ed., ed London: Academic Press, 1984, pp. 1-158.

[92] G. P. Misson, "The theory and implications of the biaxial model of corneal birefringence," *Ophthalmic Physiol Opt,* vol. 30, pp. 834-46, Nov 2010.

[93] G. J. Van Blokland and S. C. Verhelst, "Corneal polarization in the living human eye explained with a biaxial model," *J Opt Soc Am A,* vol. 4, pp. 82-90, Jan 1987.

[94] R. W. Knighton, X.-R. Huang, and L. A. Cavuoto, "Corneal birefringence mapped by scanning laser polarimetry," *Optics Express,* vol. 16, p. 13738, 2008.

[95] W. Calhoun, R. Weiblinger, A. Beylin, and I. K. Ilev, "Assessing the phase retardation in corneal tissues using a femtosecond laser," *Rev Sci Instrum,* vol. 84, p. 084301, Aug 2013.

[96] W. N. Charman, "Reflection of plane-polarized light by the retina," *Br J Physiol Opt,* vol. 34, pp. 34-49, 1980.

[97] J. M. Bueno and J. Jaronski, "Spatially resolved polarization properties for in vitro corneas," *Ophthalmic and Physiological Optics,* vol. 21, pp. 384-392, 2001.

[98] M. Pircher, C. K. Hitzenberger, and U. Schmidt-Erfurth, "Polarization sensitive optical coherence tomography in the human eye," *Prog Retin Eye Res,* vol. 30, pp. 431-51, Nov 2011.

[99]   M. Miclea, U. Skrzypczak, S. Faust, F. Fankhauser, H. Graener, and G. Seifert, "Nonlinear refractive index of porcine cornea studied by z-scan and self-focusing during femtosecond laser processing," *Opt Express,* vol. 18, pp. 3700-7, Feb 15 2010.

[100]   W. Calhoun, D. Kernik, A. Beylin, R. Weiblinger, and I. Ilev, "Nonlinear optical frequency conversions of a femtosecond laser in cornea tissue," in *SPIE Photonics West*, San Francisco, 2013.

[101]   R. Boyd, *Nonlinear Optics*, 3 ed. Burlington, MA: Academic Press, 2008.

[102]   F. Docchio, C. Sacchi, and J. Marshall, "Experimental investigation of optical breakdown thresholds in ocular media under single pulse irradiation with different pulse durations," *Lasers Ophthalmol,* vol. 1, pp. 83-93, 1986.

[103]   A. Vogel and V. Venugopalan, "Mechanisms of pulsed laser ablation of biological tissues," *Chem Rev,* vol. 103, pp. 577-644, Feb 2003.

[104]   D. Milam, "LASER-INDUCED DAMAGE AT 1064 NM, 125 PSEC," *Applied Optics,* vol. 16, pp. 1204-1213, 1977 1977.

[105]   J. Noack and A. Vogel, "Laser-induced plasma formation in water at nanosecond to femtosecond time scales: Calculation of thresholds, absorption coefficients, and energy density," *IEEE Journal of Quantum Electronics,* vol. 35, pp. 1156-1167, Aug 1999.

[106]   Y. P. Raizer, "Heating of a Gas by a Powerful Light Pulse," *Soviet Physics Jetp-Ussr,* vol. 21, pp. 1009-&, 1965 1965.

[107]   F. Docchio, P. Regondi, M. R. Capon, and J. Mellerio, "Study of the temporal and spatial dynamics of plasmas induced in liquids by nanosecond Nd:YAG laser pulses. 1: Analysis of the plasma starting times," *Appl Opt,* vol. 27, pp. 3661-8, Sep 1 1988.

[108]   F. Docchio, P. Regondi, M. R. Capon, and J. Mellerio, "Study of the temporal and spatial dynamics of plasmas induced in liquids by nanosecond Nd:YAG laser pulses. 2: Plasma luminescence and shielding," *Appl Opt,* vol. 27, pp. 3669-74, Sep 1 1988.

[109]   A. O. H. Vogel, *Optical breakdown in water and ocular media, and its use for intraocular photodisruption*: Shaker, 2001.

[110]   D. N. Nikogosyan, A. A. Oraevsky, and V. I. Rupasov, "Two-photon ionization and dissociation of liquid water by powerful laser UV radiation," *Chemical Physics,* vol. 77, pp. 131-143, 1983.

[111]   P. A. Franken, G. Weinreich, C. W. Peters, and A. E. Hill, "Generation of Optical Harmonics," *Physical Review Letters,* vol. 7, pp. 118-&, 1961 1961.

[112] J. Baxi, W. Calhoun, Y. J. Sepah, D. X. Hammer, I. Ilev, T. J. Pfefer*, et al.*, "Retina-simulating phantom for optical coherence tomography," *J Biomed Opt,* vol. 19, p. 21106, Feb 1 2014.

[113] D. J. Lund, B. E. Stuck, and P. Edsall, "Retinal injury thresholds for blue wavelength lasers," *Health Physics,* vol. 90, pp. 477-484, May 2006.

[114] C. P. Cain, C. A. Toth, G. D. Noojin, D. J. Stolarski, R. J. Thomas, and B. A. Rockwell, "Thresholds for retinal injury from multiple near-infrared ultrashort laser pulses," *Health Physics,* vol. 82, pp. 855-862, Jun 2002.

[115] J. Wang, C. Sramek, Y. M. Paulus, D. Lavinsky, G. Schuele, D. Anderson*, et al.*, "Retinal safety of near-infrared lasers in cataract surgery," *J Biomed Opt,* vol. 17, pp. 95001-1, Sep 2012.

[116] A. Heisterkamp, T. Ripken, T. Mamom, W. Drommer, H. Welling, W. Ertmer*, et al.*, "Nonlinear side effects of fs pulses inside corneal tissue during photodisruption," *Applied Physics B-Lasers and Optics,* vol. 74, pp. 419-425, Apr 2002.

[117] R. L. Harzic, R. Bückle, C. Wüllner, C. Donitzky, and K. König, "Laser safety aspects for refractive eye surgery with femtosecond laser pulses," *Medical Laser Application,* vol. 20, pp. 233-238, 2005.

[118] B. A. Rockwell, R. J. Thomas, and A. Vogel, "Ultrashort laser pulse retinal damage mechanisms and their impact on thresholds," *Medical Laser Application,* vol. 25, pp. 84-92, 2010.

[119] B. A. Rockwell, D. X. Hammer, R. A. Hopkins, D. J. Payne, C. A. Toth, W. P. Roach*, et al.*, "Ultrashort laser pulse bioeffects and safety," *Journal of Laser Applications,* vol. 11, pp. 42-44, Feb 1999.

[120] N. Olivier, F. Aptel, K. Plamann, M.-C. Schanne-Klein, and E. Beaurepaire, "Harmonic microscopy of isotropic and anisotropic microstructure of the human cornea," *Optics Express,* vol. 18, pp. 5028-5040, Mar 1 2010.

[121] F. Aptel, N. Olivier, A. Deniset-Besseau, J.-M. Legeais, K. Plamann, M.-C. Schanne-Klein*, et al.*, "Multimodal Nonlinear Imaging of the Human Cornea," *Investigative Ophthalmology & Visual Science,* vol. 51, pp. 2459-2465, May 2010.

[122] W. L. Chen, C. K. Chou, M. G. Lin, Y. F. Chen, S. H. Jee, H. Y. Tan*, et al.*, "Single-wavelength reflected confocal and multiphoton microscopy for tissue imaging," *J Biomed Opt,* vol. 14, p. 054026, Sep-Oct 2009.

[123] P. Stoller, K. M. Reiser, P. M. Celliers, and A. M. Rubenchik, "Polarization-modulated second harmonic generation in collagen," *Biophys J,* vol. 82, pp. 3330-42, Jun 2002.

[124] B. Vohnsen and P. Artal, "Second-harmonic microscopy of ex vivo porcine corneas," *Journal of Microscopy,* vol. 232, pp. 158-163, Oct 2008.

[125] M. Han, L. Zickler, G. Giese, M. Walter, F. H. Loesel, and J. F. Bille, "Second-harmonic imaging of cornea after intrastromal femtosecond laser ablation," *J Biomed Opt,* vol. 9, pp. 760-6, Jul-Aug 2004.

[126] S.-Y. Chen, H.-C. Yu, I. J. Wang, and C.-K. Sun, "Infrared-based third and second harmonic generation imaging of cornea," *Journal of Biomedical Optics,* vol. 14, Jul-Aug 2009.

[127] G. N. Ramachandran and G. Kartha, "STRUCTURE OF COLLAGEN," *Nature,* vol. 174, pp. 269-270, 1954 1954.

[128] O. del Barco and J. M. Bueno, "Second harmonic generation signal in collagen fibers: role of polarization, numerical aperture, and wavelength," *Journal of Biomedical Optics,* vol. 17, Apr 2012.

[129] Y. Chang, C. Chen, J. Chen, Y. Jin, and X. Deng, "Theoretical simulation study of linearly polarized light on microscopic second-harmonic generation in collagen type I," *J Biomed Opt,* vol. 14, p. 044016, Jul-Aug 2009.

[130] G. Latour, I. Gusachenko, L. Kowalczuk, I. Lamarre, and M.-C. Schanne-Klein, "In vivo structural imaging of the cornea by polarization-resolved second harmonic microscopy," *Biomedical Optics Express,* vol. 3, pp. 1-15, Jan 1 2012.

[131] R. M. Williams, W. R. Zipfel, and W. W. Webb, "Interpreting second-harmonic generation images of collagen I fibrils," *Biophysical Journal,* vol. 88, pp. 1377-1386, Feb 2005.

[132] C. Odin, Y. Le Grand, A. Renault, L. Gailhouste, and G. Baffet, "Orientation fields of nonlinear biological fibrils by second harmonic generation microscopy," *Journal of Microscopy-Oxford,* vol. 229, pp. 32-38, Jan 2008.

[133] J. M. Bueno, E. J. Gualda, and P. Artal, "Analysis of corneal stroma organization with wavefront optimized nonlinear microscopy," *Cornea,* vol. 30, pp. 692-701, Jun 2011.

[134] H. Aghamohammadzadeh, R. H. Newton, and K. M. Meek, "X-ray scattering used to map the preferred collagen orientation in the human cornea and limbus," *Structure,* vol. 12, pp. 249-256, Feb 2004.

[135] N. Morishige, W. M. Petroll, T. Nishida, M. C. Kenney, and J. V. Jester, "Noninvasive corneal stromal collagen imaging using two-photon-generated second-harmonic signals," *Journal of Cataract and Refractive Surgery,* vol. 32, pp. 1784-1791, Nov 2006.

[136] G. Wollensak, E. Spoerl, and T. Seiler, "Riboflavin/ultraviolet-A-induced collagen crosslinking for the treatment of keratoconus," *American Journal of Ophthalmology,* vol. 135, pp. 620-627, May 2003.

[137] W. Radner, M. Zehetmayer, C. Skorpik, and R. Mallinger, "Zur Anordnung der kollagenen Lamellen beim Keratokonus," *Spektrum der Augenheilkunde,* vol. 10, pp. 156-160, 1996/08/01 1996.

[138] A. Daxer and P. Fratzl, "Collagen fibril orientation in the human corneal stroma and its implication in keratoconus," *Investigative Ophthalmology & Visual Science,* vol. 38, pp. 121-129, Jan 1997.

[139] C. Edmund, "Corneal elasticity and ocular rigidity in normal and keratoconic eyes," *Acta Ophthalmol (Copenh),* vol. 66, pp. 134-40, Apr 1988.

[140] I. S. Nash, P. R. Greene, and C. S. Foster, "Comparison of mechanical properties of keratoconus and normal corneas," *Exp Eye Res,* vol. 35, pp. 413-24, Nov 1982.

[141] S. Tanaka, G. Avigad, B. Brodsky, and E. F. Eikenberry, "Glycation induces expansion of the molecular packing of collagen," *J Mol Biol,* vol. 203, pp. 495-505, Sep 20 1988.

[142] G. Wollensak, M. Wilsch, E. Spoerl, and T. Seiler, "Collagen fiber diameter in the rabbit cornea after collagen crosslinking by riboflavin/UVA," *Cornea,* vol. 23, pp. 503-507, Jul 2004.

[143] D. Kampik, B. Ralla, S. Keller, M. Hirschberg, P. Friedl, and G. Geerling, "Influence of Corneal Collagen Crosslinking with Riboflavin and Ultraviolet-A Irradiation on Excimer Laser Surgery," *Investigative Ophthalmology & Visual Science,* vol. 51, pp. 3929-3934, Aug 2010.

[144] S. Sikder, R. L. McCally, C. Engler, D. Ward, and A. S. Jun, "Evaluation of Irradiated Corneas Using Scatterometry and Light and Electron Microscopy," *Cornea,* vol. 30, pp. 503-507, May 2011.

[145] J. C. J. C. W. S. J. Elisseeff, "Extracellular Matrix Characterization of the Acellular Gamma-Irradiated Cornea," presented at the ARVO, 2013.

[146] S. Hayes, C. Boote, C. S. Kamma-Lorger, M. S. Rajan, J. Harris, E. Dooley*, et al.*, "Riboflavin/UVA Collagen Cross-Linking-Induced Changes in Normal and Keratoconus Corneal Stroma," *Plos One,* vol. 6, Aug 5 2011.

[147] V. Nuzzo, M. Savoldelli, J. M. Legeais, and K. Plamann, "Self-focusing and spherical aberrations in corneal tissue during photodisruption by femtosecond laser," *J Biomed Opt,* vol. 15, p. 038003, May-Jun 2010.

[148] V. Nuzzo, K. Plamann, M. Savoldelli, M. Merano, D. Donate, O. Albert, *et al.*, "In situ monitoring of second-harmonic generation in human corneas to compensate for femtosecond laser pulse attenuation in keratoplasty," *J Biomed Opt,* vol. 12, p. 064032, Nov-Dec 2007.

[149] W. R. Calhoun, 3rd and I. K. Ilev, "Effect of therapeutic femtosecond laser pulse energy, repetition rate, and numerical aperture on laser-induced second and third harmonic generation in corneal tissue," *Lasers Med Sci,* Mar 17 2015.

[150] A. Vogel, J. Noack, K. Nahen, D. Theisen, S. Busch, U. Parlitz, *et al.*, "Energy balance of optical breakdown in water at nanosecond to femtosecond time scales," *Applied Physics B-Lasers and Optics,* vol. 68, pp. 271-280, Feb 1999.

[151] A. Vogel, P. Schweiger, A. Frieser, M. N. Asiyo, and R. Birngruber, "Intraocular Nd-Yag Laser-Surgery - Light Tissue Interaction, Damage Range, and Reduction of Collateral Effects," *Ieee Journal of Quantum Electronics,* vol. 26, pp. 2240-2260, Dec 1990.

[152] M. H. Niemz, E. G. Klancnik, and J. F. Bille, "Plasma-Mediated Ablation of Corneal Tissue at 1053-Nm Using a Nd-Ylf Oscillator Regenerative Amplifier Laser," *Lasers in Surgery and Medicine,* vol. 11, pp. 426-431, 1991 1991.

[153] L. Moreaux, T. Pons, V. Dambrin, M. Blanchard-Desce, and J. Mertz, "Electro-optic response of second-harmonic generation membrane potential sensors," *Optics Letters,* vol. 28, pp. 625-627, Apr 15 2003.

[154] J. Mertz and L. Moreaux, "Second-harmonic generation by focused excitation of inhomogeneously distributed scatterers," *Optics Communications,* vol. 196, pp. 325-330, Sep 1 2001.

[155] L. Moreaux, O. Sandre, and J. Mertz, "Membrane imaging by second-harmonic generation microscopy," *Journal of the Optical Society of America B-Optical Physics,* vol. 17, pp. 1685-1694, Oct 2000.

[156] G. K. Samanta, S. C. Kumar, K. Devi, and M. Ebrahim-Zadeh, "Multicrystal, continuous-wave, single-pass second-harmonic generation with 56% efficiency," *Optics Letters,* vol. 35, pp. 3513-3515, Oct 15 2010.

[157] M. Ghotbi, M. Ebrahim-Zadeh, A. Majchrowski, E. Michalski, and I. V. Kityk, "High-average-power femtosecond pulse generation in the blue using BiB3O6," *Optics Letters,* vol. 29, pp. 2530-2532, Nov 2004.

[158] M. H. Niemz, "Threshold Dependence of Laser-Induced Optical-Breakdown on Pulse Duration," *Applied Physics Letters,* vol. 66, pp. 1181-1183, Mar 6 1995.

[159] B. C. Stuart, M. D. Feit, S. Herman, A. M. Rubenchik, B. W. Shore, and M. D. Perry, "Nanosecond-to-femtosecond laser-induced breakdown in dielectrics," *Physical Review B,* vol. 53, pp. 1749-1761, Jan 15 1996.

[160] P. K. Kennedy, "A First-Order Model for Computation of Laser-Induced Breakdown Thresholds in Ocular and Aqueous-Media .1. Theory," *Ieee Journal of Quantum Electronics,* vol. 31, pp. 2241-2249, Dec 1995.

[161] P. K. Kennedy, S. A. Boppart, D. X. Hammer, B. A. Rockwell, G. D. Noojin, and W. P. Roach, "A First-Order Model for Computation of Laser-Induced Breakdown Thresholds in Ocular and Aqueous-Media .2. Comparison to Experiment," *Ieee Journal of Quantum Electronics,* vol. 31, pp. 2250-2257, Dec 1995.

[162] L. Werner, O. Yeh, J. Haymore, B. Haugen, N. Romaniv, and N. Mamalis, "Corneal endothelial safety with the irradiation system for light-adjustable intraocular lenses," *Journal of Cataract and Refractive Surgery,* vol. 33, pp. 873-878, May 2007.

[163] G. Wollensak, E. Sporl, F. Reber, L. Pillunat, and R. Funk, "Corneal endothelial cytotoxicity of riboflavin/UVA treatment in vitro," *Ophthalmic Research,* vol. 35, pp. 324-328, 2003 2003.

[164] A. Lichtinger, C. A. Sandstedt, K. Padilla, D. M. Schwartz, and A. S. Chayet, "Corneal endothelial safety after ultraviolet light treatment of the light-adjustable intraocular lens," *Journal of Cataract and Refractive Surgery,* vol. 37, pp. 324-327, Feb 2011.

[165] J. A. Zuclich and J. S. Connolly, "Ocular damage induced by near-ultraviolet laser radiation," *Invest Ophthalmol Vis Sci,* vol. 15, pp. 760-4, Sep 1976.

[166] D. G. Pitts, A. P. Cullen, U. o. H. C. o. Optometry, N. I. f. O. Safety, H. D. o. Biomedical, and B. Science, *Ocular effects of ultraviolet radiation from 295 to 365 nm.*: U.S. Department of Health, Education, and Welfare, Public Health Service, Center for Disease Center, National Institute for Occupational Safety and Health, Division of Biomedical and Behavioral Science, 1977.

[167] M. Tomita, G. O. t. Waring, and M. Watabe, "Analysis of corneal endothelial cell density and morphology after laser in situ keratomileusis using two types of femtosecond lasers," *Clinical ophthalmology (Auckland, N.Z.),* vol. 6, pp. 1567-72, 2012 (Epub 2012 Sep 2012.

[168] M. Kimakura, O. Sakai, S. Nakagawa, J. Yoshida, R. Shirakawa, T. Toyono*, et al.*, "Stromal bed quality and endothelial damage after femtosecond laser cuts into the deep corneal stroma," *British Journal of Ophthalmology,* vol. 97, pp. 1404-1409, Nov 2013.

[169] M. S. Oliva and H. Taylor, "Ultraviolet radiation and the eye," *International ophthalmology clinics,* vol. 45, pp. 1-17, 2005 2005.

[170] L. Kessel, L. Eskildsen, M. van der Poel, and M. Larsen, "Non-invasive bleaching of the human lens by femtosecond laser photolysis," *PLoS One,* vol. 5, p. e9711, 2010.

[171] H. Bloemendal, W. de Jong, R. Jaenicke, N. H. Lubsen, C. Slingsby, and A. Tardieu, "Ageing and vision: structure, stability and function of lens crystallins," *Progress in Biophysics & Molecular Biology,* vol. 86, pp. 407-485, Nov 2004.

[172] S. Zigman, "Lens UVA photobiology," *Journal of Ocular Pharmacology and Therapeutics,* vol. 16, pp. 161-165, Apr 2000.

[173] H. R. Taylor, "The environment and the lens," *Br J Ophthalmol,* vol. 64, pp. 303-10, May 1980.

[174] R. D. Glickman, "Ultraviolet phototoxicity to the retina," *Eye Contact Lens,* vol. 37, pp. 196-205, Jul 2011.

[175] U. P. Andley, R. M. Lewis, J. R. Reddan, and I. E. Kochevar, "Action Spectrum for Cytotoxicity in the Uva-Wavelength and Uvb-Wavelength Region in Cultured Lens Epithelial-Cells," *Investigative Ophthalmology & Visual Science,* vol. 35, pp. 367-373, Feb 1994.

[176] U. P. Andley and J. G. Weber, "Ultraviolet action spectra for photobiological effects in cultured human lens epithelial cells," *Photochem Photobiol,* vol. 62, pp. 840-6, Nov 1995.

[177] D. H. Sliney, "How light reaches the eye and its components," *International Journal of Toxicology,* vol. 21, pp. 501-509, Nov-Dec 2002.

[178] J. L. Landry, T. J. Pfefer, and I. K. Ilev, "Laser and Optical Radiation Safety in Biophotonics," in *Biomedical Photonics Handbook*, T. Vo-Dinh, Ed., 2 ed: Taylor and Francis, 2014.